

AD-A193 562

BODY AND SURFACE WAVE MODELING OF OBSERVED SEISMIC
EVENTS PART 3(U) CALIFORNIA INST OF TECH PASADENA
SEISMOLOGICAL LAB R W CLAYTON ET AL. 13 MAY 87

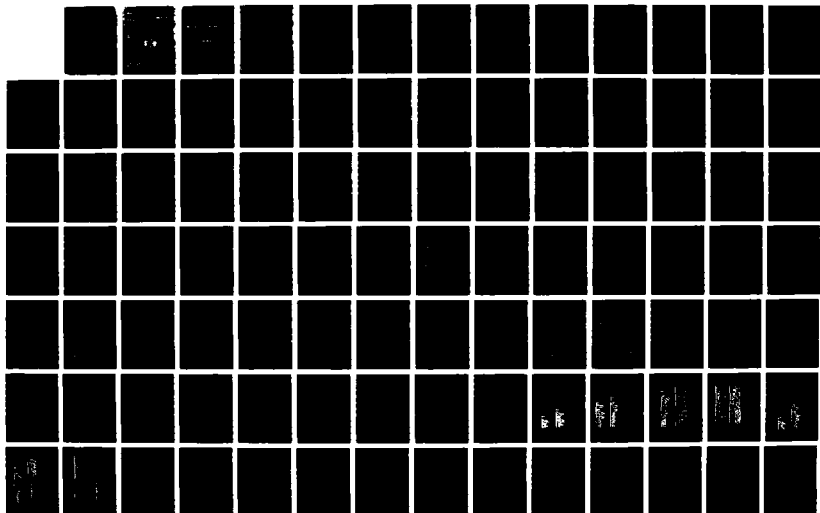
1/2

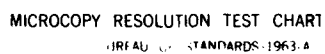
UNCLASSIFIED

AFGL-TR-87-0158 F19628-85-K-0017

F/G 17/10

NL





AD-A193 562

4

DTIC FILE COPY

Body and Surface Wave Modeling of
Observed Seismic Events (Part III)

Robert W. Clayton
David G. Harkrider
Donald V. Helmberger

California Institute of Technology
Seismological Laboratory
Pasadena, CA 91125

13 May 1987

DTIC
ELECTE
APR 29 1988
S D

Final Report
14 July 1986-13 January 1987

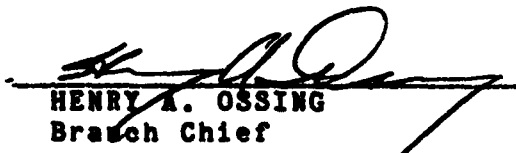
APPROVED FOR PUBLIC RELEASE; DISTRIBUTION UNLIMITED

AIR FORCE GEOPHYSICS LABORATORY
AIR FORCE SYSTEMS COMMAND
UNITED STATES AIR FORCE
HANSCOM AIR FORCE BASE, MASSACHUSETTS 01731

88 4 29 305

"This technical report has been reviewed and is approved for publication"


JAMES F. LEWKOWICZ
Contract Manager


HENRY A. OSSING
Branch Chief

FOR THE COMMANDER


DONALD H. ECKHARDT
Division Director

This report has been reviewed by the ESD Public Affairs Office (PA) and is releasable to the National Technical Information Service (NTIS).

Qualified requestors may obtain additional copies from the Defense Technical Information Center. All others should apply to the National Technical Information Service.

If your address has changed, or if you wish to be removed from the mailing list, or if the addressee is no longer employed by your organization, please notify AFGL/DAA, Hanscom AFB, MA 01731. This will assist us in maintaining a current mailing list.

Do not return copies of this report unless contractual obligations or notices on a specific document requires that it be returned.

UNCLASSIFIED

SECURITY CLASSIFICATION OF THIS PAGE

REPORT DOCUMENTATION PAGE

1a. REPORT SECURITY CLASSIFICATION
Unclassified

1b. RESTRICTIVE MARKINGS

2a. SECURITY CLASSIFICATION AUTHORITY

3. DISTRIBUTION/AVAILABILITY OF REPORT

2b. DECLASSIFICATION/DOWNGRADING SCHEDULE

Approved for public release; distribution unlimited.

4. PERFORMING ORGANIZATION REPORT NUMBER(S)

5. MONITORING ORGANIZATION REPORT NUMBER(S)

AFGL-TR-87-0158

6a. NAME OF PERFORMING ORGANIZATION

6b. OFFICE SYMBOL
(If applicable)

7a. NAME OF MONITORING ORGANIZATION

California Institute of Tech.
Seismological Laboratory

Air Force Geophysical Laboratory

6c. ADDRESS (City, State and ZIP Code)

7b. ADDRESS (City, State and ZIP Code)

Pasadena, California 91125

Hanscom Air Force Base, Massachusetts 01731

8a. NAME OF FUNDING/SPONSORING
ORGANIZATION8b. OFFICE SYMBOL
(If applicable)

9. PROCUREMENT INSTRUMENT IDENTIFICATION NUMBER

Advanced Research Projects Agency

F19628-85-K-0017

8c. ADDRESS (City, State and ZIP Code) (DOD)

10. SOURCE OF FUNDING NOS.

1400 Wilson Boulevard
Arlington, Virginia 22209PROGRAM
ELEMENT NO.PROJECT
NO.TASK
NO.WORK UNIT
NO.11. TITLE (Include Security Classification) Body and Surface
Wave Modeling of Observed Seismic Events (Part III)

61102F

5A10

DA

AA

12. PERSONAL AUTHOR(S)

Robert W. Clayton, David G. Harkrider and Donald V. Helmberger

1a. TYPE OF REPORT FINAL

13b. TIME COVERED

FROM 7/14/86 TO 1/13/87

14. DATE OF REPORT (Yr., Mo., Day)

5/13/87

15. PAGE COUNT

142

16. SUPPLEMENTARY NOTATION

17. COSATI CODES

FIELD GROUP SUB. GR.

18. SUBJECT TERMS (Continue on reverse if necessary and identify by block number)

2-D Kirchoff; modeling explosions in Yucca Basin NTS;
Rayleigh wave scattering to body wave coda; 2-D SH Green's
functions; effect of ocean path on Lg waves, seismic repre-
sentation theorem.

19. ABSTRACT (Continue on reverse if necessary and identify by block number)

The research performed under the contract, during the period 14 July 1986 through 13 January 1987, can be divided into two main topics; coupling line source calculations in 2-D lateral variations of near source structure to analytic teleseismic body wave codes, and the effects of ocean continent transition zones on L_g waves.

In section II, we present a new method for interfacing numerical and integral techniques which allows greater flexibility in seismic modeling. Specifically, numerical calculations in laterally varying structure are interfaced with analytic methods that enable propagation to great distances. Such modeling is important in studying situations contain-

20. DISTRIBUTION/AVAILABILITY OF ABSTRACT

UNCLASSIFIED/UNLIMITED ☐ SAME AS RPT. ☐ DTIC USERS ☐

21. ABSTRACT SECURITY CLASSIFICATION

Unclassified

22a. NAME OF RESPONSIBLE INDIVIDUAL

James Lewkowicz

22b. TELEPHONE NUMBER
(Include Area Code)

(617) 377-3028

22c. OFFICE SYMBOL

AFGL/LWH

→ing localized complex regions not easily handled by analytic means. The calculations involved are entirely two-dimensional, but use of an appropriate source and then a filter applied to the resulting seismograms produce synthetic seismograms which are point source responses in three dimensions. The integral technique is called two-dimensional Kirchhoff. Data from Yucca Flat, Nevada Test Site (NTS) are modeled as a demonstration of the usefulness of the new method. In this application, both local and teleseismic records are modeled simultaneously from the same model with the same finite-difference run. The application documents the importance of locally scattered Rayleigh waves in the production of teleseismic body wave complexity and coda.

In section III, the effects of the length of the intermediate path between the continent ocean and ocean continent transition regions is investigated. First the results of two FE calculations with different intermediate path lengths are presented and compared. These examples are contrasted with the path length used in the previous report. Then the RT integration method is discussed and explained. First analytic expressions for the stress components of double couple and line sources are derived, then the expressions for displacement and stress line source Green's functions are determined. These expressions are used to illustrate the validity and determine the accuracy of the RT coupling method. The RT coupling method is then used to continue the propagation of FE results through a layered structure using the displacement and stress Green's functions for the remaining path length and the displacement and stress time histories recorded at a column of element centers within the FE grid. The total attenuation of L_p due to propagation through a 2-D transition of continent to ocean to continent is found to be at most a factor of four to six. This is inadequate to explain the observed attenuation of L_p . Thus, additional effects, other than geometry must be considered to provide a complete explanation of the attenuation of L_p .

FINAL TECHNICAL REPORT
14 July 1986 - 13 January 1987

ARPA Order No.: 5299

Name of Contractor: California Institute of Technology

Effective Date of Contract: 14 January 1985

Contract Expiration Date: 13 January 1987

Contract Number: F19628-85-K-0017

Principal Investigators: Robert W. Clayton
(818) 356-6909

David G Harkrider
(818) 356-6910

Donald V. Helmberger
(818) 356-6998

Program Manager: James F. Lewkowicz
(617) 861-3028

Short Title of Work: Body and Surface Wave Modeling of
Observed Seismic Events

The views and conclusions contained in this document are those of the authors and should not be interpreted as necessarily representing the official policies, either expressed or implied, of the Defense Advanced Research Projects Agency of the U. S. Government

Sponsored by
Defense Advanced Research Projects Agency (DOD)
Defense Sciences Office, Geophysical Sciences Division
DARPA/DSO Physical Characterization of Seismic Sources
ARPA Order No. 5299.
Issued by the Air Force Geophysics Laboratory under
Contract# F19628-85-K-0017

Seismological Laboratory
Division of Geological and Planetary Sciences
California Institute of Technology
Pasadena, California 91125

Accession For	
NTIS - CRA&I	<input checked="checked" type="checkbox"/>
DTIC - TAB	<input type="checkbox"/>
Unannounced	<input type="checkbox"/>
Distribution	
By	
Distribution/	
Availability Codes	
Dist	Availability Codes
A-1	



TABLE OF CONTENTS

Summary	v
Numerical-analytical interfacing in two dimensions with applications to modeling NTS seismograms	1
Numerical studies of propagation of L_g waves across ocean continent boundaries using the representation theorem.	64
Chapter 3: Finite element to modal propagator matrix coupling; tests of accuracy and applications to transmission of L_g along partially oceanic paths	68

I. Summary

The research performed under the contract, during the period 14 July 1986 through 13 January 1987, can be divided into two main topics; coupling line source calculations in 2-D lateral variations of near source structure to analytic teleseismic body wave codes, and the effects of ocean continent transition zones on L_g waves.

In section II, we present a new method for interfacing numerical and integral techniques which allows greater flexibility in seismic modeling. Specifically, numerical calculations in laterally varying structure are interfaced with analytic methods that enable propagation to great distances. Such modeling is important in studying situations containing localized complex regions not easily handled by analytic means. The calculations involved are entirely two-dimensional, but use of an appropriate source and then a filter applied to the resulting seismograms produce synthetic seismograms which are point source responses in three dimensions. The integral technique is called two-dimensional Kirchhoff. Data from Yucca Flat, Nevada Test Site (NTS) are modeled as a demonstration of the usefulness of the new method. In this application, both local and teleseismic records are modeled simultaneously from the same model with the same finite-difference run. The application documents the importance of locally scattered Rayleigh waves in the production of teleseismic body wave complexity and coda.

In section III, the effects of the length of the intermediate path between the continent ocean and ocean continent transition regions is investigated. First the results of two FE calculations with different intermediate path lengths are presented and compared. These examples are contrasted with the path length used in the previous report. Then the RT integration method is discussed and explained. First analytic expressions for the stress components of double couple and line sources are derived, then the expressions for displacement and stress line source Green's functions are determined. These expressions are used to illustrate the validity and determine the accuracy of the RT coupling method. The RT coupling method is then used to continue the propagation of FE results through a layered structure using the displacement and stress Green's functions for the remaining path length and the displacement and stress time histories recorded at a column of element centers within the FE grid. The total attenuation of L_g due to propagation through a 2-D transition of continent to ocean to continent is found to be at most a factor of four to six. This is inadequate to explain the observed attenuation of L_g . Thus, additional effects, other than geometry must be considered to provide a complete explanation of the attenuation of L_g .

**Numerical-analytical interfacing in two dimensions
with applications to modeling NTS seismograms**

Richard J. Stead and Donald V. Helmberger

Seismological Laboratory

California Institute of Technology

Pasadena, CA 91125

March 27, 1986

*submitted to "Scattering and Attenuation of Seismic Waves",
special issue of Pure and Applied Geophysics*

suggested short title:

2d numerical-analytical interfacing

ABSTRACT

A new method for interfacing numerical and integral techniques allows greater flexibility in seismic modeling. Specifically, numerical calculations in laterally varying structure are interfaced with analytic methods that enable propagation to great distances. Such modeling is important in studying situations containing localized complex regions not easily handled by analytic means. The calculations involved are entirely two-dimensional, but use of an appropriate source and then a filter applied to the resulting seismograms produce synthetic seismograms which are point source responses in three dimensions. The integral technique is called two-dimensional Kirchhoff because its form is similar to classic three-dimensional Kirchhoff. Data from Yucca Flat, Nevada Test Site are modeled as a demonstration of the usefulness of the new method. In this application, both local and teleseismic records are modeled simultaneously from the same model with the same finite-difference run. This application documents the importance of locally scattered Rayleigh waves in the production of teleseismic bodywave complexity and coda.

Introduction

Seismologists have long recognized that structural complexities near seismic sources may affect teleseismic waveforms. For instance, events occurring in the Imperial Valley, California produce extended teleseismic short period signals lasting much longer than expected from near-in strong motion studies, see Hartzell and Heaton [1982]. Presumably, the energy trapped by the low-velocity layering scatters out the bottom of the basin when it encounters the basin edge. Recently, Vidale and Helmberger [1987a], using a finite-difference scheme, had considerable success at modeling a profile of the San Fernando earthquake strong motion records that cross the Los Angeles basin. Their approach assumes two-dimensional symmetry, as displayed in Figure 1, but corrects for three-dimensional spreading and mimics the well known double couple radiation field. Essentially, the numerical excitation is matched to an asymptotic analytical source representation. Synthetics generated by this procedure match closely those generated by analytical point source codes for the same flat layered case [Vidale, et al., 1985]. However, these solutions cannot be propagated to great distance because of computational efforts. Thus, a technique is needed to interface the numerical field back into an analytical scheme such that the signals can be sent to large distances. This is the basic objective of this paper, and we will also discuss, as a demonstration, a well controlled experiment where scattered surface waves can be seen leaving the local field to reappear as teleseismic body waves.

The most controlled experiment consistent with the above motivation above is that of explosions fired at Yucca Flat in the Nevada Test Site. The local structure of Yucca Flat is a basin containing volcanic tuffs and alluvium [Eckren, 1968 and Houser, 1968]. The events in this area have a striking complexity on teleseismic records for an explosion source (see Figure 2). Various studies show the structure of this region to be seismically complex [Taylor, 1983, among many others]. Hart, et al. [1979] examine the variation of amplitudes and magnitudes within Yucca Flat dependent on source position in the valley. Recent studies have concentrated on the azimuthal variations observed in the data in both the

time [Lay, Wallace and Helmberger, 1984] and frequency [Lay, 1986a] domains. Studies of these records have indicated the presence of local scattering structure [Lay, 1986b]. In addition, existing strong motion records demonstrate lateral anomalies in the propagation of seismic energy at Yucca Flat. Figure 3 shows the vertical velocity records from the event FLASK. The large difference in amplitude and duration of both the first arrivals and the Rayleigh waves from east to west strongly suggests that scattering plays an important role. It is found herein that these scattered Rayleigh waves are the likely progenitors of teleseismic complexity apparent in Figure 2. This is consistent with the results of Lynnes and Lay [1987], published in this issue.

A Two-Dimensional Representation Theorem

In accordance with the motivation discussed above, we derive a two-dimensional representation theorem method similar in its application to three-dimensional Kirchhoff integration. Such an integral method allows computationally inexpensive generation of teleseismic records from complex source region calculations, particularly those of finite difference. In deriving such a method, the resulting expression must be fully elastic, require a minimum of computation time, and be readily adaptable to finite-difference methods. A straightforward approach is to parallel the derivation of three-dimensional integration methods. For more information on such integral methods in both two and three dimensions see Baker and Copson [1950] and Mow and Pao [1971].

Starting with the two-dimensional elastic wave equation in polar coordinates,

$$\frac{\partial^2 u}{\partial r^2} + \frac{1}{r} \frac{\partial u}{\partial r} + \frac{1}{r^2} \frac{\partial^2 u}{\partial \theta^2} = \frac{1}{\alpha^2} \frac{\partial^2 u}{\partial t^2} \quad (1)$$

take the Laplace transform over time, ignoring the θ - dependence, and setting

$u=0, \frac{\partial u}{\partial t}=0$, at $t=0$, for all r, θ . Then,

$$\frac{\partial^2 \bar{u}}{\partial r^2} + \frac{1}{r} \frac{\partial \bar{u}}{\partial r} - \frac{s^2}{\alpha^2} \bar{u} = 0 \quad (2)$$

which has solutions like $K_0\left(\frac{sr}{\alpha}\right)$, see Hudson [1963] for example.

Thus, \bar{u} depends only on r and solves

$$\left(\nabla^2 - \frac{s^2}{\alpha^2}\right) \bar{u} = 0.$$

Let w be another solution of the Equation 2, then Green's transformation becomes

$$\begin{aligned} \int_{\Gamma} \left(\bar{u} \frac{\partial w}{\partial n} - w \frac{\partial \bar{u}}{\partial n} \right) dl &= \iint_D (\bar{u} \nabla^2 w - w \nabla^2 \bar{u}) dA \\ &= \iint_D \left(\bar{u} \frac{s^2}{\alpha^2} w - w \frac{s^2}{\alpha^2} \bar{u} \right) dA \\ &= 0. \end{aligned} \quad (3)$$

The geometry for this transformation is shown in Figure 4. Now let $w = K_0\left(\frac{sr}{\alpha}\right)$. Then for $P \notin D$,

$$\int_{\Gamma} \left[\bar{u} \frac{\partial}{\partial n} K_0\left(\frac{sr}{\alpha}\right) - K_0\left(\frac{sr}{\alpha}\right) \frac{\partial \bar{u}}{\partial n} \right] dl = 0. \quad (4)$$

For $P \in D$, as in Figure 5, the log singularity at P for $K_0\left(\frac{sr}{\alpha}\right)$ gives the result

$$\int_{\Gamma} \left(\bar{u} \frac{\partial w}{\partial n} - w \frac{\partial \bar{u}}{\partial n} \right) dl + \int_{\sigma} \left(\bar{u} \frac{\partial w}{\partial n} - w \frac{\partial \bar{u}}{\partial n} \right) dc = \iint_{D'} (\bar{u} \nabla^2 w - w \nabla^2 \bar{u}) dA = 0 \quad (5)$$

Let $\hat{n} = -\vec{r}/r$ in the integral over σ , then

$$\int_{\Gamma} \left(\bar{u} \frac{\partial w}{\partial n} - w \frac{\partial \bar{u}}{\partial n} \right) dl = \int_{\sigma} \left(\bar{u} \frac{\partial w}{\partial r} - w \frac{\partial \bar{u}}{\partial r} \right) dc \quad (6)$$

where dc is a length element on the circumference of the inner circle. Again, let $w = K_0$, and also let the radius, ϵ , of σ go to zero.

$$\int_{\Gamma} \left[\bar{u} \frac{\partial}{\partial n} K_0\left(\frac{sr}{\alpha}\right) - K_0\left(\frac{sr}{\alpha}\right) \frac{\partial \bar{u}}{\partial n} \right] dl = \lim_{\epsilon \rightarrow 0} \int_{\sigma} \left[\bar{u} \frac{\partial}{\partial r} K_0\left(\frac{sr}{\alpha}\right) - K_0\left(\frac{sr}{\alpha}\right) \frac{\partial \bar{u}}{\partial r} \right] dc \quad (7)$$

Near P, K_0 can be approximated as follows.

$$K_0\left(\frac{sr}{\alpha}\right) = \frac{\pi i}{2} H_0^{(1)}\left(\frac{sr}{\alpha}\right) \sim -\log r \quad (8)$$

$$\frac{\partial}{\partial r} K_0\left(\frac{sr}{\alpha}\right) \sim -\frac{1}{r} \quad (9)$$

If these approximations are substituted into the Equation 7, the integral over σ is evaluated in the limit.

$$\begin{aligned} \lim_{\epsilon \rightarrow 0} \int_{\sigma} \left[\bar{u} \frac{\partial}{\partial r} K_0\left(\frac{sr}{\alpha}\right) - K_0\left(\frac{sr}{\alpha}\right) \frac{\partial \bar{u}}{\partial r} \right] d\epsilon &= \lim_{\epsilon \rightarrow 0} - \int_{\sigma} \left(\frac{\bar{u}}{\epsilon} - \log \epsilon \frac{\partial \bar{u}}{\partial r} \right) d\epsilon \\ &= -2\pi \bar{u}(P) \end{aligned} \quad (10)$$

Therefore,

$$\bar{u}(P) = \frac{-1}{2\pi} \int_{\Gamma} \left[\bar{u} \frac{\partial}{\partial n} K_0\left(\frac{sr}{\alpha}\right) - K_0\left(\frac{sr}{\alpha}\right) \frac{\partial \bar{u}}{\partial n} \right] dl. \quad (11)$$

This integral can be exactly inverted to the time domain. First, take the derivative of K_0 .

$$\frac{\partial}{\partial n} K_0\left(\frac{sr}{\alpha}\right) = -\frac{s}{\alpha} K_1\left(\frac{sr}{\alpha}\right) \frac{\partial r}{\partial n} \quad (12)$$

Substitute this into the integral.

$$\bar{u}(P) = \frac{1}{2\pi} \int_{\Gamma} \left[\frac{s}{\alpha} \frac{\partial r}{\partial n} \bar{u} K_1\left(\frac{sr}{\alpha}\right) + \frac{\partial \bar{u}}{\partial n} K_0\left(\frac{sr}{\alpha}\right) \right] dl \quad (13)$$

Take the inverse transform.

$$\begin{aligned} u(P) &= \frac{1}{2\pi i} \int_{\gamma-i\infty}^{\gamma+i\infty} \frac{1}{2\pi} \int_{\Gamma} \left[\frac{s}{\alpha} \frac{\partial r}{\partial n} \bar{u} K_1\left(\frac{sr}{\alpha}\right) + \frac{\partial \bar{u}}{\partial n} K_0\left(\frac{sr}{\alpha}\right) \right] dl e^{st} ds \\ &= \frac{1}{2\pi} \int_{\Gamma} \frac{1}{2\pi i} \int_{\gamma-i\infty}^{\gamma+i\infty} \left[\frac{s}{\alpha} \frac{\partial r}{\partial n} \bar{u} K_1\left(\frac{sr}{\alpha}\right) + \frac{\partial \bar{u}}{\partial n} K_0\left(\frac{sr}{\alpha}\right) \right] dl e^{st} ds \end{aligned} \quad (14)$$

Inverting the above integral requires the use of the convolution rule, the

derivative rule and the inverse transforms

$$L^{-1}(K_0(bp)) [b > 0] = (t^2 - b^2)^{-1/2} H(t - b) \quad (15)$$

$$L^{-1}(K_1(bp)) [b > 0] = \frac{t}{b} (t^2 - b^2)^{-1/2} H(t - b). \quad (16)$$

Now, taking the inverse,

$$u(P) = \frac{1}{2\pi} \int_{\Gamma} \left[\frac{1}{\alpha} \frac{\partial r}{\partial n} \frac{d}{dt} \left(u * \left(\frac{\alpha t}{r} \frac{H(t - (r/\alpha))}{\sqrt{t^2 - (r/\alpha)^2}} \right) \right) + \frac{\partial u}{\partial n} * \left(\frac{H(t - (r/\alpha))}{\sqrt{t^2 - (r/\alpha)^2}} \right) \right] dt.$$

For simplicity, let $f(t) = (t^2 - (r/\alpha)^2)^{-1/2} H(t - (r/\alpha))$.

$$u(P) = \frac{1}{2\pi} \int_{\Gamma} \left[\frac{1}{r} \frac{\partial r}{\partial n} \frac{du}{dt} * (t \cdot f(t)) + \frac{\partial u}{\partial n} * f(t) \right] dt \quad (17)$$

Equation 17 may be cast in a form similar to that of conventional Kirchhoff methods. First apply the convolution identity $f(t) * g(t+c) = f(t+c) * g(t)$ with $c = -r/\alpha$.

$$u(P) = \frac{1}{2\pi} \int_{\Gamma} \left[\frac{1}{r} \frac{\partial r}{\partial n} \frac{du}{dt} * \left(\left(t + \frac{r}{\alpha} \right) f(t) \right) + \frac{\partial u}{\partial n} * f(t) \right] dt$$

where u is now $u(r)$, $r = t - r/\alpha$, the retarded time, and the operator

$f(t) = \frac{H(t)}{\sqrt{t} \sqrt{t + 2r/\alpha}}$. Rewriting this,

$$u(P) = \frac{1}{2\pi} \int_{\Gamma} \left[f(t) * \left(\frac{\partial u}{\partial n} + \frac{1}{\alpha} \frac{\partial r}{\partial n} \frac{\partial u}{\partial t} \right) + \left(t \cdot f(t) \right) * \frac{1}{r} \frac{\partial r}{\partial n} \frac{\partial u}{\partial t} \right] dt.$$

Bring the derivative across the convolution in the last term.

$$u(P) = \frac{1}{2\pi} \int_{\Gamma} \left[f(t) * \left(\frac{\partial u}{\partial n} + \frac{1}{\alpha} \frac{\partial r}{\partial n} \frac{\partial u}{\partial t} \right) + \left(\frac{1}{2\sqrt{t}} \frac{H(t)}{\sqrt{t + 2r/\alpha}} + \sqrt{t} \frac{d}{dt} \frac{H(t)}{\sqrt{t + 2r/\alpha}} \right) * \frac{u}{r} \frac{\partial r}{\partial n} \right] dt$$

Rearranging terms and taking the last time derivative,

$$u(P) = \frac{1}{2\pi} \int_{\Gamma} \left[f(t) * \left(\frac{\partial u}{\partial n} + \frac{u}{2r} \frac{\partial r}{\partial n} + \frac{1}{\alpha} \frac{\partial r}{\partial n} \frac{\partial u}{\partial t} \right) \right] dt - \frac{1}{2\pi} \int_{\Gamma} \left(\frac{t}{t + 2r/\alpha} f(t) \right) * \frac{u}{2r} \frac{\partial r}{\partial n} dt. \quad (18)$$

This equation is an exact form of the representation theorem.

It is useful to consider an approximation of Equation 18 for large r . The main reason for considering this is that $f(t)$ depends on r and therefore the convolution, which is computationally expensive, cannot be moved outside the integral. For large r , the operator $f(t)$ is dominated by $1/\sqrt{t}$, that is

$$f(t) = \frac{H(t)}{\sqrt{t} \sqrt{t + 2r/\alpha}} \sim \frac{H(t)}{\sqrt{t} \sqrt{2r/\alpha}}, \text{ and}$$

$$\frac{t}{t + 2r/\alpha} f(t) \sim H(t) \sqrt{t} (2r/\alpha)^{3/2}.$$

Equation 18 then becomes

$$u(P) = \frac{1}{2\pi} \frac{\sqrt{\alpha}}{\sqrt{2}} \frac{1}{\sqrt{t}} * \int_{\Gamma} \left[\frac{1}{\sqrt{r}} \left(\frac{\partial u}{\partial n} + \frac{u}{2r} \frac{\partial r}{\partial n} + \frac{1}{\alpha} \frac{\partial r}{\partial n} \frac{\partial u}{\partial t} \right) \right] dl$$

$$- \frac{1}{2\pi} \frac{\sqrt{\alpha}}{\sqrt{2}} \sqrt{t} * \int_{\Gamma} \frac{\alpha}{2r} \frac{1}{\sqrt{r}} \frac{u}{2r} \frac{\partial r}{\partial n} dl.$$

The second integral is similar to the second term in the first integral, except that it falls off as $1/r$ with respect to it. This means that the second integral may be ignored at large r .

$$u(P) = \frac{1}{2\pi} \frac{\sqrt{\alpha}}{\sqrt{2}} \frac{1}{\sqrt{t}} * \int_{\Gamma} \left[\frac{1}{\sqrt{r}} \left(\frac{\partial u}{\partial n} + \frac{u}{2r} \frac{\partial r}{\partial n} + \frac{1}{\alpha} \frac{\partial r}{\partial n} \frac{\partial u}{\partial t} \right) \right] dl \quad (19)$$

This approximation also arises from using the asymptotic form of K_0 before inverting the transform. That is,

$$K_0\left(\frac{sr}{\alpha}\right) \sim \frac{\sqrt{\pi\alpha}}{\sqrt{2sr}} e^{-\frac{sr}{\alpha}}. \quad (20)$$

Substitute Equation 20 into Equation 11, taking the appropriate derivatives, to get

$$\bar{u}(P) = \frac{1}{2} \frac{1}{\sqrt{2\pi}} \int_{\Gamma} \frac{\sqrt{\alpha}}{\sqrt{sr}} e^{-\frac{sr}{\alpha}} \left[\bar{u} \left(\frac{s}{\alpha} + \frac{1}{2r} \right) \frac{\partial r}{\partial n} + \frac{\partial \bar{u}}{\partial n} \right] dl. \quad (21)$$

This may be inverted using the shift rule to account for the $e^{-\frac{sr}{\alpha}}$, and

$L^{-1}(\sqrt{\pi/s}) = 1/\sqrt{t}$, to arrive at

$$u(P) = \frac{1}{2\pi} \frac{1}{\sqrt{2}} \frac{1}{\sqrt{t}} \int_{\Gamma} \left[\frac{\sqrt{\alpha}}{\sqrt{r}} \left(\frac{\partial u}{\partial n} + \frac{u}{2r} \frac{\partial r}{\partial n} + \frac{1}{\alpha} \frac{\partial r}{\partial n} \frac{\partial u}{\partial t} \right) \right] dl.$$

Once again, u is a function of retarded time $\tau = t - r/\alpha$, this time due to the application of the shift rule.

It is interesting to compare Equation 19 to the more familiar point source Kirchhoff formula from optics [see, for example, Baker and Copson, 1950].

$$u(P) = \frac{1}{4\pi} \iint_S \left(u \frac{d}{dn} \frac{1}{r} - \frac{1}{\alpha r} \frac{\partial r}{\partial n} \frac{\partial u}{\partial t} - \frac{1}{r} \frac{\partial u}{\partial n} \right) dS \quad (22)$$

which can be written

$$u(P) = \frac{1}{4\pi} \iint_S \frac{-1}{r} \left(\frac{\partial u}{\partial n} + \frac{u}{r} \frac{\partial r}{\partial n} + \frac{1}{\alpha} \frac{\partial r}{\partial n} \frac{\partial u}{\partial t} \right) dS \quad (23)$$

Comparing Equations 19 and 23, the form is identical between the integrals, except for a factor of two on the second term. The convolution with $1/\sqrt{t}$ and the difference in scaling with distance are expected for a line source as opposed to a point source. Both integrals can be applied in similar ways. Given a two-dimensional problem, the method of choice should be the line source integral.

An analytic verification of these formulae in a whole space demonstrates the operation of both the three-dimensional Kirchhoff formula and the two-dimensional integral just derived. The verification of the three-dimensional Kirchhoff formula is similar to that of Hilterman [1975] who set up a reflected case. The setup of the problem is given in Figure 6, where a plane (S) is assumed located equidistant between the source and receiver (that is, $r_0 = r$). Conceptually, the source lights up the surface, and the surface reradiates the energy to the receiver. In this case, the transmission coefficient is unity so that only geometrical effects are tested. Starting with the integral in Laplace space,

$$\bar{\phi}(P) = \frac{1}{4\pi} \iint_S e^{\frac{-\alpha r}{\alpha}} \left[\frac{1}{r} \frac{\partial \phi(S)}{\partial n} + \frac{\phi(S)}{r^2} \frac{\partial r}{\partial n} + \frac{1}{\alpha} \frac{\phi(S)}{r} \frac{\partial r}{\partial n} \right] dS \quad (24)$$

In this example, $\phi(P)$ is the potential at the observation point, and $\phi(s)$ is potential on the interface S . For a symmetric point source,

$$\phi(s) = \frac{1}{r_0} e^{-\frac{r_0}{\alpha}} \bar{f}(s) \quad (25)$$

Applying the chain rule to $\frac{\partial \phi(s)}{\partial n}$,

$$\frac{\partial \phi(s)}{\partial n} = \frac{\partial \phi(s)}{\partial r_0} \frac{\partial r_0}{\partial n} = - \left(\frac{s}{\alpha} + \frac{1}{r_0} \right) \frac{\partial r_0}{\partial n} \phi(s) \quad (26)$$

Substituting Equations 25 and 26 into Equation 24 yields

$$\bar{\phi}(P) = \bar{f}(s) \frac{1}{4\pi} \iint_S \frac{1}{r_0} e^{-\frac{r_0}{\alpha}} e^{-\frac{r}{\alpha}} \left[-\frac{1}{r} \left(\frac{s}{\alpha} + \frac{1}{r_0} \right) \frac{\partial r_0}{\partial n} + \frac{1}{r^2} \frac{\partial r}{\partial n} + \frac{s}{\alpha} \frac{1}{r} \frac{\partial r}{\partial n} \right] dS \quad (27)$$

Let $r_0 = r$, $\frac{\partial r_0}{\partial n} = -\frac{\partial r}{\partial n}$ and $d\Omega = \frac{1}{r^2} \frac{\partial r}{\partial n} dS$, where Ω is solid angle. Then

$$= \bar{f}(s) \frac{1}{2\pi} \int_{\Omega} e^{-\frac{2r}{\alpha}} \left(\frac{s}{\alpha} + \frac{1}{r} \right) d\Omega$$

Let $t = 2r/\alpha$, $t_0 = 2r_0/\alpha$ and $d\Omega = \frac{d\Omega}{dt} dt$.

$$\bar{\phi}(P) = \bar{f}(s) \frac{1}{2\pi} \int e^{-t} \left(\frac{s}{\alpha} + \frac{2}{\alpha t} \right) \frac{d\Omega}{dt} dt$$

Invert to the time domain.

$$\phi(P) = \frac{1}{2\pi} \left[\frac{1}{\alpha} \frac{d^2 \Omega}{dt^2} + \frac{2}{\alpha t} \frac{d\Omega}{dt} \right] * f(t) \quad (28)$$

The solid angle swept out over the surface as a function of time is

$$\Omega(t) = 2\pi \left(1 - \frac{t_0}{t} \right) H(t - t_0)$$

$$\frac{d\Omega}{dt} = 2\pi \frac{t_0}{t^2} H(t - t_0)$$

$$\frac{d^2 \Omega}{dt^2} = 2\pi \frac{t_0}{t^2} \delta(t - t_0) - 4\pi \frac{t_0}{t^3} H(t - t_0)$$

Using these expressions, Equation 28 becomes

$$\begin{aligned}
 \phi(P) &= \frac{1}{2\pi\alpha} \left(2\pi \frac{t_0}{t^2} \delta(t-t_0) - 4\pi \frac{t_0}{t^3} H(t-t_0) + \frac{2}{t} 2\pi \frac{t_0}{t^2} H(t-t_0) \right) * f(t) \\
 &= \frac{1}{\alpha} \frac{t_0}{t^2} \delta(t-t_0) * f(t) \\
 &= \frac{1}{\alpha} \frac{f(t-t_0)}{t_0} \\
 &= \frac{1}{R} f(t-t_0)
 \end{aligned} \tag{29}$$

This is the familiar geometric spreading law for a point source.

The same analysis can be performed in two dimensions (see Figure 7). The approximate form of the integral, as given in Equation 19, is used because the form is more like that of the three-dimensional case, and the analysis is more straightforward. For an appropriate correspondence, replace \ast inside the integral of Equation 19 with $\phi(r)$, the potential on the contour Γ . As above, starting with the Laplace transform of the integral (Equation 21), use the approximate form of the source (see Equation 20).

$$\phi(r) = \frac{\sqrt{\pi\alpha}}{\sqrt{2\pi r_0}} e^{\frac{-\pi r_0}{\alpha}} \bar{f}(s) \tag{30}$$

$$\frac{\partial \phi(r)}{\partial n} = -\frac{\sqrt{\pi\alpha}}{\sqrt{2\pi r_0}} \left(\frac{1}{2r_0} + \frac{s}{\alpha} \right) e^{\frac{-\pi r_0}{\alpha}} \frac{\partial r_0}{\partial n} \bar{f}(s) \tag{31}$$

Substitute these into Equation 21 to obtain

$$\bar{\phi}(P) = \bar{f}(s) \frac{1}{2} \frac{1}{\sqrt{2\pi}} \int_{\Gamma} \frac{\sqrt{\alpha}}{\sqrt{sr}} \frac{\sqrt{\pi\alpha}}{\sqrt{2\pi r_0}} e^{\frac{-\pi r}{\alpha}} e^{\frac{-\pi r_0}{\alpha}} \left[\left(\frac{s}{\alpha} + \frac{1}{2r} \right) \frac{\partial r}{\partial n} - \left(\frac{s}{\alpha} + \frac{1}{2r} \right) \frac{\partial r_0}{\partial n} \right] dl \tag{32}$$

Let $r_0=r$, $\frac{\partial r_0}{\partial n} = -\frac{\partial r}{\partial n}$ and $d\theta = \frac{1}{r} \frac{\partial r}{\partial n} dl$, where θ measures the angle from vertical, as indicated in Figure 7. Then

$$\bar{\phi}(P) = \bar{f}(s) \frac{1}{4} \int_{\Gamma} \frac{\alpha}{sr} e^{\frac{-2\pi r}{\alpha}} 2 \left(\frac{s}{\alpha} + \frac{1}{2r} \right) \frac{\partial r}{\partial n} dl$$

$$= \bar{f}(s) \frac{1}{2} \int_{t_0}^t \frac{\alpha}{s} e^{-\frac{2\sigma r}{\alpha}} \left[\left(\frac{s}{\alpha} + \frac{1}{2r} \right) \right] d\theta$$

Let $t = 2r/\alpha$, $t_0 = 2r_0/\alpha$ and $d\theta = \frac{d\theta}{dt} dt$.

$$\bar{\phi}(P) = \bar{f}(s) \frac{1}{2} \int e^{-st} \left(1 + \frac{1}{st} \right) \frac{d\theta}{dt} dt$$

Invert to the time domain.

$$\phi(P) = \frac{1}{2} \left[\frac{d\theta}{dt} + \int_0^t \frac{1}{\tau} \frac{d\theta}{d\tau} d\tau \right] H(t-t_0) * f(t) \quad (33)$$

The total angle swept out over the contour as a function of time is

$$\theta(t) = 2 \cos^{-1} \left(\frac{t_0}{t} \right) H(t-t_0)$$

$$\frac{d\theta}{dt} = 2 \frac{t_0}{t} \frac{H(t-t_0)}{\sqrt{t^2 - t_0^2}}$$

Using these expressions, Equation 33 becomes

$$\begin{aligned} \phi(P) &= \left[\frac{t_0}{t} \frac{H(t-t_0)}{\sqrt{t^2 - t_0^2}} + \int_0^t \frac{1}{\tau} \frac{t_0}{\tau} \frac{H(t-t_0)}{\sqrt{\tau^2 - t_0^2}} d\tau \right] H(t-t_0) * f(t) \\ &= \left[\frac{t_0}{t} \frac{H(t-t_0)}{\sqrt{t^2 - t_0^2}} + t_0 \int_{t_0}^t \frac{d\tau}{\tau^2 \sqrt{\tau^2 - t_0^2}} d\tau \right] H(t-t_0) * f(t) \\ &= \left[\frac{t_0}{t} \frac{1}{\sqrt{t^2 - t_0^2}} + t_0 \frac{\sqrt{\tau^2 - t_0^2}}{t_0^2 \tau} \right]_{t_0}^t H(t-t_0) * f(t) \\ &= \frac{t_0^2 + t^2 - t_0^2}{t_0 t \sqrt{t^2 - t_0^2}} H(t-t_0) * f(t) \\ &= \frac{t}{t_0} \frac{H(t-t_0)}{\sqrt{t^2 - t_0^2}} * f(t) \end{aligned}$$

Now, let $t \sim t_0$.

$$\phi(P) = \frac{H(t-t_0)}{\sqrt{t^2-t_0^2}} * f(t) \quad (34)$$

This is the familiar equation for line source response. Note that in the three-dimensional point source case, $d\Omega/dt = 0$ until $t=t_0$, and then jumps to $2\pi/t_0$ at $t=t_0$, gradually decreasing with time thereafter. An interface with structure behaves in a more interesting manner, see Scott and Helmberger [1984]. In two dimensions, $d\theta/dt$ has a square root singularity at $t=t_0$. In the three-dimensional extension of this case, the response at $t=t_0$ represents the integrated energy arriving at the receiver from an infinite strip represented by the first line element. It is the integration over this infinite strip in and out of the plane of Figure 7 that creates the singularity.

The simplest application of two-dimensional Kirchhoff is to a medium of constant velocity set in Cartesian coordinates, with part of the contour, Γ , parallel to one of the axes (Figure 8). Choosing a boundary paralleling the x -axis in an (x, z) system and extending to infinity in both directions, the contour Γ may be closed at $r = \infty$ in the direction $z = +\infty$. As $r \rightarrow \infty$, the integral over this closure of Γ vanishes. The point P becomes the receiver location, and all sources are outside the contour. The vector \vec{r} has its origin at P and is the distance to Γ . From this information, $\hat{n} = -\hat{z}$ on the straight boundary, $\frac{\partial r}{\partial n} = \frac{z}{r}$ and $\frac{\partial}{\partial n} = -\frac{\partial}{\partial z}$. For this case, the integral from Equation 19 becomes

$$u(P) = \frac{1}{2\pi} \frac{\sqrt{\alpha}}{\sqrt{2}} \frac{1}{\sqrt{t}} * \int_{-\infty}^{\infty} \left[\frac{1}{\sqrt{r}} \left(-\frac{\partial u}{\partial z} + u \frac{z}{2r^2} + \frac{z}{r\alpha} \frac{\partial u}{\partial t} \right) \right] dl. \quad (35)$$

For computation, the integral must be discretized to a finite sum. Assuming that the contributions from the ends of the boundary are small,

$$u(P) = \frac{h}{2\pi} \frac{\sqrt{\alpha}}{\sqrt{2}} \frac{1}{\sqrt{t}} * \sum_{i=1}^N \left[\frac{1}{\sqrt{r_i}} \left(-\frac{\partial u}{\partial z} + u \frac{z}{2r_i^2} + \frac{z}{r_i\alpha} \frac{\partial u}{\partial t} \right) \right]. \quad (36)$$

where h is the spacing between discrete line elements. If the coordinates of P are

x_P , y_P , and the coordinates of the first line element are x_1 , y_1 , then $x = x_P - x_1$, $y = y_P - y_1 - (i-1)h$ and $r_i = \sqrt{x_i^2 + y^2}$.

The above geometry is developed specifically for application with finite-difference techniques. For the acoustic case, the wave field u becomes pressure (or dilatation, Θ), and Equation 36 is directly applicable. For the elastic case, some modifications must be made. Assuming continuous material properties across the boundary, the compressional and shear wave fields may be separated. Separating these fields following a fully elastic finite-difference calculation requires the taking of the divergence and curl of the full wave displacement field for the compressional and shear components, respectively. This can be seen from the potential form of the vector displacements, $\underline{u} = \nabla\phi + \nabla \times \underline{\psi}$. First, take the divergence, $\nabla \cdot \underline{u} = \nabla \cdot \nabla\phi$, and take the curl, $\nabla \times \underline{u} = \nabla \times \nabla \times \underline{\psi}$. Take divergence and curl, respectively, a second time. Two equations now exist, one in which u is identified as the second spatial derivative of the compressional wave field with velocity α as the p-wave velocity, and a second in which u is identified as the second spatial derivative of the shear wave field with velocity α as the s-wave velocity, β . Returning to the wave equation, the reason for the second derivatives becomes evident. The wave equations for the second derivatives of displacement are

$$\nabla^2 \underline{u}_p = \frac{1}{\alpha^2} \frac{\partial^2 \underline{u}_p}{\partial t^2}$$

$$\nabla^2 \underline{u}_s = \frac{1}{\beta^2} \frac{\partial^2 \underline{u}_s}{\partial t^2}$$

Identifying the wave field u in Equation 19 as the second derivatives of the vector displacements \underline{u}_p and \underline{u}_s , the wave equations allow the second spatial derivatives of $\underline{u}_p(P)$ and $\underline{u}_s(P)$ to be equated to second time derivatives, that is accelerations. Thus, Equation 19 becomes two integrals, one for the p-wave field and another for the s-wave field, in each of which the required inputs are spatial derivatives of displacement (calculated in the finite-difference code), and the outputs are accelerations.

Normally, when calculating a teleseismic record in this manner, elastic or acoustic, a point source in three-dimensional geometry is the response desired. An appropriate approximate conversion, derived in Appendix A, is

$$U_{\text{point}} = \frac{2}{\sqrt{R} + \sqrt{z}} \frac{1}{\sqrt{t}} * \frac{d}{dt} U_{\text{line}}. \quad (\text{A.28})$$

Here, z is the horizontal distance (as in the above derivation), and R is the total distance ($\sqrt{z^2 + z^2}$) from the source to the receiver. This conversion assumes cylindrical symmetry about a vertical axis through the source. If it is applied directly to Equation 36, the result is as follows.

$$u(P) = \frac{h}{2\pi} \frac{\sqrt{\alpha}}{\sqrt{2}} \frac{2}{\sqrt{R} + \sqrt{z}} \frac{d}{dt} \frac{1}{\sqrt{t}} * \frac{1}{\sqrt{t}} * \sum_{i=1}^N \left[\frac{1}{\sqrt{r_i}} \left(-\frac{\partial u}{\partial z} + u \frac{z}{2r_i^2} + \frac{z}{r_i \alpha} \frac{\partial u}{\partial t} \right) \right].$$

This equation can be simplified by recognizing that

$$\begin{aligned} \frac{d}{dt} \frac{1}{\sqrt{t}} * \frac{1}{\sqrt{t}} * F(t) &= \frac{d}{dt} \pi H(t) * F(t) \\ &= \pi \delta(t) * F(t) \\ &= \pi F(t) \end{aligned}$$

Then

$$u(P) = \frac{h}{\sqrt{R} + \sqrt{z}} \frac{\sqrt{\alpha}}{\sqrt{2}} \sum_{i=1}^N \left[\frac{1}{\sqrt{r_i}} \left(-\frac{\partial u}{\partial z} + u \frac{z}{2r_i^2} + \frac{z}{r_i \alpha} \frac{\partial u}{\partial t} \right) \right]. \quad (37)$$

This conversion assumes the original line source radiation pattern was appropriately adjusted for conversion to point source, as discussed in Appendix A.

Many assumptions are made in the above derivation. While the justifications given are reasonable, some simple tests of the method against other analytical methods is useful. Suppose we examine a simple half-space with a point source at a depth of 1 km in an elastic half space with p-velocity 4 km/s, s-velocity 2.3 km/s and density 2.7 g/cc, and receivers at a depth of 6 km and a variety of ranges. A comparison of the new method, finite-difference and

Cagniard seismograms is shown in Figure 9. The seismograms shown include an RDP source convolved with a Gaussian. The Gaussian is necessary in the finite-difference scheme to limit the bandwidth of the source to a range in which propagation is stable. The Gaussian is normalized to have an integral of unity. The records shown are all velocity records, representative of the response of a broad band strong motion instrument. The response at the surface for finite differences and Cagniard are compared in Figure 10, demonstrating the usefulness of finite differences in modeling strong motions.

The synthetics for small ranges have not been included in either Figure 9 or 10, because the line to point source mapping approximation breaks down at near vertical take-off angles, see Appendix A. The parameter k , used in the mapping, is fixed at 0.6 throughout this investigation, because it seems to give good agreement to other synthetic methods (Figures 9 and 10) at the take-off angles of interest in this study.

Canonical basin models

Having demonstrated, briefly, the accuracy of the finite-difference and two-dimensional Kirchhoff methods, it is now appropriate to examine some canonical models of basins, to understand what effects various geometries may have. Four models of basin boundaries are shown in Figure 11; they are variations of a layer over a half space. The half space parameters are p -velocity 4.6 km/s, s -velocity 2.7 km/s, and density 2.7 g/cc; and are representative of crystalline rock. The layer parameters are chosen to give a p -velocity ratio of one to two, with the other parameters appropriate for a sediment with that p -velocity; p -velocity 2.3 km/s, s -velocity 1.1 km/s, density 2.0 g/cc. The source is fixed 3.75 km from the basin boundary at a depth of 0.75 km in each case. Surface strong motions are computed at one km intervals from the source to the edge of the model and compared with the uniform layer over a half space model. Examination of the strong motions in Figure 12 shows some of the differences between the four basin termination models. Both of the sharper basin terminations pass more energy across

the termination; the gradual terminations allow waves of only about half the amplitude to pass across. Nevertheless, all the models of basin termination cause large drops in amplitude as the wavefronts cross the boundary. Part of this energy is reflected back across the basin (this energy cannot be corrected to three dimensions properly and will have higher than its true amplitude, especially as it approaches the source position), but much of it is scattered to teleseismic distances. The surface waves are not well-developed here because there is no low-velocity surface layer to reduce the direct wave and enhance amplitude and duration of the Rayleigh wave. The primary conclusion to be drawn from the strong motions is that gradual basin terminations will have the greatest effect on energy crossing that boundary, but that all large contrasts across great changes in basin depth will cause large reductions in transmitted strong motion amplitudes.

Now, using the two-dimensional Kirchhoff technique derived above, the scattered energy may be examined at teleseismic distances. Figure 13 shows the teleseismic p-wave seismograms computed at a distance through the half-space of 1000 km from the source. These displacement records include the RDP source, a WWSSN short-period instrument response and attenuation with T^* of one. The seismograms are all normalized to the flat-layer response (ie: the response if the model at the source were extended laterally without termination). The distance of 1000 km is sufficient for these half-space teleseismic calculations because it is two orders of magnitude greater than the length of the integration contour, and therefore the waveform will no longer change with distance, only the amplitude will change by geometric spreading. This will be discussed more fully later. Differences in the synthetics for the various models consist primarily of small amplitude changes at the frequencies involved here. Even broad band responses do not show large changes in teleseismic records (Figure 14). This indicates that at teleseismic distances, for explosions, velocity contrast at the boundary and the overall dimensions of the boundary are of primary importance, not the precise shape of the boundary. On the other hand, increasing the amplitude and duration of the surface wave before it interacts with the boundary increases the

overall effect on the teleseismic waveform and increases the variation with boundary geometry, as we will show later.

Some of this scattered energy is also found as teleseismic sv-waves. Figure 15 shows the s-wave responses at the same teleseismic distances. These waves are of the same order of magnitude in amplitude as the scattered p-waves. Also, because they are not dominated by P and pP (pS is small at near vertical take-off angles), they show a great deal more variation with the type of boundary chosen. Such high amplitude scattered sv-waves could complicate the analysis of sources such as earthquakes which generate direct s-waves, but these waves could be important when studying explosions, which can only generate sv-waves through structural interaction.

In demonstration of how two-dimensional Kirchhoff constructs the teleseismic waveform, Figure 16 shows a series of synthetic velocity seismograms at four take-off angles (5, 10, 15 and 20 degrees) for five cases in which more of the line elements along the contour are included in each subsequent calculation. That is, case 0 includes contributions from the single line element at 17 degrees take-off angle. Case 1 includes the two nearest neighbors, case 2 includes 11 elements, case 3 includes 25, and case 4 includes all elements. Up to case 2, the P-pP arrivals increase by addition of energy from a narrow range of angles providing energy propagating away from the very near vicinity of the source. Energy scattered from structure is not propagating in the direction of the receivers over this portion of the contour. The elements used in case 2 should include most the energy for the P-pP arrival, and remaining contributions to that phase are small, as seen by comparing peak amplitudes in the remaining cases. Case 3 is the first to include significant energy from scattering. Notice that the contour elements included in case three contain all contributions from the basin boundary up to 20 degrees take-off angle. For this reason, the contributions from the remaining elements are small and the records for case 4 differ little from those of case 3.

Figure 17 demonstrates the effect of distance on the resulting seismograms. At the smaller distances of 5 and 10 km, cases 0 and 1, the contribution from scattering propagates at a greatly different angle than the energy from the source. For receivers below the source, the scattered energy is small because it is propagating backward off the scatterer. Further from the source, at distances of 100 and 1000 km, cases 2 and 3, there is little difference between records at different distances because the take-off angles from the source and the scatterer become indistinguishable. Source and scatterer become one. These synthetic seismograms contain only the p-waves; if the s-waves were included, the records at 5 and 10 km would become very complicated and would differ greatly from those at teleseismic distances.

Application - Events at Yucca Flat, NTS

Since near source structural interaction causes variations in teleseismic waveforms due to surface wave interaction, records of this scattering are likely to be quite common. Yucca Flat at NTS, Nevada is one example of a structure that may generate these effects. The lateral variation in the Yucca Flat area is due to the basin structure of the valley. Sources at NTS are typically located near the center of the valley, three to five kilometers from the basin termination. As shown in the canonical models of basins above, this situation will cause strong interaction of the surface wave with the basin boundary. At the surface, the amplitude of the surface wave will be reduced and the frequency content will change as the wave encounters hard rock.

As discussed above, the two-dimensional methods used in this investigation produce a three-dimensional response from point sources. The conversion derived in Appendix A requires that the source used to drive the finite-difference scheme include higher order (non-isotropic) line source terms [Vidale and Helmberger, 1986]. For an explosion, these terms have radiation patterns such that the response is correct only from half the source. In the modeling below, the structure in the invalid direction is restricted to flat layers. The result of this

modeling is a structure which is locally cylindrical, because the response in and out of the plane and in the invalid direction is flat layered and has no effect on the seismograms produced.

Figure 18 is a map of Yucca Flat that shows the outlines of the hard rock outcrops which approximately mark the the basin boundary. Also displayed are the various event locations and a network of strong motion recorders for one event (FLASK). Note that the locally cylindrical geometry is appropriate here, especially in the direction of the WWSSN station MAT, Japan. The line AB marks the location of a cross-section shown in Figure 19. The cross-section is a view looking south, and the positions of various sources and receivers used in this study are shown. The dashed line is the integration contour for the two-dimensional Kirchhoff. There are three materials in this model: low-velocity alluvium, volcanic tuffs, and hard rock (Cretaceous granites and Paleozoic rocks). The large differences between the velocities of these materials is what makes lateral variation important.

The local cylindrical symmetry of the resulting model is shown in Figure 20. The source falls on the axis of the cylinder, and the line source to point source conversion is valid only in the direction of the basin boundary. The seismograms generated for the source positions indicated are responses for this three-dimensional geometry.

Figure 3 shows some of the strong motion data from the FLASK event. Both the locations of the receivers and the location of the event are shown on the map of Figure 18. The data shown in the figure are vertical velocity records from stations three to four kilometers from the event. The basin becomes shallow between the source and the position of the westernmost stations, creating a geometry where the stations closest to the source see a distant basin boundary, while those to the west see a basin boundary directly below. In the figure, the differences between the two directions is readily apparent. To the west, the amplitudes of surface waves are reduced by roughly half with respect to those to

the east. It also appears that the longer period surface waves are reduced more than shorter period waves. It will be shown that the energy lost from the surface waves is converted to body waves and is found on teleseismic records.

Some strong motion synthetics for a source at position 1 are shown in Figure 21. Notice that as the Rayleigh wave encounters the basin boundary, the amplitude becomes roughly half and the longer period surface waves are greatly reduced. The source parameters mentioned in the figure are used in a Helmburger and Hadley [1981] reduced displacement potential. This RDP source is approximately that expected for FLASK and similar events in Yucca Flat, and is used throughout this investigation as a representative source description.

Direct comparisons of various source-receiver pairs and the data are given in Figure 22. The data have more energy in the higher frequencies due to limitations of the finite-difference method. Finite grid spacing results in a maximum frequency which can be propagated accurately. Therefore, the source used is convolved with a Gaussian window to remove higher frequencies. Nevertheless, the absolute amplitudes and many of the primary features of each record are accurately modeled. The record for station 795, is best modeled by a source at position 2 (out of positions 0 through 3 spaced one kilometer apart) at a distance of three kilometers. This is one of the better waveform fits produced by the model. Station 791 is best modeled by a source at position 3 (closest to the basin boundary) at a distance of 3.5 kilometers. Stations 791, 793 and 795 are north and east of the event. This is the range of directions, as argued from the map of Figure 18, which is most like a locally cylindrical geometry. Station 789 is to the south. Here, the basin boundary is further from the source. Thus, source position 0 gives the most accurate result.

Now the two-dimensional Kirchhoff may be applied to see if this model is consistent also with the teleseismic data. Figure 2 shows the data set to be considered here. These are short period WWSSN records recorded at station MAT, Japan. Seven different events from various sites within the valley are shown.

Notice the additional energy arriving after P-pP. This energy is present at very large amplitudes on all records except PORTMANTEAU. PORTMANTEAU occurred at the basin boundary to the northeast and therefore may be considered primarily a flat layer case. Note also that while P-pP is similar for all the events, the later phases vary substantially as a function of position. Yet when sources are close together (KEELSON and OSCURO), differences are small.

Figure 23 shows some of the two-dimensional Kirchhoff results. These are point source displacement records and have been convolved with a WWSSN short period instrument response and a Q-operator with $T^*=1$. Take off angles of 15° and 20° were chosen to bracket that appropriate for MAT (17.8°). All amplitudes are relative to the flat layer case at a take-off angle of 0° (the flat layer record shown is at 15°). The important observation here is that the records vary far more by moving the source one kilometer within the basin than by changing the take-off angle by five degrees. The energy which causes the waveform variations comes from the conversion of surface wave energy at the basin boundary. Figure 24 shows a direct comparison of the data and model. KEELSON and OSCURO are modeled accurately by the same synthetic record, demonstrating repeatability, and the flat layer comparison with PORTMANTEAU is good as expected.

Discussion and Conclusions

This paper presents a new method for calculating teleseismic waveforms, using an interface of numerical and analytic computations. As presented, the two-dimensional Kirchhoff method relies entirely on local structural effects to change the teleseismic waveform. This method can be made computationally fast and efficient. Using anisotropic sources and filtering the resulting seismograms produce three dimensional, point source records. The finite-difference calculation produces both surface strong motion records and the functions needed for the teleseismic synthetics. In this way, a model of local structure can be compared with both local and teleseismic data simultaneously.

In this paper, we concentrated on the local structural effects in modeling teleseismic waveforms. More realistic path effects can be included in the calculations by modifying Equation 39 using a convolution with an appropriate kernel computed by various analytical ray techniques. Such interfacing would be useful, for example, in modeling the complexities observed by Lynnes and Lay [1987] (also on this issue). This problem will be addressed in future publications.

The case for using only local structure in the teleseismic calculation is strong for Yucca Flat because the local strong motion and teleseismic data are modeled simultaneously. Only the local structure need be considered to make a good synthetic strong motion seismogram. If a local structure models well both the strong motion records and the teleseismic records then the effect of local structure on the teleseismic waveform is substantiated. A relatively simple model of the basin at Yucca Flat produces synthetic seismograms which match very well those observed at teleseismic and local distances. Several features of these records are explained. The variation of surface wave amplitude with azimuth is shown to be the result of interaction with the basin boundary. A drop in amplitude across the basin boundary occurs as surface wave energy is converted to body waves. These scattered phases are observed on teleseismic records shortly after P-pP.

ACKNOWLEDGEMENTS

This work was supported by the Geophysical Sciences Division of the Air Force Geophysics Laboratory under Contract Number F19628-85-K-0017 and monitored by the Defense Advanced Research Projects Agency. Gladys Engen and John Vidale reviewed the manuscript. John Vidale provided the finite-difference code used. Contribution number 4464 from the Division of Geological and Planetary Sciences, California Institute of Technology, Pasadena, California, 91125.

References

- Baker, B.B. and E.T. Copson, *The Mathematical Theory of Huygens' Principle*, Oxford University Press, London, pp. 36-53, 1950.
- Eckren, E.B., Geologic setting of Nevada Test Site and Nellis Air Force Range, in *Nevada Test Site, GSA Memoir 110*, E.B. Eckel, ed., pp. 21-33, 1968.
- Hart, R.S., D.M. Hadley, G.R. Mellman and R. Butler, Seismic amplitude waveform research, Final Technical Report SGI-R-79-012, Sierra Geophysics, 1979.
- Hartzell, S., and T. Heaton, Inversion of strong ground motion and teleseismic waveform data for the fault rupture history of the 1979 Imperial Valley, California earthquake., *Bull. Seism. Soc. Am.*, **73**, 1553-1583, 1983.
- Haskell, N., Analytic approximation for the elastic radiation from a contained underground explosion, *J. Geophys. Res.*, **72**, 2583-2597, 1967.
- Hays, W.W. and T.R. Murphy, The effect of Yucca Fault on seismic wave propagation, Report NVO-1163-TM-19, Environmental Research Corporation, 1970.
- Helmberger, D.V. and D.M. Hadley, Seismic source functions and attenuation from local and teleseismic observations of the NTS events Jorum and Handley, *Bull. Seism. Soc. Am.*, **71**, 51-67, 1981.
- Hilterman, F.J., Amplitudes of seismic waves - a quick look, *Geophysics*, **40**, 745-762, 1975.
- Houser, F.N., Application of geology to underground nuclear testing, Nevada Test Site, in *Nevada Test Site, GSA Memoir 110*, E.B. Eckel, ed., pp. 11-19, 1968.
- Hudson, J.A., SH waves in a wedge-shaped medium, *Geophys. J. Roy. Astron. Soc.*, **7**, 517-546, 1963.
- Lay, T., Analysis of near-source contributions to early P-wave coda for underground explosions: 2. frequency dependence, submitted to *Bull. Seism.*

- Soc. Am.*, 1986a.
- Lay, T., Analysis of near-source contributions to early P-wave coda for underground explosions: 3. inversion for isotropic scatterers, submitted to *Bull. Seism. Soc. Am.*, 1986b.
- Lay, T., T.C. Wallace and D.V. Helmberger, Effect of tectonic release on short period P waves from NTS explosions, *Bull. Seism. Soc. Am.*, 74, 819-842, 1984.
- Mow, C.C. and Y.H. Pao, *The Diffraction of Elastic Waves and Dynamic Stress Concentrations*, Report R-482-PR for United States Air Force Project Rand, Santa Monica, CA, pp. 140-171, 1971.
- Scott, P. and D. Helmberger, Applications of the Kirchhoff-Helmholtz integral to problems in seismology, *Geophys. J. Roy. Astron. Soc.*, 72, 237-254, 1983.
- Springer, D.L. and R.L. Kinnaman, Seismic source summary for U.S. underground Nuclear Explosions, 1961-1970, *Bull. Seism. Soc. Am.*, 61, 1073-1098, 1971.
- Taylor, R.T., Three-dimensional crust and upper mantle structure at the Nevada Test Site, *J. Geophys. Res.*, 88, 2220-2232, 1983.
- Vidale, J.E., Application of two-dimensional finite-differencing methods to simulation of earthquakes, earth structure, and seismic hazard, thesis, Calif. Institute of Tech., 1986.
- Vidale, J.E. and D.H. Helmberger, Elastic finite-difference modeling of the 1971 San Fernando, Ca. earthquake, submitted to *Bull. Seism. Soc. Am.*, 1987a.
- Vidale, J.E. and D.H. Helmberger, On modeling explosions using 2-d numerical methods, in preparation for *Bull. Seism. Soc. Am.*, 1987b.
- Vidale, J.E. and D.H. Helmberger, Path effects in strong motion seismology, chapter 6 in *Methods of Computational Physics*, Bruce Bolt, ed., 267-319, 1987c.
- Vidale, J., D.V. Helmberger, and R.W. Clayton, Finite-difference seismograms

for SH waves, *Bull. Seism. Soc. Am.*, 75, 1765-1782, 1985.

West, L.R. and R.K. Christie, Observed seismic data FLASK event, Report
NVO-1163-233, Environmental Research Corporation, 1971.

Appendix A: Analytic source function for 2d finite difference

Asymptotic source theory produces p-wave point source displacement potentials in three dimensions of the following forms, assuming a step function source [Helmberger, 1983]

$$\phi_p(x, z, t) = \frac{\sqrt{2}}{\pi\sqrt{z}} \left[\frac{1}{\sqrt{t}} * \text{Im} \left\{ \frac{\sqrt{p}}{\eta} \frac{dp}{dt} \right\} \right] \quad (\text{A.1})$$

and for a delta function source

$$\phi_p(x, z, t) = \frac{\sqrt{2}}{\pi\sqrt{z}} \frac{d}{dt} \left[\frac{1}{\sqrt{t}} * \text{Im} \left\{ \frac{\sqrt{p}}{\eta} \frac{dp}{dt} \right\} \right] \quad (\text{A.2})$$

In these equations, p is given by

$$p = \frac{zt}{R^2} + i\sqrt{t^2 - (R/\alpha)^2} \frac{|z|}{R^2}, \quad (\text{A.3})$$

and η is given by

$$\eta = \frac{|z|}{R^2} t - i\sqrt{t^2 - (R/\alpha)^2} \frac{z}{R^2}. \quad (\text{A.4})$$

The conventions are x positive to the right, u positive to the right, z positive down, but w positive up. The variables are: x , u horizontal distance and displacement; z , w vertical distance and displacement; α p-wave velocity; ϕ potential; and $R = (x^2 + z^2)^{1/2}$.

The method used in this paper requires the delta function response in displacement, which is obtained by taking derivatives of the potential.

$$u_p = \frac{\partial \phi_p}{\partial x} \quad w_p = -\frac{\partial \phi_p}{\partial z} \quad (\text{A.5})$$

To simplify the taking of these derivatives, first take the Laplace transform of Equation A.2.

$$\bar{\phi}_p = \frac{\sqrt{2}}{\sqrt{\pi z}} \frac{s}{\sqrt{s}} \text{Im} \int e^{-s(|x| + \eta|z|)} \frac{\sqrt{p}}{\eta} \frac{dp}{dt} dt \quad (\text{A.6})$$

Now, taking the derivatives A.5 of Equation A.6 and keeping only the far-field terms

$$\bar{u}_p = \frac{\partial \bar{\phi}_p}{\partial z} = (-sp) \bar{\phi}_p, \text{ and } \bar{w}_p = -\frac{\partial \bar{\phi}_p}{\partial z} = (s \eta \epsilon) \bar{\phi}_p, \quad (\text{A.7})$$

where ϵ is the signum function.

$$\epsilon = \text{sgn}(z) = \begin{cases} +1 & z > 0 \\ -1 & z < 0 \end{cases}$$

Returning A.7 to the time domain,

$$u_p = -\frac{d}{dt} \text{Re}(p \phi_p) \text{ and } w_p = \frac{d}{dt} \text{Re}(\eta \epsilon \phi_p). \quad (\text{A.8})$$

Part of Equation A.2 can be evaluated before assembling the displacements, that is

$$\text{Im} \left(\frac{1}{\eta} \frac{dp}{dt} \right) = \frac{H(t-R/\alpha)}{\sqrt{t^2 - (R/\alpha)^2}}. \quad (\text{A.9})$$

A final stipulation is that one derivative with respect to time will be applied later to the source time function before convolving it with the result, so one derivative can be dropped here. Then using A.2 and A.9 in Equation A.8:

$$u_p = \frac{\sqrt{2}}{\pi \sqrt{z}} \frac{d}{dt} \left[\frac{1}{\sqrt{t}} * \left(\frac{H(t-R/\alpha)}{\sqrt{t^2 - (R/\alpha)^2}} \text{Re}(-p \sqrt{p}) \right) \right] \quad (\text{A.10})$$

and

$$w_p = \frac{\sqrt{2}}{\pi \sqrt{z}} \frac{d}{dt} \left[\frac{1}{\sqrt{t}} * \left(\frac{H(t-R/\alpha)}{\sqrt{t^2 - (R/\alpha)^2}} \text{Re}(\eta \epsilon \sqrt{p}) \right) \right] \quad (\text{A.11})$$

Now let

$$u_p = \frac{-1}{\sqrt{z}} \frac{d}{dt} \left[\frac{1}{\sqrt{t}} * u_{FD} \right] \text{ and } w_p = \frac{-1}{\sqrt{z}} \frac{d}{dt} \left[\frac{1}{\sqrt{t}} * w_{FD} \right] \quad (\text{A.12})$$

Then, combining A.10 and A.11,

$$\begin{pmatrix} u \\ w \end{pmatrix}_{FD} = \frac{\sqrt{2}}{\pi} \frac{H(t-R/\alpha)}{\sqrt{t^2 - (R/\alpha)^2}} \text{Re} \begin{pmatrix} p \sqrt{p} \\ -\eta \epsilon \sqrt{p} \end{pmatrix}. \quad (\text{A.13})$$

Approximate \sqrt{p} as

$$\sqrt{p} \sim \frac{\sqrt{p_0}}{2} \left(1 + \frac{p}{p_0} \right)$$

or

$$\sqrt{p} \sim \sqrt{p_0} \left(1 - k + \frac{kp}{p_0} \right) \quad (\text{A.14})$$

where k is a parameter that allows a better fit to \sqrt{p} over selected ranges of take-off angle. Using this approximation, set

$$\begin{aligned} \text{Re}(p \sqrt{p}) &= \text{Re} \left[p \sqrt{p_0} \left(1 - k + \frac{kp}{p_0} \right) \right] \\ &= (1-k) \sqrt{p_0} \frac{zt}{R^2} + \frac{k}{\sqrt{p_0}} \text{Re}(p^2) \\ &= (1-k) \sqrt{p_0} \frac{zt}{R^2} + \frac{k}{\sqrt{p_0}} \left[\frac{t^2}{R^4} (z^2 - z^2) + \frac{z^2}{R^2} \frac{1}{\alpha^2} \right]. \end{aligned} \quad (\text{A.15})$$

Similarly,

$$\text{Re}(\eta \epsilon \sqrt{p}) = (1-k) \sqrt{p_0} \frac{|z|}{R^2} t \epsilon + \frac{k}{\sqrt{p_0}} \frac{t^2}{R^4} \left[2|z|z - |z|z \frac{R^2}{\alpha^2 t^2} \right] \epsilon. \quad (\text{A.16})$$

If i is the take-off angle (the direction of R), measured counter-clockwise from positive z , then $p_0 = \sin(i)/\alpha$. Take $p_0 = 1/\alpha$ for $i \sim \pi/2$ in Equations A.15 and A.16, and apply these to Equation A.13,

$$\left(\frac{u}{w} \right)_{\text{FD}} = \frac{\sqrt{2}}{\pi \sqrt{\alpha}} \frac{H(t-R/\alpha)}{t(1-(R/\alpha t)^2)^{1/2}} \frac{t}{R^2} \left[(1-k) \left(-\frac{z}{|z|} \epsilon \right) + k \frac{\alpha t}{R^2} \left(-2z \frac{z}{|z|} \epsilon + z \frac{z}{|z|} (R/\alpha t)^2 \epsilon \right) \right]$$

Let $(R/\alpha t)^2 = T_\alpha$ and $|z| \epsilon = z$, then

$$\left(\frac{u}{w} \right)_{\text{FD}} = \frac{\sqrt{2}}{\pi R^2 \sqrt{\alpha}} \frac{H(t-R/\alpha)}{(1-T_\alpha)^{1/2}} \left[(1-k) \left(-\frac{z}{|z|} \right) + k \frac{\alpha t}{R^2} \left(\frac{z^2 - z^2 + z^2 T_\alpha}{(T_\alpha - 2) z z} \right) \right] \quad (\text{A.17})$$

It is instructive at this point to do dimensional analysis on Equation A.17. Let units of length be denoted l and units of time t . Then,

$$\begin{aligned} \left(\frac{u}{w} \right)_{\text{FD}} &= \frac{1}{l^2} \frac{\sqrt{t}}{\sqrt{t}} \left[l + \frac{l}{t} \frac{t}{l^2} l^2 \right] \\ &= \frac{1}{l^2} \frac{\sqrt{t}}{\sqrt{t}} l \end{aligned}$$

$$= \frac{\sqrt{t}}{\sqrt{l^3}} \quad (\text{A.18})$$

Convert this result to point source form using Equation A.12.

$$\begin{aligned} (u_w)_p &= \frac{1}{\sqrt{l}} \frac{1}{t} \frac{1}{\sqrt{t}} \frac{\sqrt{t}}{\sqrt{l^3}} t \\ &= \frac{1}{l^2} \end{aligned} \quad (\text{A.19})$$

Now convolve the result with the correct time function, the reduced displacement potential (RDP) function. The definition of the RDP is

$$\phi(R, t) = \frac{-\psi(t)}{R} \quad \text{where } \psi(t) = \psi_\infty(1 - e^{-kt})(1 + kt + \dots) \quad (\text{A.20})$$

where ψ_∞ has dimensions of volume. From Equation A.5, displacement is

$$u = \frac{\partial \phi}{\partial R} = \frac{\psi}{R^2} + \frac{1}{R\alpha} \frac{d\psi}{dt} \quad (\text{A.21})$$

Applying this to the derivation above, true displacement is expressed as

$$u(R, t) = -\psi(t) \frac{d\phi_p}{dR} \quad (\text{A.22})$$

where the derivative is equivalent to the expression of Equation A.19. Continuing with the dimensional analysis, Equations A.19 and A.22 give the result

$$u = l^3 \frac{1}{l^2} t = lt \quad (\text{A.23})$$

But, in the derivation of Equations A.10 and A.11, one time derivative was dropped in order that it could later be applied to the source time function. Replacing ψ with $d\psi/dt$ in equation A.22, Equation A.23 becomes

$$u = \frac{l^3}{t} \frac{1}{l^2} t = l \quad (\text{A.24})$$

which is correct for displacement. Instead of using the RDP, a moment could be applied to the filtered result. Replace $\psi(t)$ with $M_0 10^{-10}/4\pi d \alpha^2$, where M_0 is moment in dyne-cm, d is density in g/cc, and α is p-velocity in km/s for displacement in cm.

When applying this source to the finite difference method, the full form of the source is assembled in stages. The form of the source entered into the finite difference grid is given in Equation A.17. The value of k is chosen at the start of the run to best fit the required range of take-off angles. Of course, since the parameter k governs a linear combination between two source terms, a line isotropic explosion and a line dipole force, the results of two runs differing only in k may be combined to give any desired k . Since Equation A.17 is singular at $T_0=1$, that is $t=R/\alpha$, the corresponding point for the numerical time series must be found by integrating the equation and matching area. This singular nature also introduces energy at frequencies too high for the grid to propagate. To correct this, the numerical time series is convolved with a Gaussian filter before it is propagated.

The finite difference results must be subjected to a line source to point source conversion filter. This filter is given by Equation A.12. It is restated here where U_{line} and U_{point} are line source and point source wavefields.

$$U_{\text{point}} = \frac{1}{\sqrt{x}} \frac{d}{dt} \left[\frac{1}{\sqrt{t}} * U_{\text{line}} \right] \quad (\text{A.25})$$

This may not be the best teleseismic form, considering the approximation (Equation A.14) of \sqrt{p} . Starting with Equation A.2, use Equation A.9 and rearrange terms to obtain

$$\phi_p = \frac{\sqrt{2}}{\sqrt{x}} \text{Re}(\sqrt{p}) \left[\frac{1}{\pi\sqrt{t}} * \frac{\delta(t-R/\alpha)}{\sqrt{t^2-(R/\alpha)^2}} \right]$$

As t approaches R/α ,

$$\begin{aligned} \phi_p &= \frac{\sqrt{2}}{\sqrt{x}} \text{Re}(\sqrt{p}) \frac{1}{\sqrt{2R/\alpha}} \left[\frac{1}{\pi\sqrt{t}} * \frac{1}{\sqrt{t-R/\alpha}} \right] \\ &= \frac{\sqrt{\alpha}}{\sqrt{Rx}} \text{Re}(\sqrt{p}) H(t-R/\alpha) \end{aligned}$$

Use Equation A.14 with $k=0.5$ and the approximations

$$p \sim \frac{\sin i}{\alpha} \quad \text{and} \quad p_0 \sim \frac{\sin i_0}{\alpha}$$

to get the form

$$\phi_P = \frac{1}{2\sqrt{x}R} \left[\sqrt{\sin i_0} + \frac{\sin i}{\sqrt{\sin i}} \right] H(t-R/\alpha)$$

The reference take-off angle i_0 is along positive x , that is, $\sin i_0 = 1$. In this case, the final form is

$$\phi_P = \frac{1}{2\sqrt{x}R} (1 + \sin i) H(t-R/\alpha) \quad (\text{A.26})$$

An ideal line to point filter would cause ϕ_P in Equation A.26 to be $H(t-R/\alpha)/R$ for all angles i between 0° and 180° . A better filter can be found by inspection. Replace \sqrt{x} in Equation A.26 as follows.

$$\phi_P = \frac{1}{2\sqrt{R}} \frac{2}{\sqrt{x} + \sqrt{R}} (1 + \sin i) H(t-R/\alpha) \quad (\text{A.27})$$

Then for both $i=0^\circ$ and $i=90^\circ$ it is immediately found that ϕ_P is $H(t-R/\alpha)/R$. Finally, applying the substitution used to obtain Equation A.27 to the filter given in Equation A.25,

$$U_{\text{point}} = \frac{2}{\sqrt{R} + \sqrt{r}} \frac{1}{\sqrt{t}} \cdot \frac{d}{dt} U_{\text{line}}. \quad (\text{A.28})$$

Figure 1. Schematic diagram displaying energy paths for a) flat layered model versus b) laterally varying structure. The model is two-dimensional. The figure demonstrates the motivation for developing a two-dimensional teleseismic method that accounts for local structural variations.

Figure 2. Teleseismic data at MAT. These are WWSSN short period vertical seismograms recorded at station MAT, Japan for seven different events at various locations within Yucca Flat (see Figure 18). There are very strong secondary phases appearing after P-pP. While P-pP seems relatively consistent among the records, the secondary phases are not, indicating the presence of scattering structure near the source.

Figure 3. Strong motion data for FLASK. Only the vertical velocity records are shown here. The stations (numbered stations ranging from 781 to 795) are each marked as an x on the map of Figure 18. The source is in the center. Such data strongly argue for lateral variation because of the strong lateral contrast in peak amplitude and duration of the Rayleigh wave.

Figure 4. Green's transformation for P not in domain D. The contour Γ is chosen such that there are no singularities of the integrand in the area D that Γ encloses. The variable r in the transformation is the distance from P to any point on Γ or in D. The vector n is the outward directed normal to Γ .

Figure 5. Green's transformation for P in D. Here, the contour σ is introduced in addition to Γ around the point P. Now the domain D' is that area enclosed between contour Γ and contour σ . These contours are freely deformable and σ is chosen to be circular with radius ϵ centered on point P. The limit as ϵ approaches 0 will produce the desired integral formula.

Figure 6. Geometry for three-dimensional analytic evaluation of the Kirchhoff integral. The interface surface is S , with solid angle Ω tracing out dS . The normal to the surface is \hat{n} . The source, at distance r_0 from S , generates potential ϕ which produces signal $\phi(S)$ on the surface. Kirchhoff integration gives the result $\phi(P)$ at point P , at a distance r from S .

Figure 7. Geometry for two-dimensional analytic evaluation of the two-dimensional Kirchhoff integral. The line interface is Γ , with angle θ tracing out dl . The normal to the contour is \hat{n} . The source, at distance r_0 from Γ , generates potential ϕ which produces signal $\phi(\Gamma)$ on the surface. Two-dimensional Kirchhoff integration gives the result $\phi(P)$ at point P , at a distance r from Γ .

Figure 8. The geometry for two-dimensional Kirchhoff along a flat interface in a half space. The contour Γ has been deformed such that it follows a line Γ_1 parallel to the x axis from $x=-\infty$ to $x=+\infty$ and is closed at $r'=\infty$ (Γ_2) in the direction of $z=+\infty$. The integrand becomes trivial along Γ_2 , reducing the integral to an infinite definite integral along x . This is further reduced for numerical application to a finite sum along x .

Figure 9. Test results for Lamb's problem. Three methods are compared in this figure: two-dimensional Kirchhoff, finite differences, and Cagniard-de Hoop. The records are responses in a half space with a source 1 km deep for deeply buried receivers (6 km) at the range of horizontal distances indicated. The velocities of the medium are 4.0 km/s p-wave and 2.3 km/s s-wave with a density of 2.7 gm/cc. The source is an explosion with RDP parameters $K=12.0$, $B=1.0$ and $\psi_\infty=10^{10}$.

Figure 10. Test results for Lamb's problem. The medium is the same as that of Figure 9. The receivers are on the surface and only finite differences and Cagniard are compared. This demonstrates the accuracy

of finite-difference strong motions.

Figure 11. Four models of basin boundaries. These are the four canonical models which are used to demonstrate the effect of various basin terminations. The structure, apart from the boundaries, is a layer over a half space. The layer has a p-velocity 2.3 km/s, s-velocity 1.1 km/s and density 2.0 gm/cc. The half space has a p-velocity 4.6 km/s, s-velocity 2.7 km/s and density 2.7 gm/cc. The star represents the position of the source, always at a depth of 750 m. The inverted triangles are the positions of strong motion instruments. The broken line is the contour along which two-dimensional Kirchhoff is performed. The distances labeled on model 1 are in km.

Figure 12a. Strong motion results for canonical basin models. These seismograms are velocity records at the surface at distances 1, 3, 5 and 7 km from the source, for the first two models shown in Figure 11. An RDP source with $K=12$, $B=1$, and $\psi_{\infty}=10^{10}$ has been used. The number to the right of each trace is the maximum amplitude in cm/s along that trace. Each trace from each model (heavy line) is compared directly to the corresponding trace for flat layers (light line). Two important observations are made. First, the amplitude of the surface wave drops abruptly at the basin boundary, and second, this drop is greatest for the least dipping boundary.

Figure 12b. Strong motion results for basin models. This figure is the same as Figure 12a, but compares the remaining two models shown in Figure 11.

Figure 13. Teleseismic p-wave results for canonical basin models. These seismograms are displacement records convolved with a WWSSN short period instrument response and include the same RDP source used in

Figure 12. They are also convolved with a Q operator with $T^*=1$. They are at a ray length of 1000 km from the source, and at take-off angles 10° , 15° and 20° . The number to the right of each record is the peak amplitude normalized to the peak amplitude of a flat layer model at 0° take off angle. The simple appearance of these seismograms is misleading, they vary significantly from the flat layer response shown as the fifth record in each series. The first four records are from each model, in order, as shown in Figure 11.

Figure 14. Teleseismic p-wave results for basin models. This is identical to Figure 13, except that no Q or instrument response has been convolved with the record. This makes the records broad band. Differences between the records, especially secondary arrivals, are now more obvious.

Figure 15. Teleseismic s-wave results for basin models. The purpose of this figure is to demonstrate the production of teleseismic s-waves, although the true character of teleseismic s-waves observed is not accurately reflected here. The figure is set up the same as Figure 13, but the value of T^* is far too low for the earth for s-waves. The sv arrivals are partly pS, but this phase is small at small take-off angles. Much of the energy shown is the result of basin boundary interactions.

Figure 16. Contributions of various line elements to the final seismogram. The model is model 4 from Figure 11. Case 0 is the result of the contribution from one line element at 17° . Each case adds more line elements to the final seismogram. Cases 0 through 2 progressively build the P-pP arrival; case 3 adds the energy from scattering. The records in all cases are broad band velocity records at 5, 10, 15 and 20 degrees take-off angles. They include an RDP source as described with Figure 12.

Figure 17. Effect of distance. Cases 0 through 3 represent progressively greater distance from the source (5, 10, 100 and 1000 km). These are broad band displacement records at 5, 10, 15 and 20 degrees take-off angle. Cases 3 and 4 are similar because at great distance, thus the source becomes indistinguishable from the scatterer in terms of take-off angle.

Figure 18. Map of Yucca Flat. The contours show the borders of hard rock outcrops. The filled circles are the locations of several events listed adjacent to the figure. Each strong motion station used to record the FLASK event (number 12) is represented by an x. The arc indicates the general shape of the basin boundary as seen from above. The arrow indicates the direction of WWSSN station MAT, Japan.

Figure 19. Cross section of Yucca Flat. The cross section shown here is a generalization of the known structure at Yucca Flat. The three layers from the surface downward are alluvium, volcanic tuff and hard rock. Hard rock is a broad term used here to describe Mesozoic granitic rock and Paleozoic rocks, all of which have similar elastic properties (velocities and density). The stars indicate four different source positions used (numbered 0 to 3), all at a depth of 875 m. The inverted triangles indicate the position of the strong motion records generated by the finite-difference calculations.

Figure 20. Local cylindrical symmetry. The structure of Yucca Flat is shown here as the locally cylindrical result required by the filter used to convert line to point responses. Comparing this to the map of Figure 18, locally cylindrical structure is desirable for the case of Yucca Flat.

Figure 21. Synthetic strong motion records for FLASK. These records, generated by the finite-difference method, include an RDP source with $K=12$, $B=1$ and $\psi_{\infty}=10^{10}$. These are only for source position 1 (of 0 to 3

on Figure 19), and for the stations shown. It is important to see that the peak amplitude drops sharply across the boundary, that the duration of the Rayleigh wave is reduced, and that the Rayleigh wave appears to lose relatively more of the lower frequencies as it crosses the basin boundary.

Figure 22. Direct comparison of strong ground motion. This figure shows some direct observed to synthetic comparisons of strong ground motions for the FLASK event. This demonstrates that, despite the simplicity of the model used, the resulting strong motions are an accurate representation of those observed.

Figure 23. Synthetic teleseismic records for Yucca Flat events. A short period WWSSN response and a Q operator with $T^*=1$ have been convolved into the records. The RDP source mentioned in Figure 21 is also included. The peak amplitudes are normalized to that for a flat layer response at a take-off angle of 0° . The flat layer record shown is at 15° . The important observation here is that moving the source 1 km within the basin is far more important than changing the take-off angle 5° .

Figure 24. Direct comparison of teleseismic records. These comparisons demonstrate the accuracy of the new method. Although the p-waves have passed through the mantle and receiver structure, the majority of the energy in the observed records is explained by the near source structure at Yucca Flat. The repeatability of the method is demonstrated by KEELSON and OSCURO. These events are located close together and are modeled well by the same synthetic record.

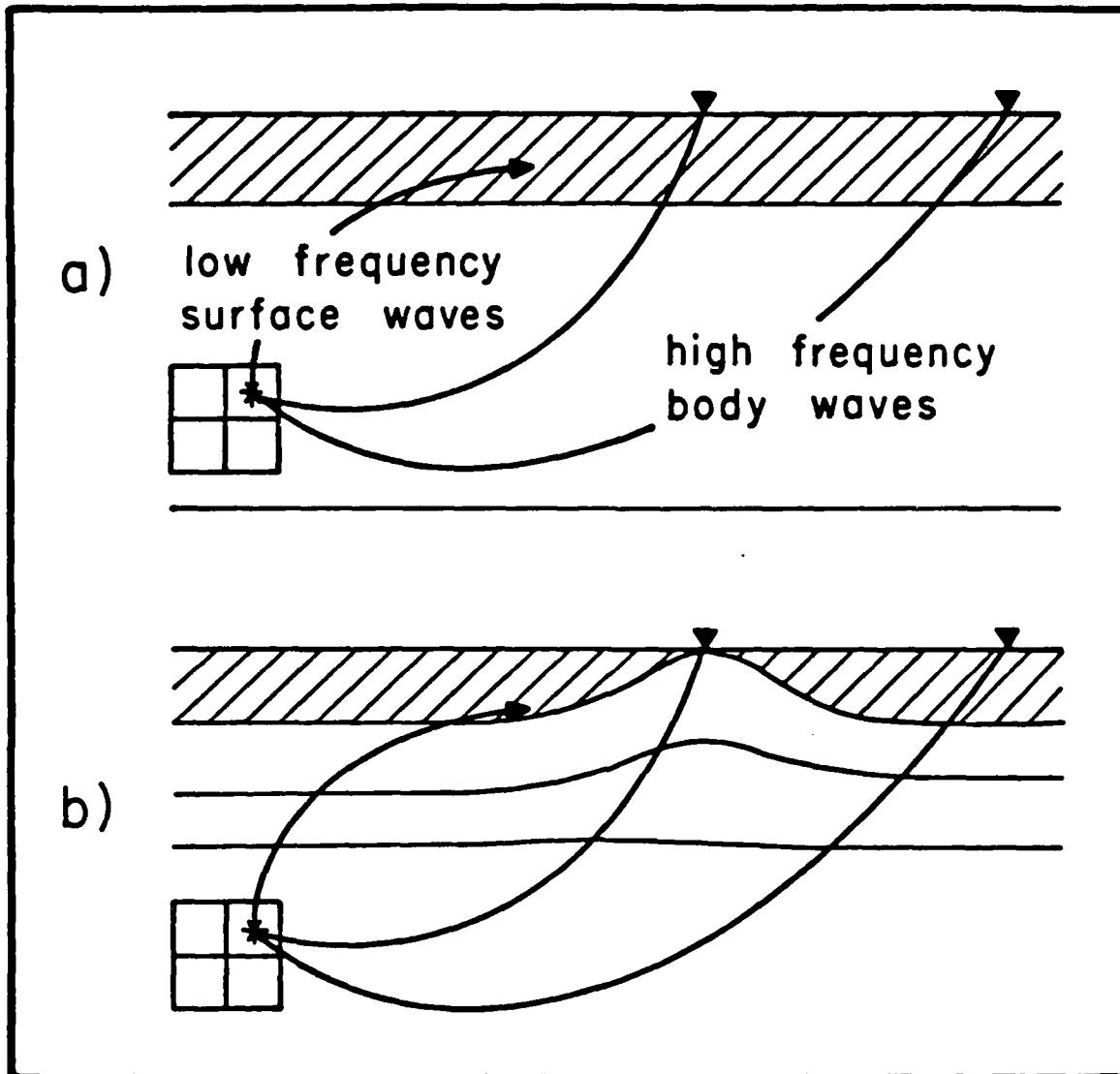


FIGURE 1

MAT

$\alpha z = 308.1^\circ$ $\Delta = 79.5^\circ$ $\alpha = 17.8^\circ$

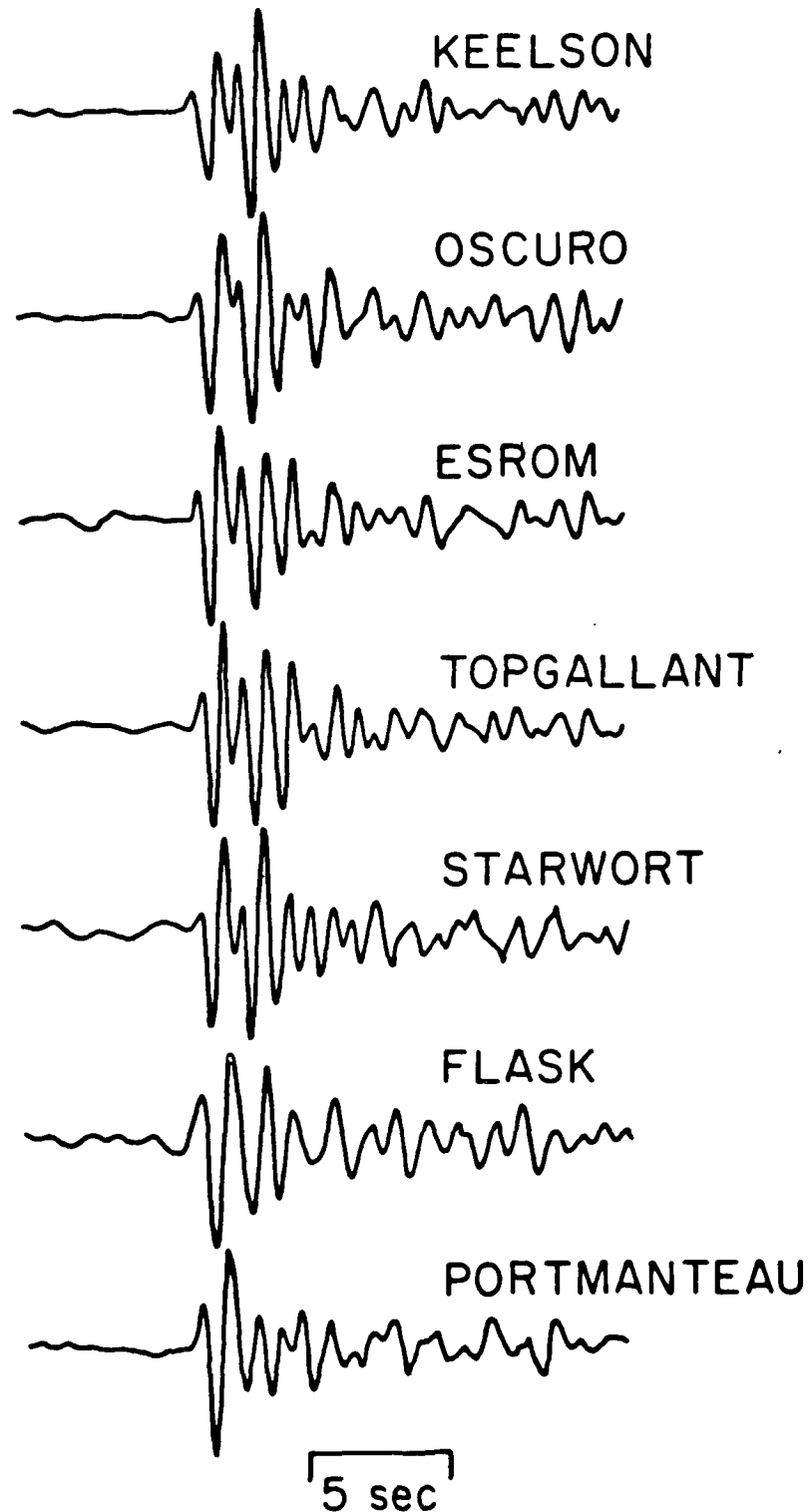


FIGURE 2

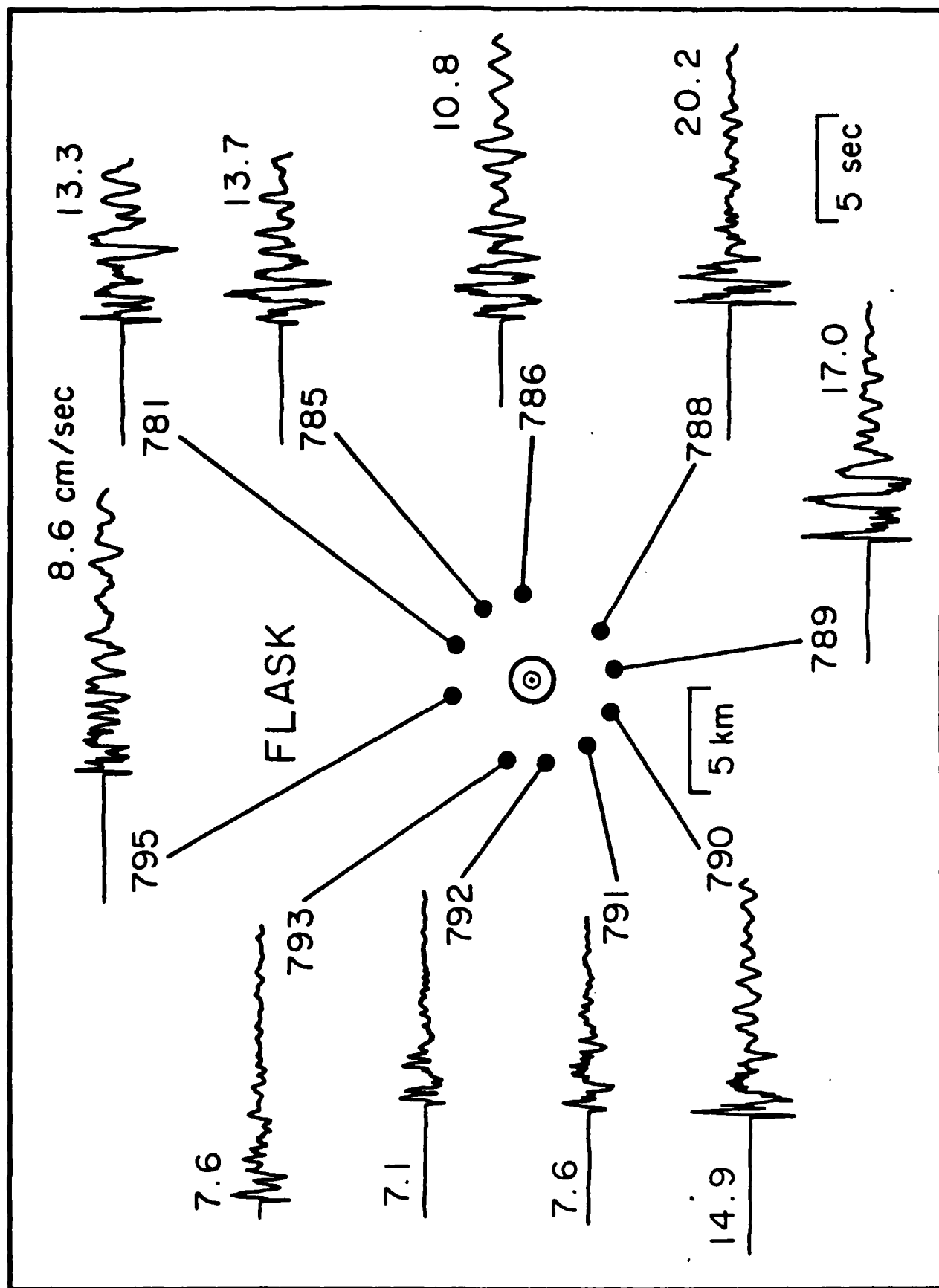


FIGURE 3

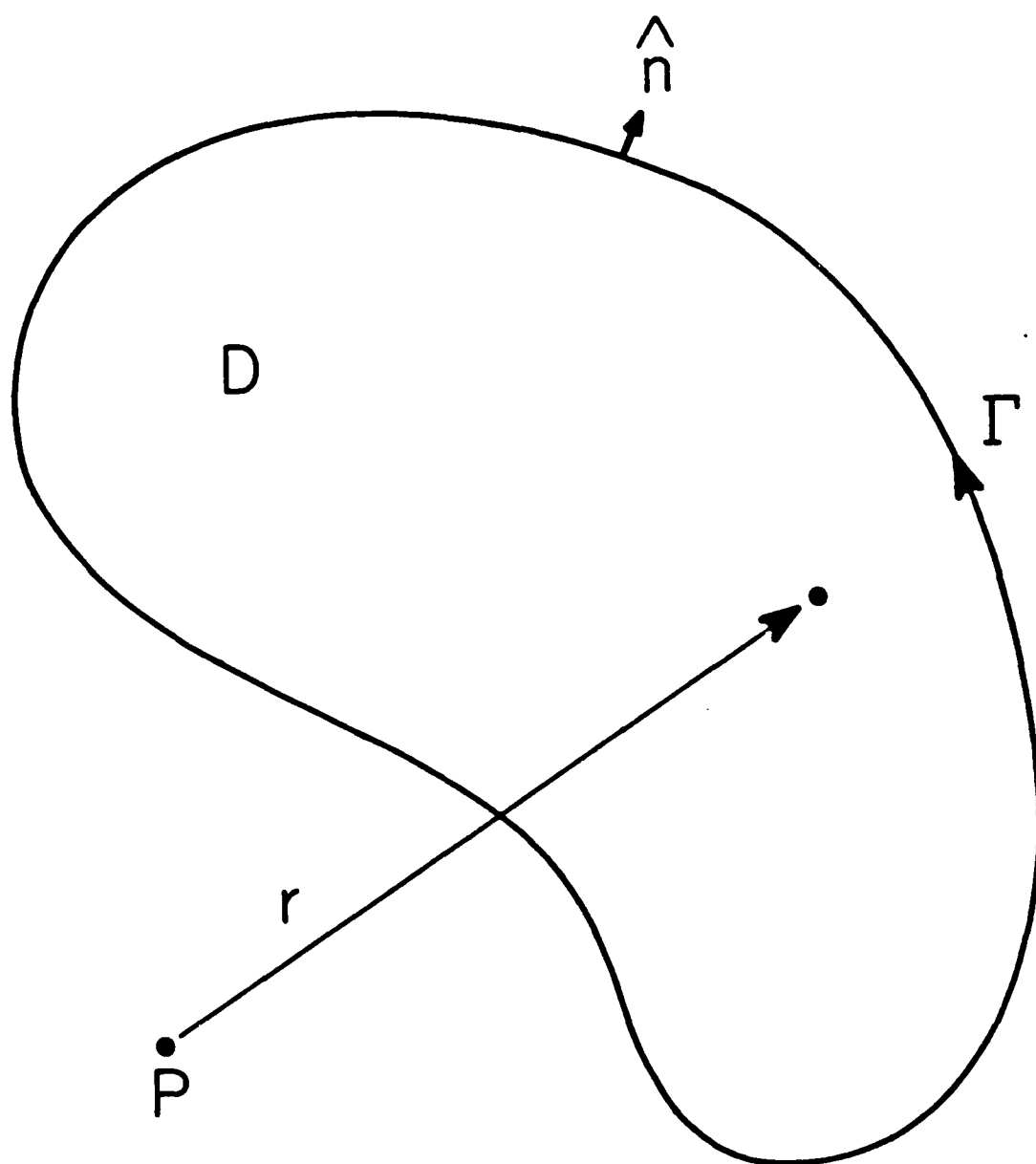


FIGURE 4

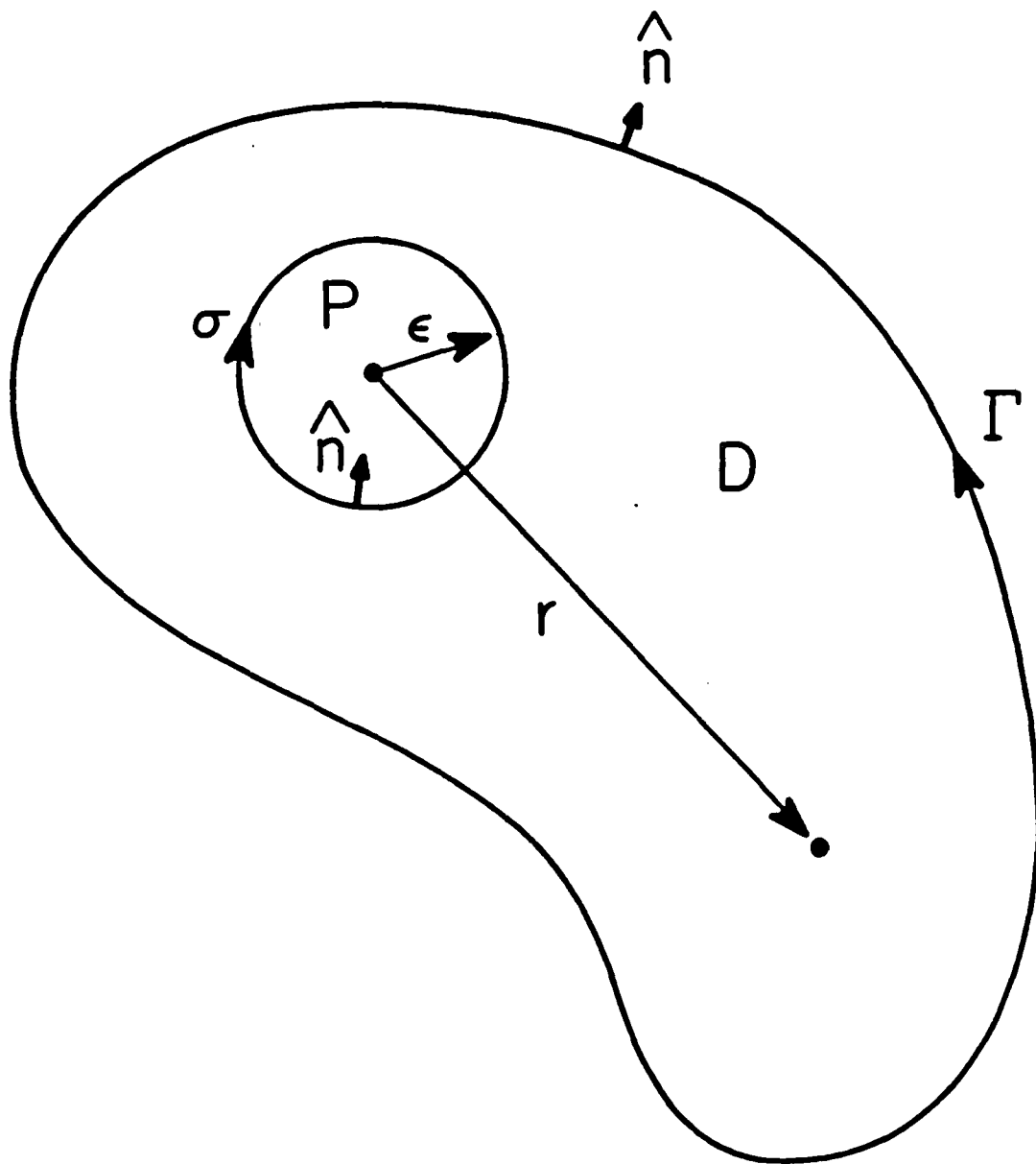


FIGURE 5

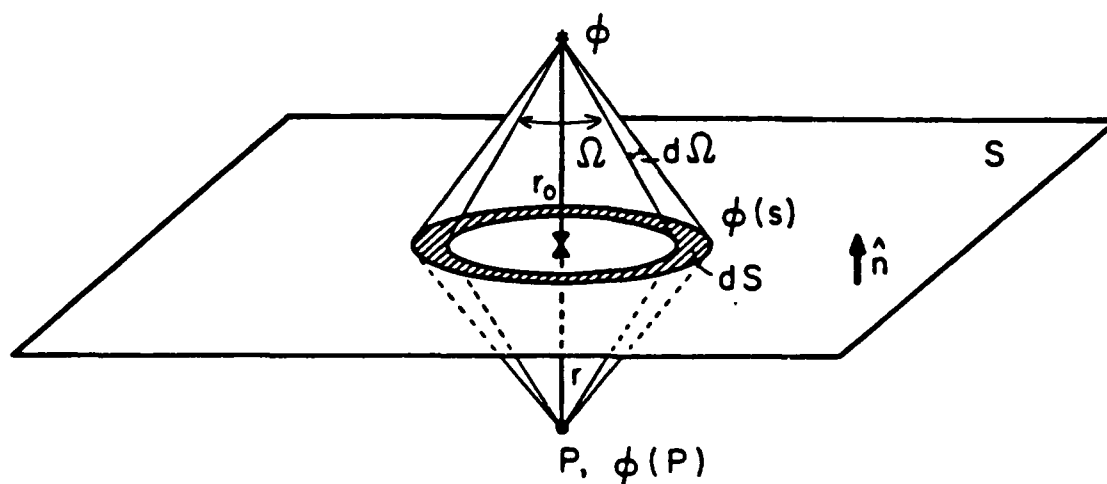


FIGURE 6

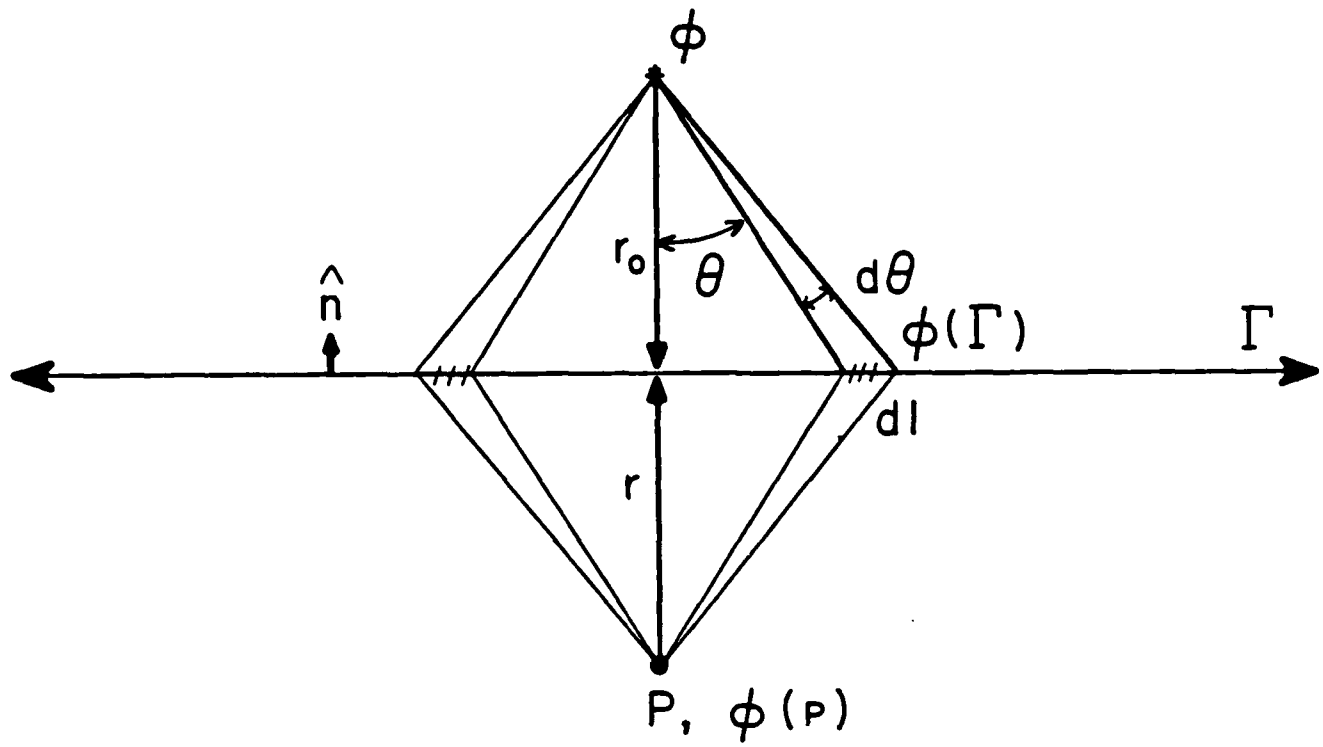


FIGURE 7

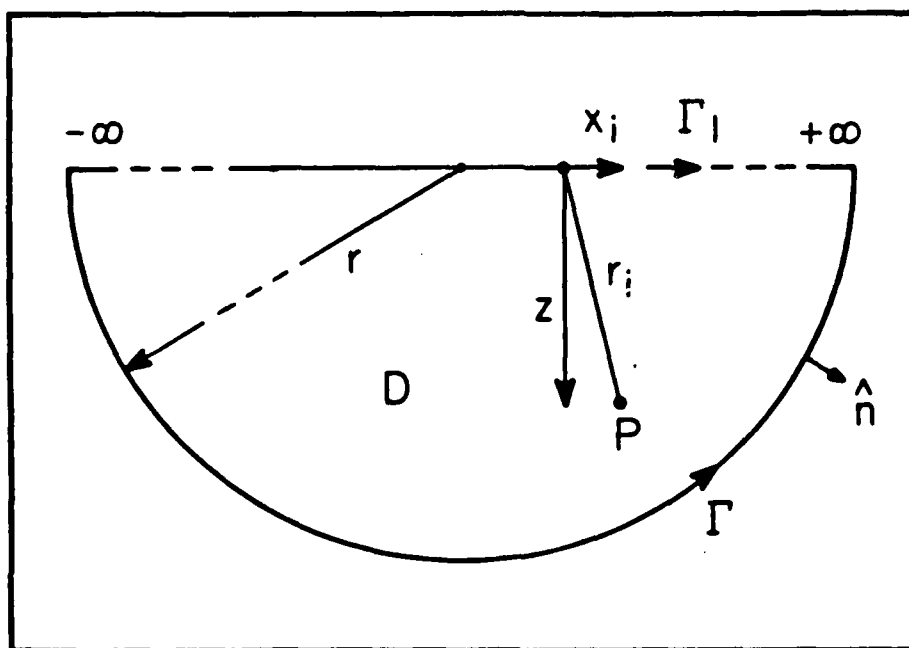


FIGURE 8

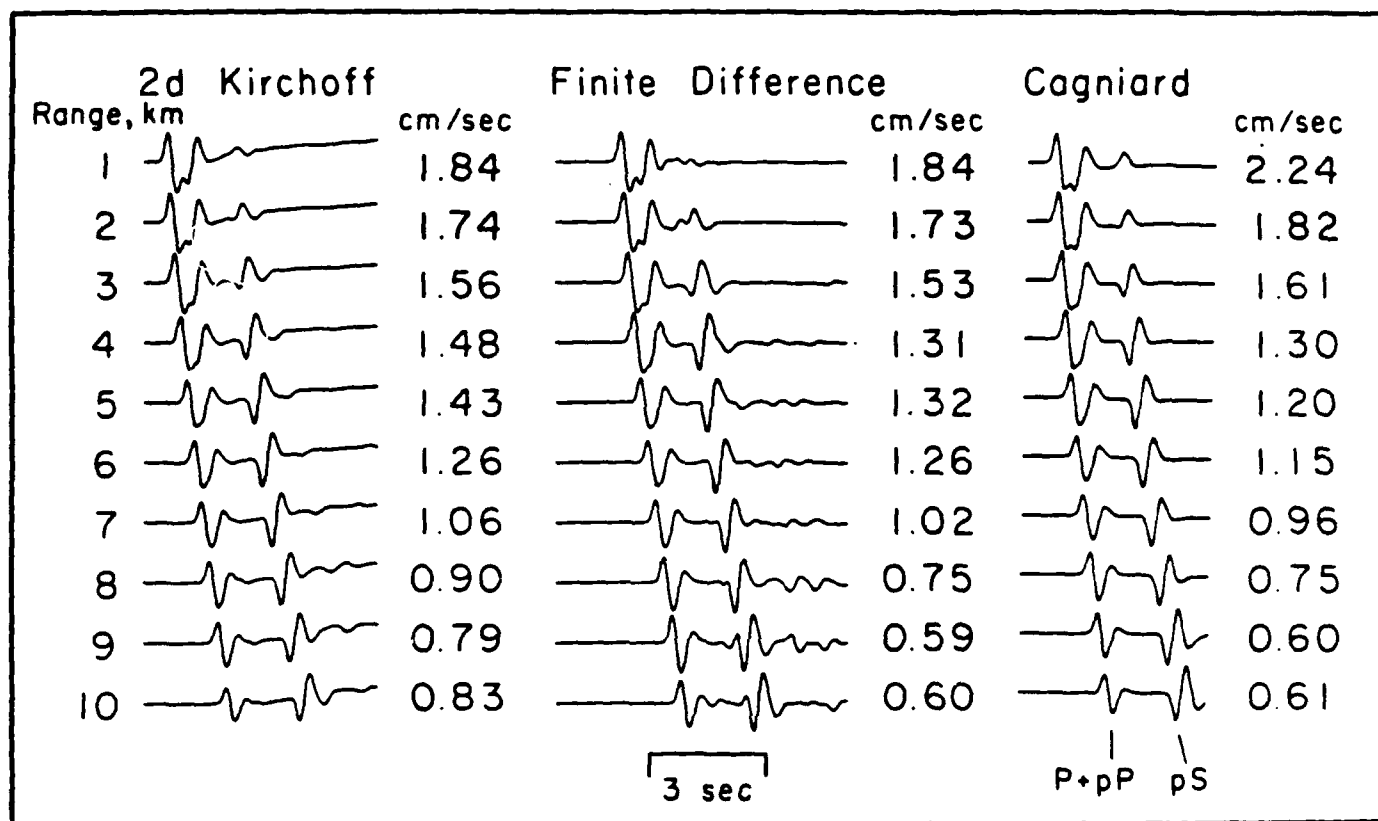


FIGURE 9

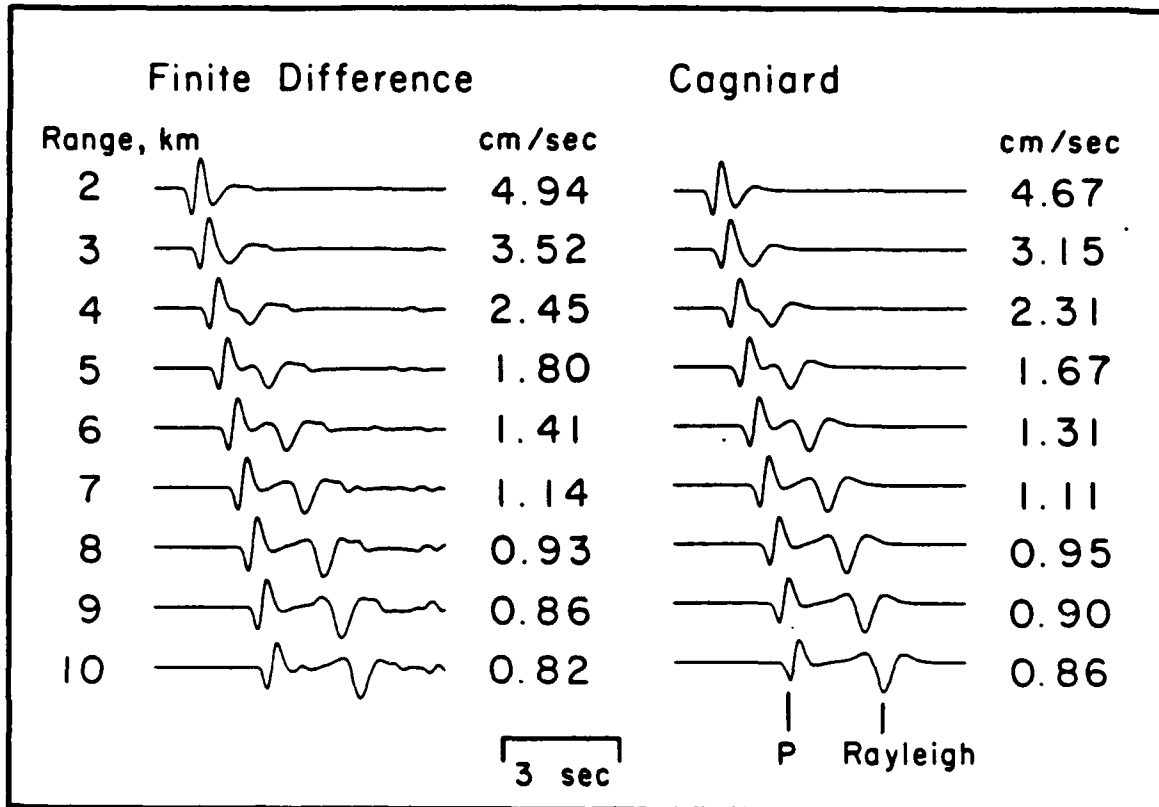
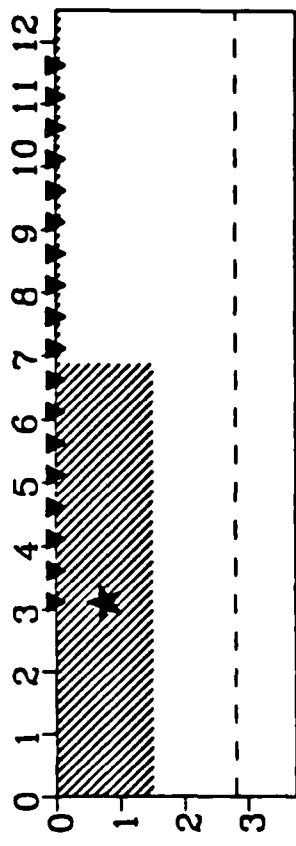
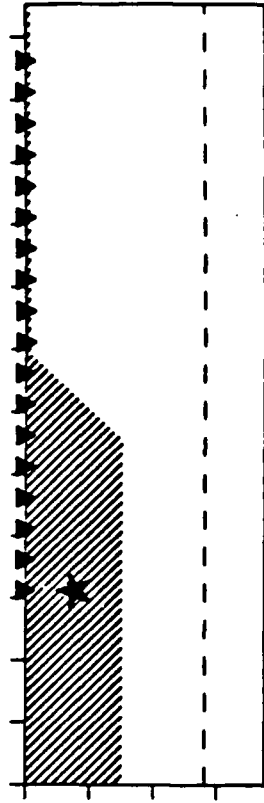


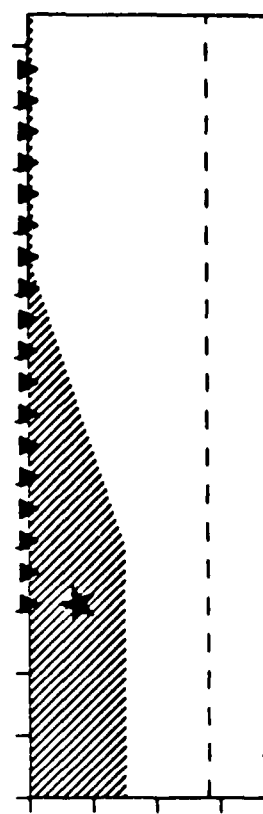
FIGURE 10



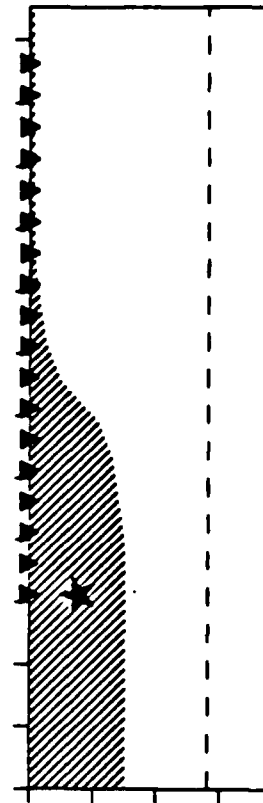
1



2



3



4

FIGURE 11

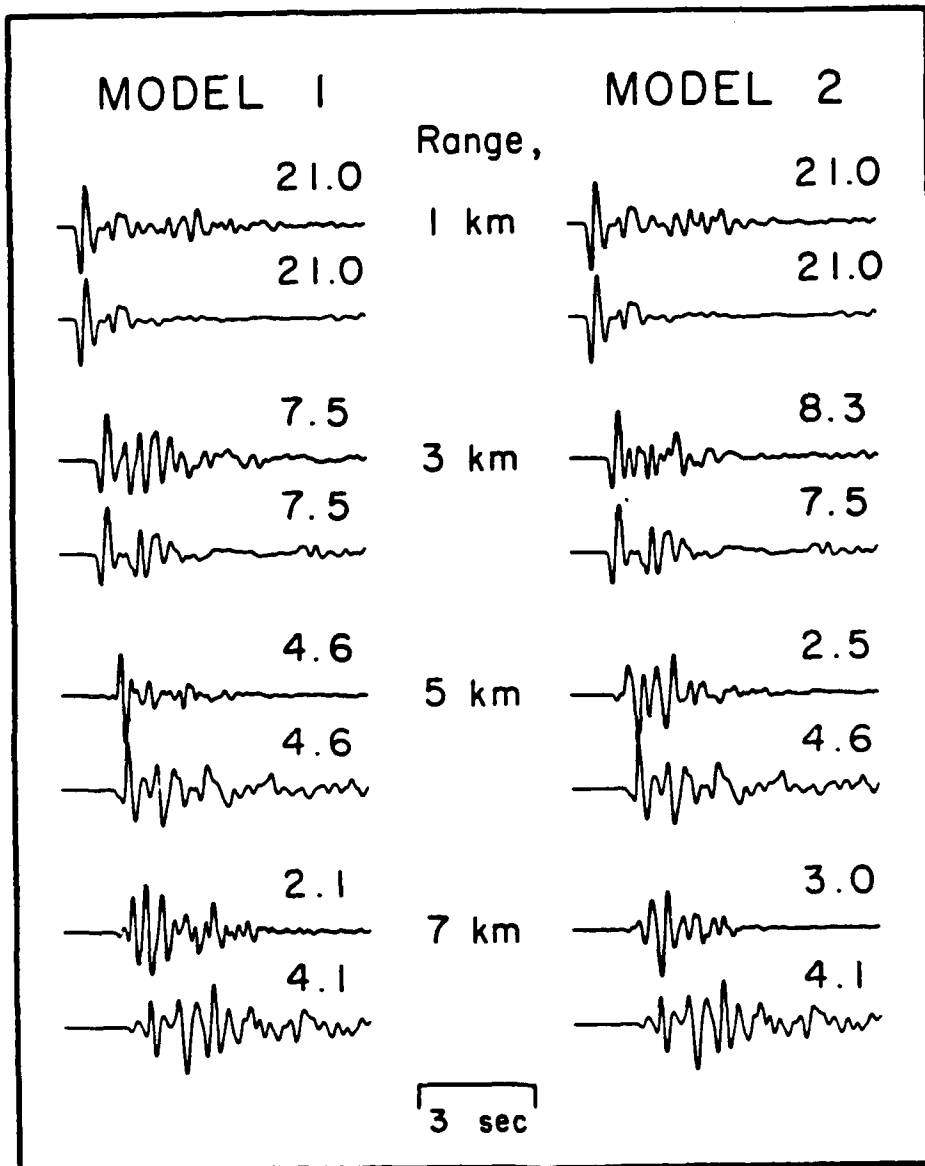


FIGURE 12a

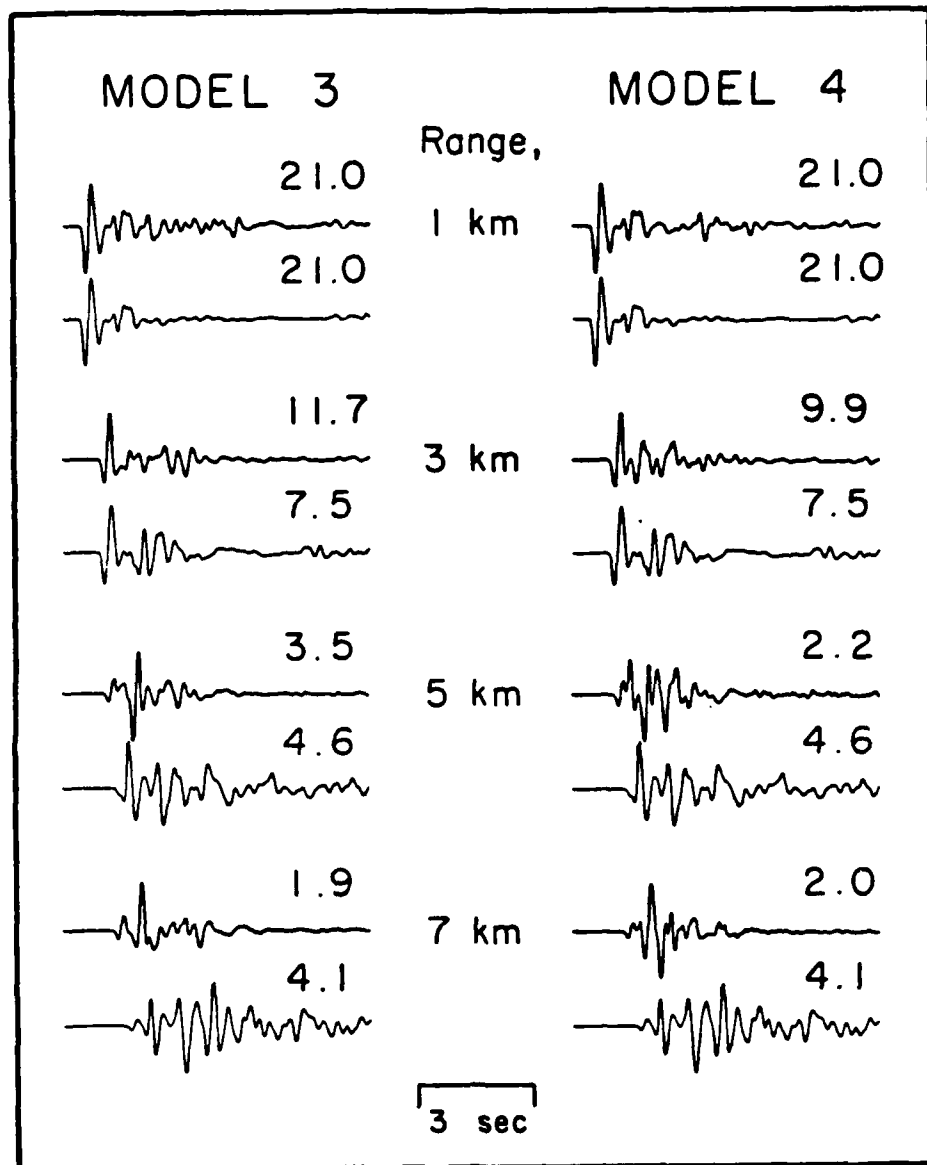


FIGURE 12b

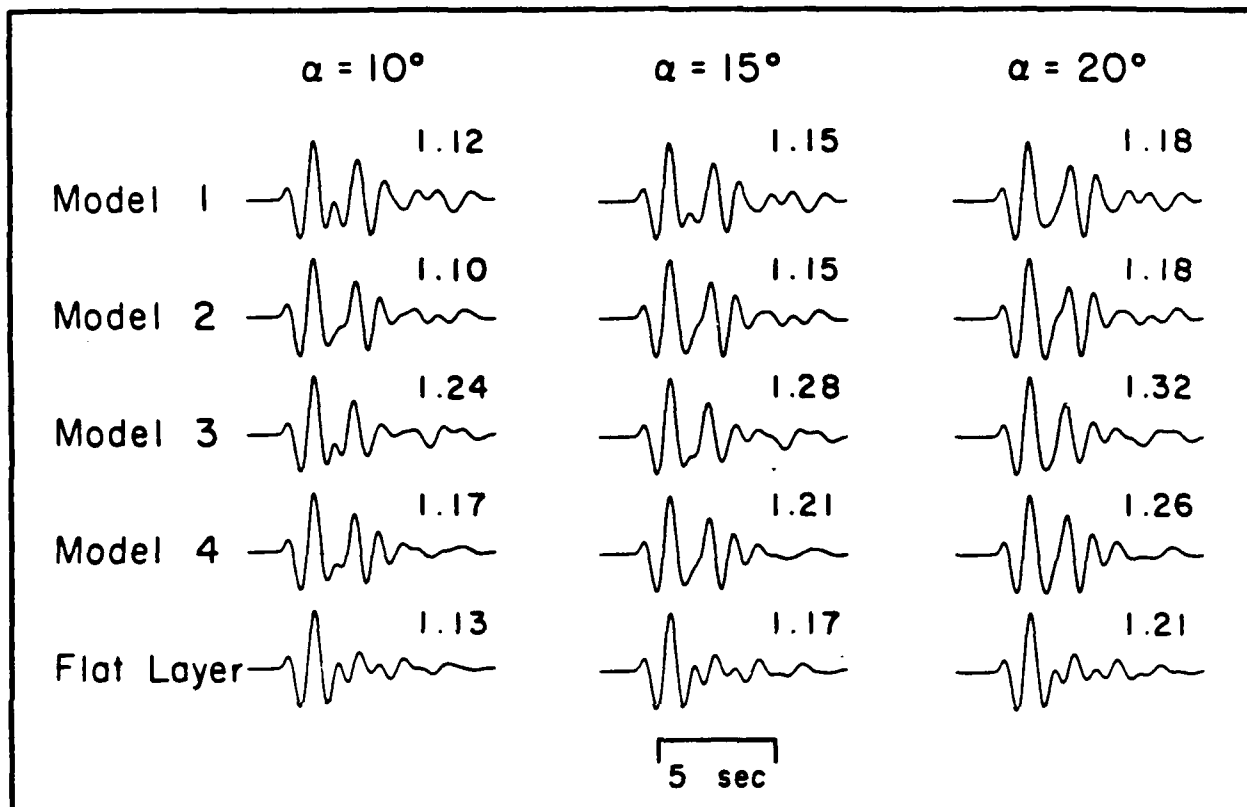


FIGURE 13

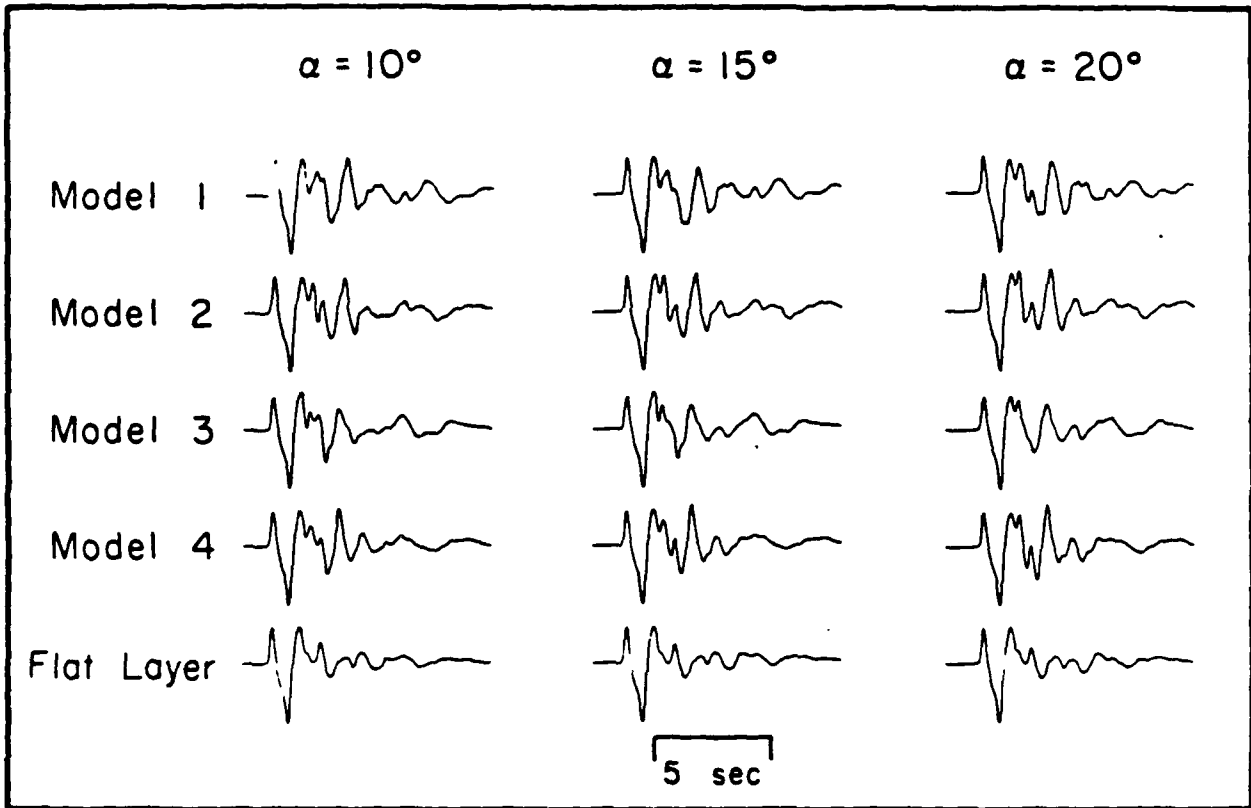


FIGURE 14

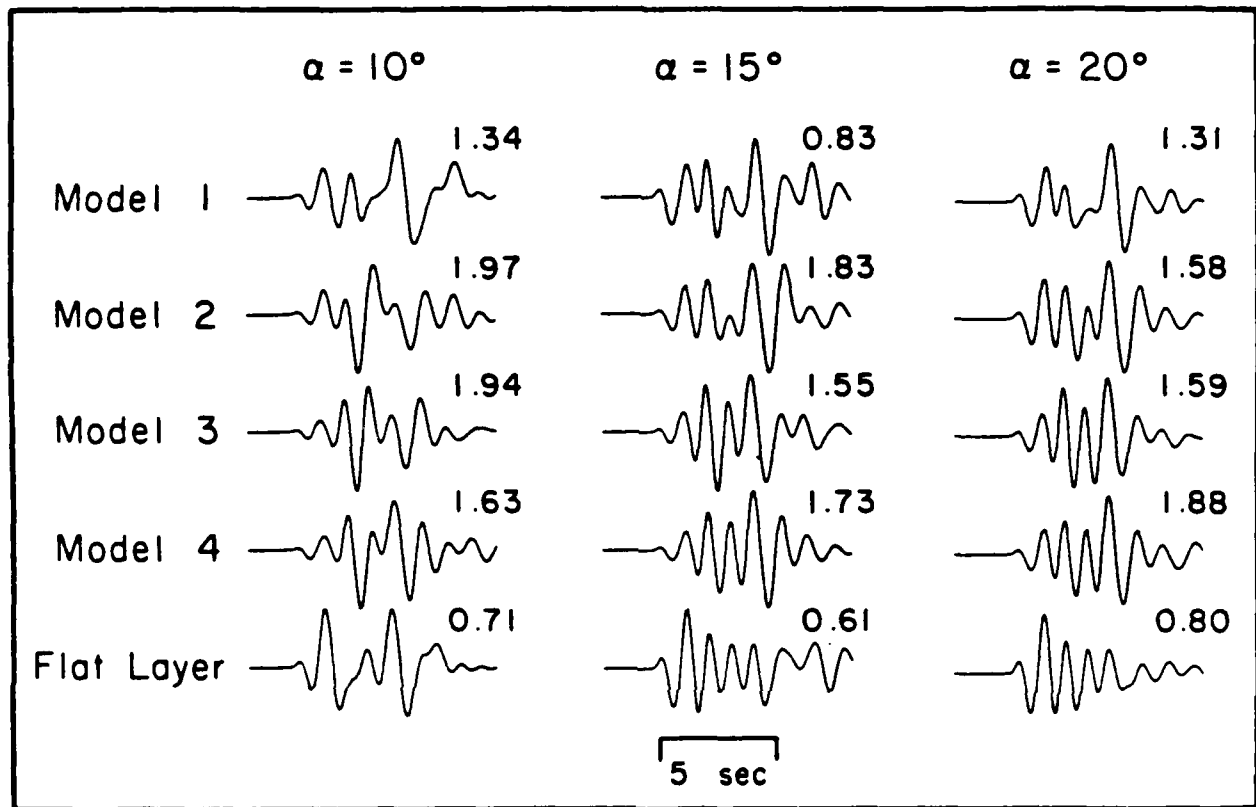


FIGURE 15

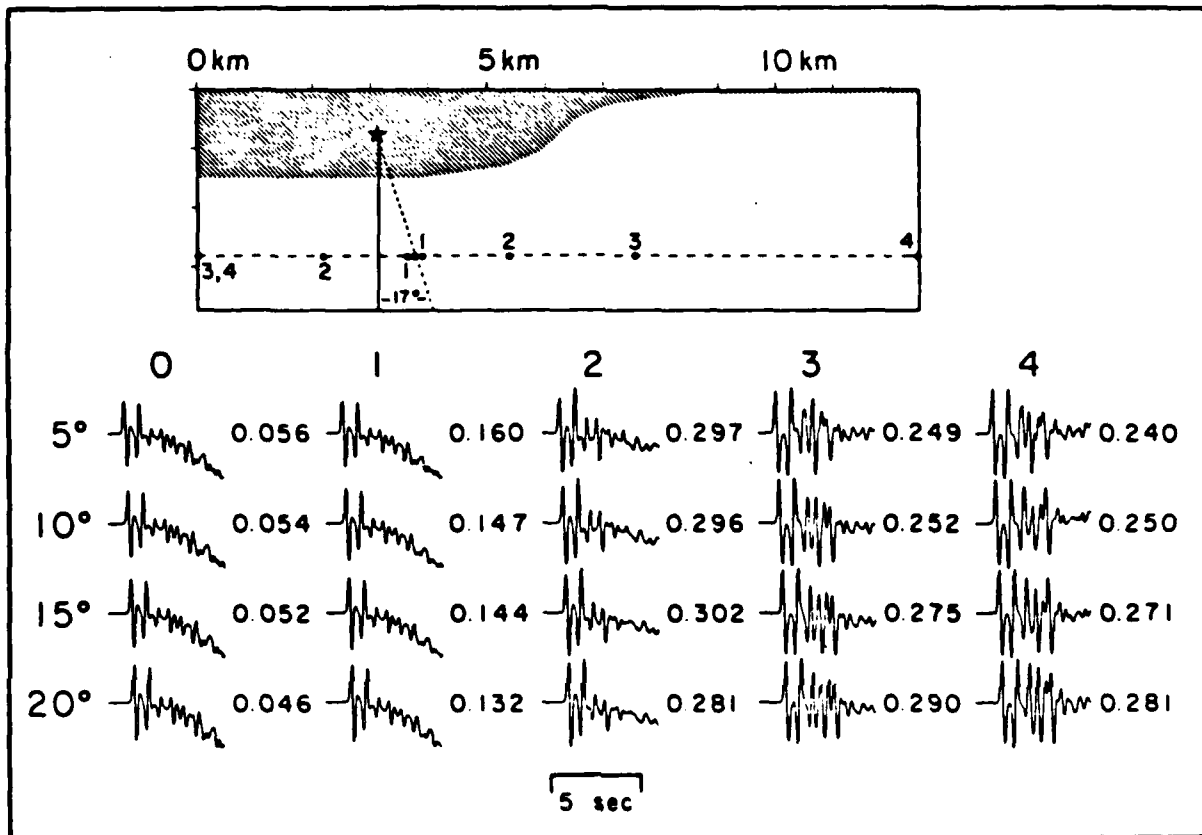


FIGURE 16

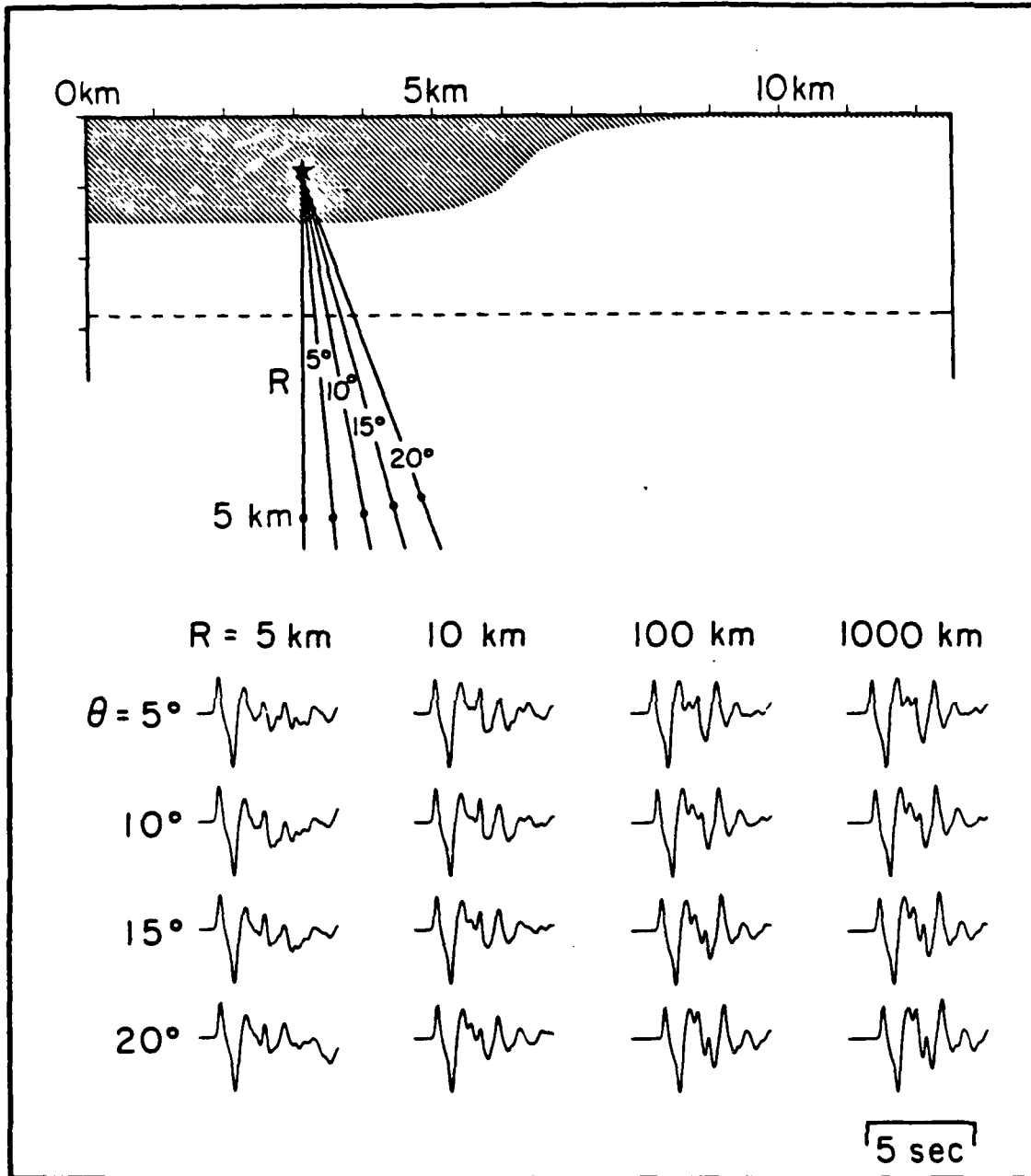


FIGURE 17

Event List

	Event	Date
1	Calabash	10/29/69
2	Carpetbag	12/17/70
3	Chiberta	12/20/75
4	Corduroy	12/3/65
5	Dumont	5/19/66
6	Escabosa	7/10/74
7	Esrom	2/4/76
8	Flask	5/26/70
9	Keelson	2/4/76
10	Knox	2/21/68
11	Lanpher	10/18/67
12	Mizzen	6/3/75
13	Oscuro	9/21/72
14	Portmanteau	8/30/74
15	Starwort	4/26/73
16	Strait	3/17/76
17	Topgallant	2/28/75

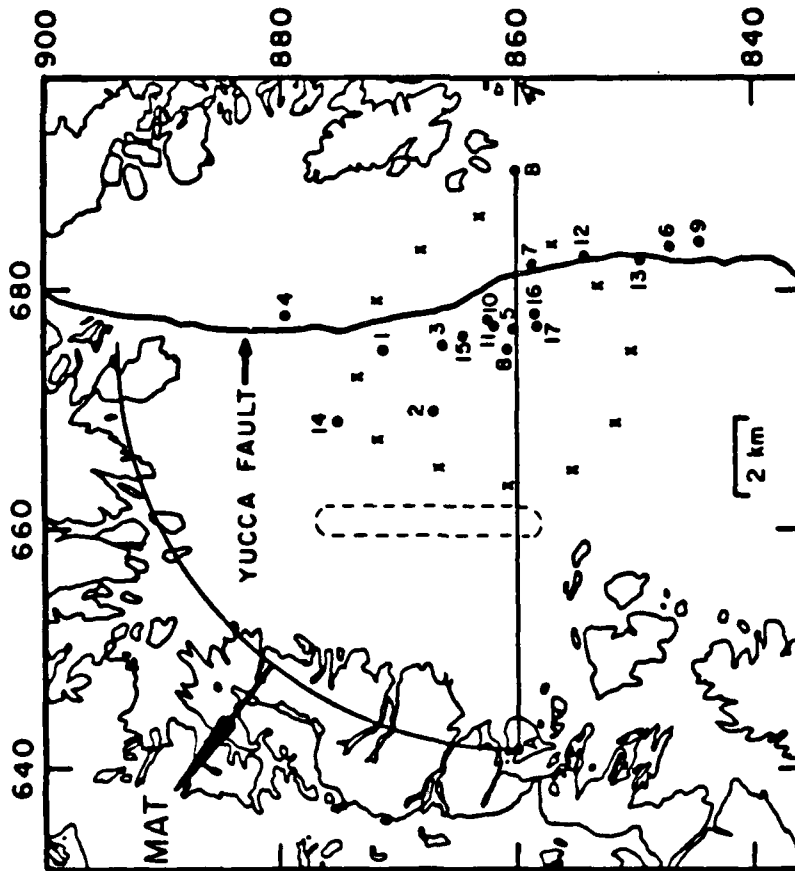


FIGURE 18

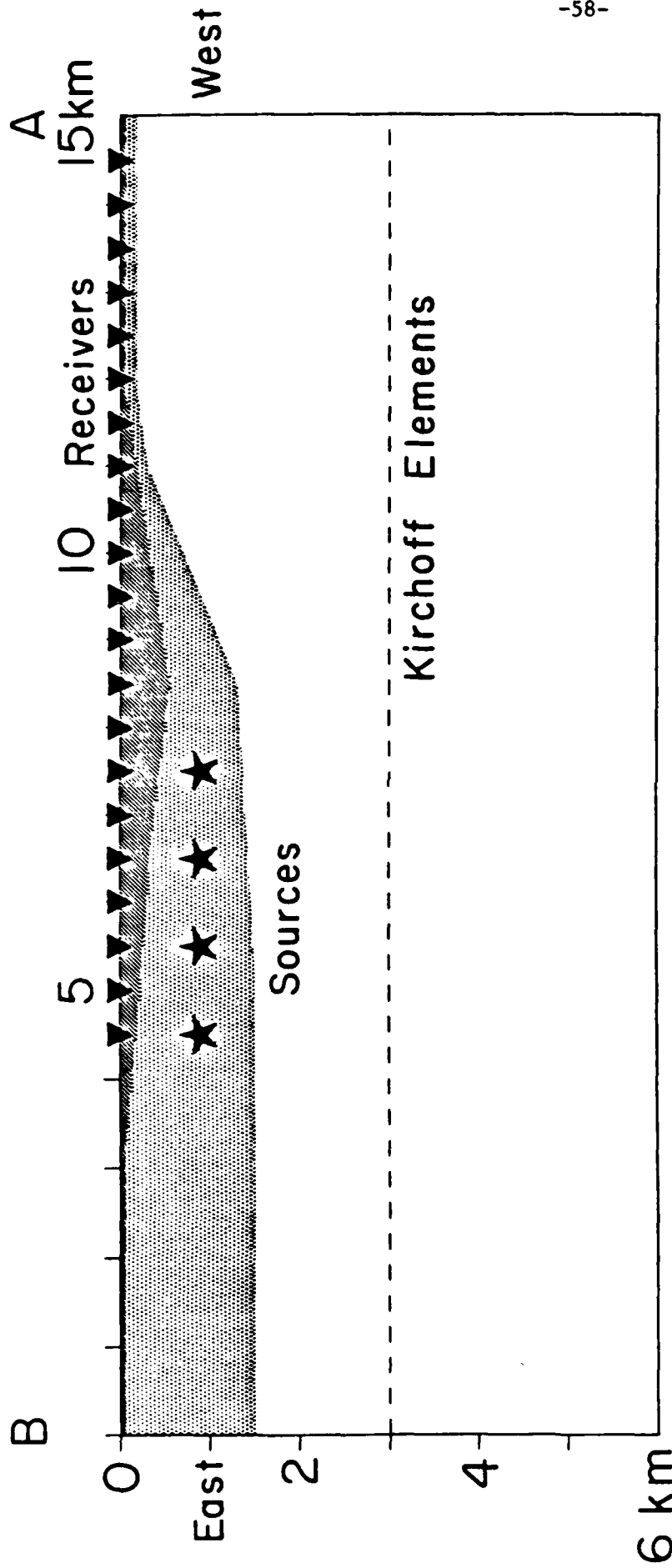


FIGURE 19

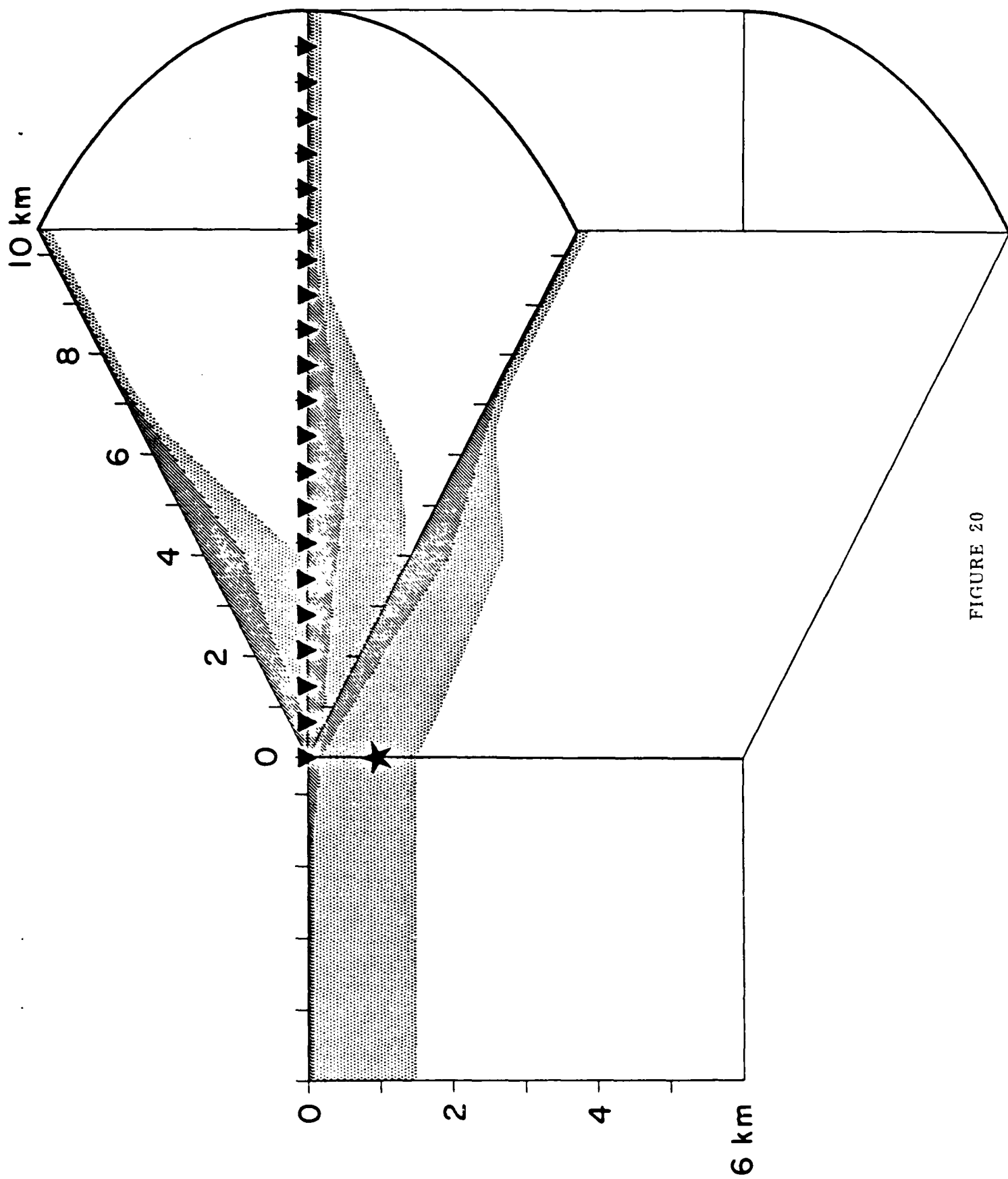


FIGURE 20

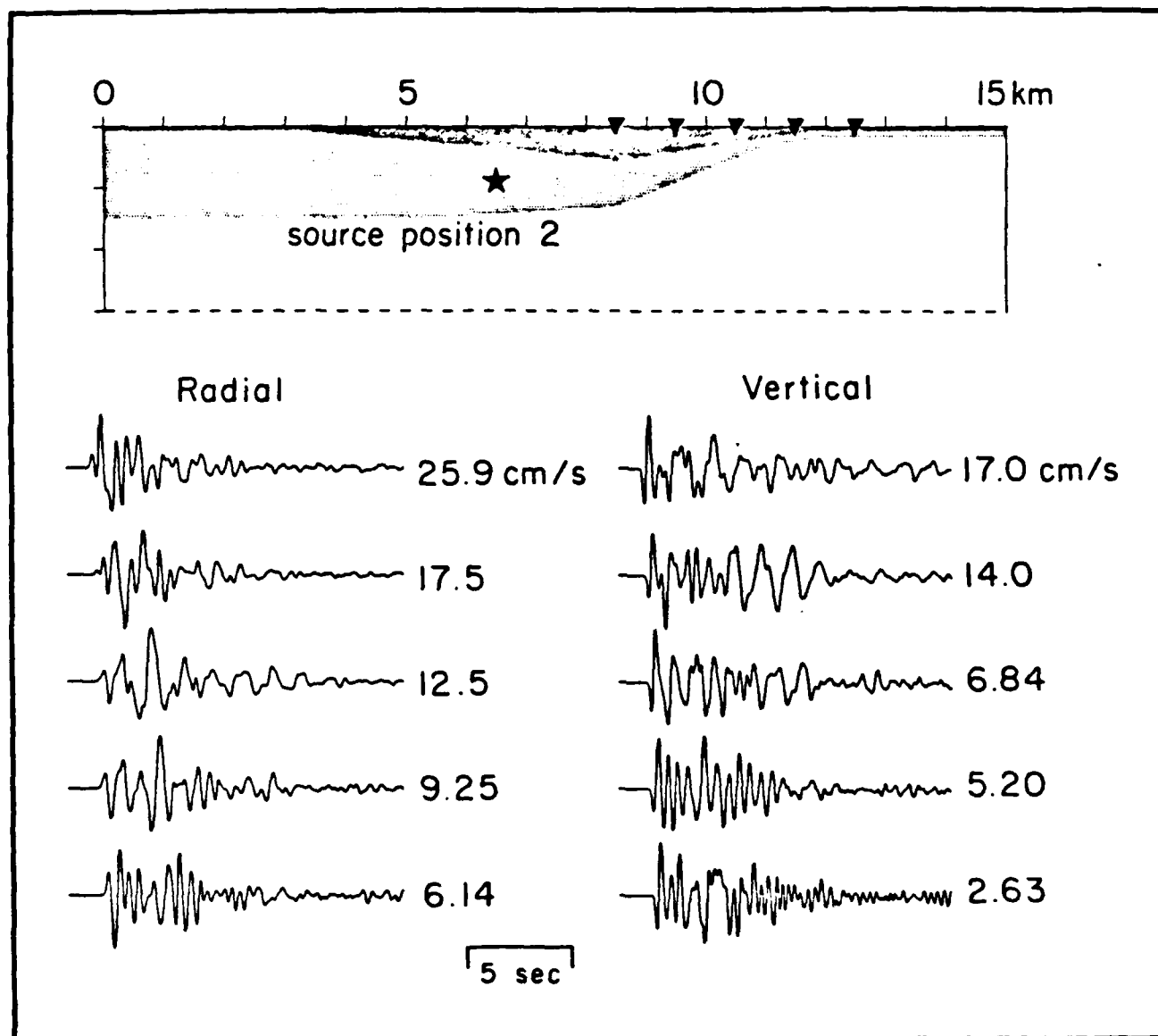


FIGURE 21

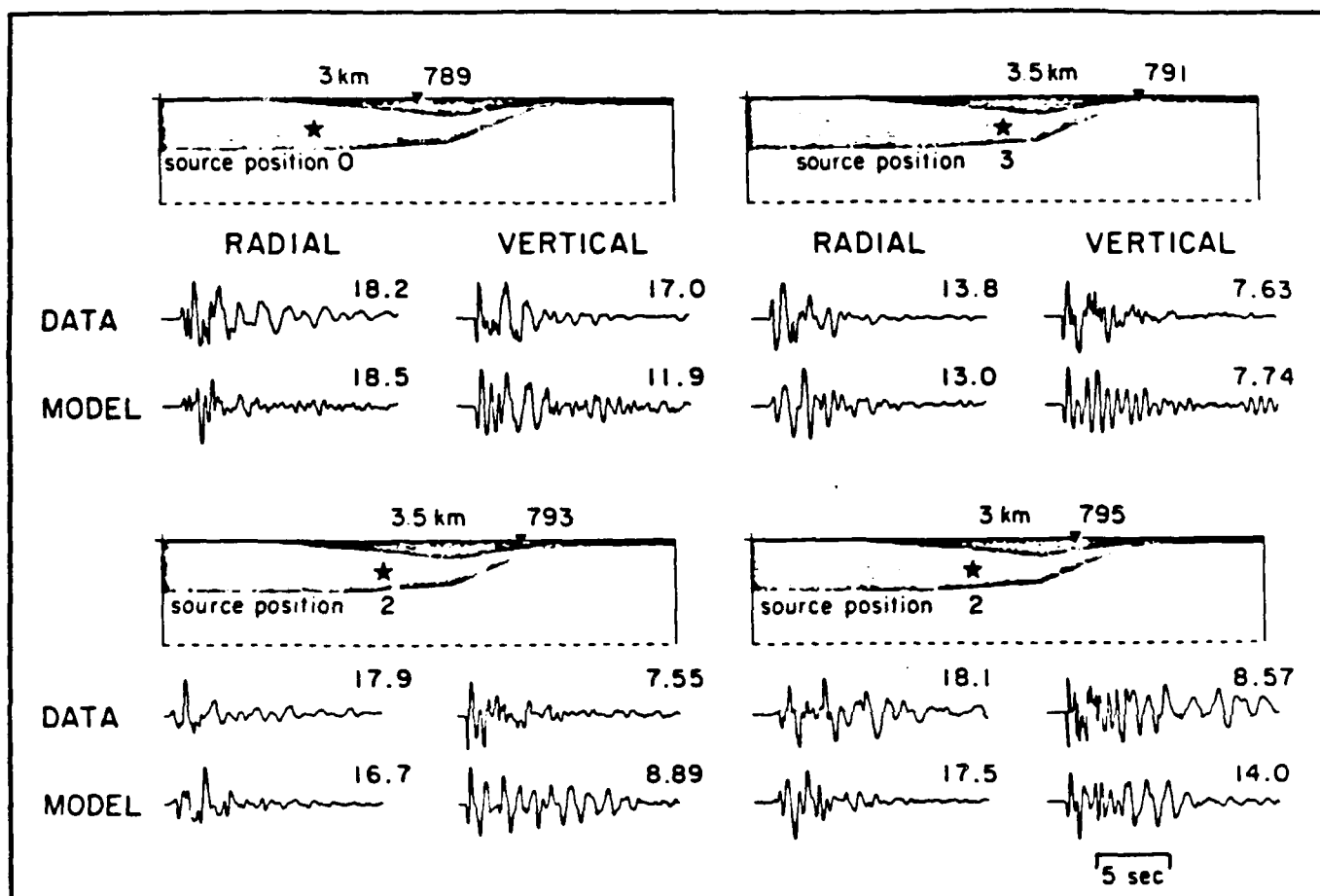


FIGURE 22

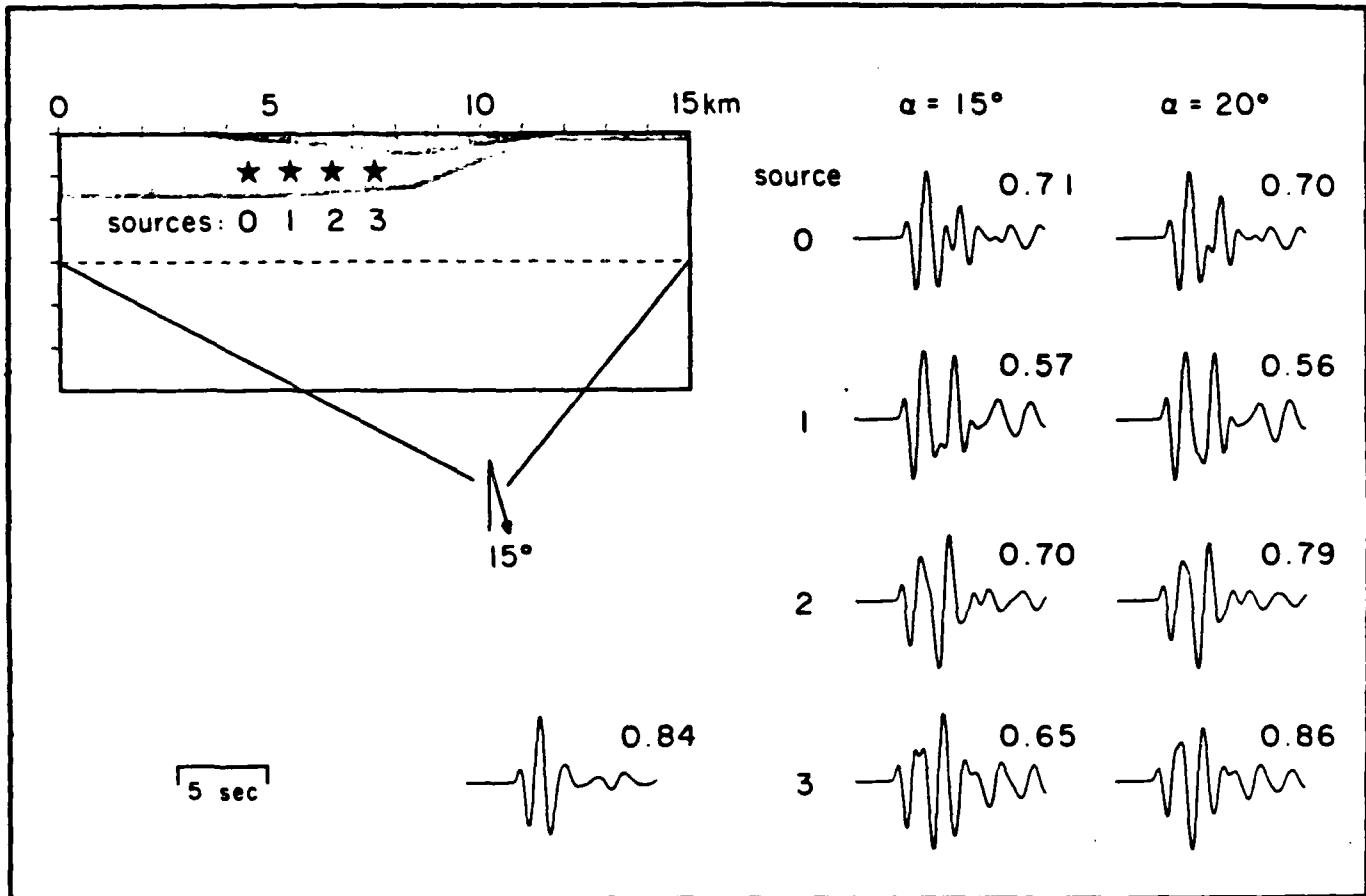


FIGURE 23

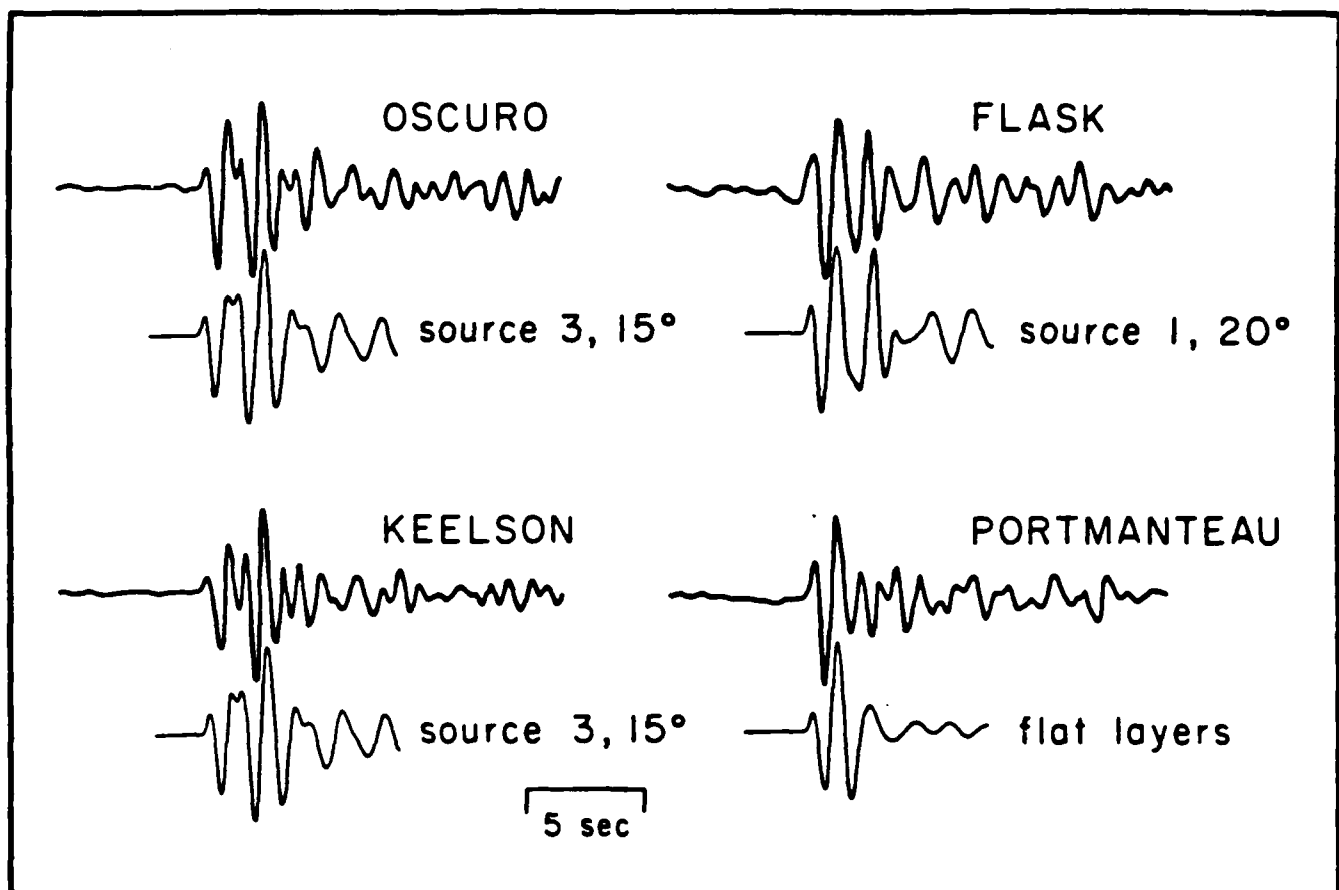


FIGURE 24

Numerical Studies of Propagation of L_g Waves across Ocean Continent Boundaries Using the Representation Theorem

Thesis by
Janice Regan

Table of Contents

Acknowledgements	65
Abstract	66
 Chapter 3: Finite Element to Modal Propagator Matrix Coupling: Tests of Accuracy and applications to transmission of L_g along Partially Oceanic Paths	
1. Introduction	68
2. FE results: effect of oceanic path length on attenuation of L_g	68
3. Calculation of stress components	70
4. RT coupling of Analytic 2-D Seismograms and Green's Functions	88
5. Using the RT Integration Method for Long Oceanic Paths	107
 References	 115

Acknowledgements

Many thanks to my thesis advisor, David G. Harkrider, for guidance, support, and encouragement. Thanks, also to the students, faculty, and staff of the Seismo. Lab. for their friendship and encouragement.

This research has been sponsored by the Defense Advanced Research Projects Agency (DOD) with technical management by the Air Force Geophysics Laboratory under Contract # F19628-85-K-0017.

Abstract

The methods for Representation Theorem (RT) coupling of finite element (FE) or finite difference calculations and Harkrider's (Harkrider 1964, 1970) propagator matrix method calculations to produce a hybrid method for propagation of SH mode sum seismograms across paths that contain regions of non plane-layered structure are explained and developed. The coupling methods explained in detail use a 2-D Cartesian FE formulation. Analogous methods for the 3-D method follow directly. Extensive tests illustrating the validity and accuracy of the implementation of these coupling methods are discussed. These hybrid techniques are developed to study the propagation of surface waves across regional transition zones or other heterogeneities that exist in part of a longer, mostly plane-layered, path. The effects of a thinning or thickening of the crustal layer on the propagation of L_g mode sum seismograms have been examined in this study. The thinning or thickening of the crustal layer is used as a simple model of ocean continent transitions. The L_g phase is of particular interest since it is used in several important applications such as mapping the extent of continental crust, magnitude determination, and discrimination between explosive and earthquake sources. The understanding of the observations that L_g wave is attenuated completely when the propagation path includes an oceanic portion of length greater than one hundred to two hundred kilometers or a region of complex crustal structure is not complete, and a clear explanation of these phenomena could have important consequences for all these types of studies. The transition model calculations done in this study show that passage through a region of thinning crustal thickness, the model for a continent to ocean transition, increases the amplitude and coda length of the L_g wave at the surface, and allows much of the modal energy

trapped in the crust, which forms the L_g phase, to escape into the subcrustal layers as body waves or other downgoing phases. The magnitude of both these effects increases as the length of the transition increases or the slope of the layer boundaries decrease. The passage of the wavefront exiting the continent to ocean transition region through the oceanic structure allows further energy to escape from the crustal layer, and produces a decrease in L_g amplitude at the surface as the length of the oceanic path increases. The amplitude decrease is maximum near the transition region and decreases with distance from it. Passage through a region of thickening crust, the model of a ocean to continent transition, causes a rapid decrease in the L_g amplitude at the surface of the crust. The energy previously trapped in the oceanic crustal layer spreads throughout the thickening crustal layer, and any amplitude which has been traveling through the subcrustal layer but has not reached depths below the base of the continental crust is transmitted back into the continental crust. The attenuation of L_g at the crustal surface along a partially oceanic path occurs in the oceanic structure and in the ocean to continent transition region. The attenuation at the surface depends in part on the escape of energy at depth through the continent to ocean transition region into the underlaying half-space. The total attenuation of L_g due to propagation through a forward transition followed by a reverse transition is at most a factor of four to six. This is inadequate to explain the observed attenuation of L_g . Thus, additional effects, other than geometry must be considered to provide a complete explanation of the attenuation of L_g .

Chapter 3

Finite Element to Modal Propagator Matrix Coupling: Tests of Accuracy and Applications to the Transmission of Lg along Partially Oceanic Paths

Introduction

In this chapter the effects of the length of the intermediate path between the continent ocean and ocean continent transition regions is investigated. First the results of two FE calculations with different intermediate path lengths are presented and compared. These examples are contrasted with the path length used in the previous chapter. Then the RT integration method is discussed and explained. First analytic expressions for the stress components of double couple and line sources are derived, then the expressions for displacement and stress line source Green's functions are determined. These expressions are used to illustrate the validity and determine the accuracy of the RT coupling method. The RT coupling method can be used to continue the propagation of FE results through a layered structure using the displacement and stress Green's functions for the remaining path length and the displacement and stress time histories recorded at a column of element centers within the FE grid.

FE Results: Effect of oceanic path length on the attenuation of Lg

Results of two FE calculations including both forward and reverse transition regions and an intermediate region of oceanic structure are presented here. Many of the details of transmission of wavefield through a forward transition region or a reverse transition region have previously been discussed and will not be repeated here. The vertical extent of the grid and thus that of each time slice illustrated for these calculations is larger than that for the results discussed in the previous chapter. This increase in vertical extent makes the disturbances moving down through the

underlying half-space easier to see. The change in the angle at which these disturbances travel down toward the base of the grid as the width of the triangular regions of maxima widen later in the wavefield is also more clearly visible in these examples.

In Figures 1 to 4 time slices recorded during a calculation using a grid which included fifty kilometer long forward and reverse transition regions separated by an intermediate path, whose length is thirty two kilometers, of oceanic structure. In Figures 5 to 7 the results of a calculation using a grid containing the same fifty kilometer forward and reverse transition regions separated by an intermediate path of seventy nine kilometers are illustrated. Figure 8 shows the RMS amplitude as a function of distance along the surface of each of these models. The upper plot shows the amplitudes for the thirty two kilometer oceanic path and the lower plot shows the amplitudes for the seventy nine kilometer long oceanic path. The amplitude, or vertical scale on each of these plots is identical, however, the horizontal scale, measuring distance along the surface of the crustal layer, is not uniform. The vertical bars on the plots indicate the ends of the regions of oceanic structure. The horizontal scales are uniform between these bars and uniform but different outside these bars. Between these bars the horizontal distance scale is defined so that the total length of the oceanic path in the illustrated model scales exactly to the distance between the bars. The scale outside the area defined by these bars is such that the distance between each point in the regions of equally spaced points is ten nodes.

Examining the time slices for the two examples with different oceanic path lengths shows that the major difference between them appears to be the amount of energy which is escaping out through the bottom of the grid. In the case of the shorter path length only the disturbances traveling through the half-space with the steepest angles are able to pass out of the system. All other disturbances are largely or completely transmitted back into the continental crustal layer since they have not

propagated downwards far enough to avoid being incident of the mantle crust boundary in the reverse transition. This observation provides an explanation of why there is a critical length of intermediate oceanic path beyond which the Lg wave does not travel. As the path length in the oceanic region increases, disturbances traveling through the crust mantle boundary in the forward transition region at progressively shallower angles are able to propagate downwards beyond the base of the continental crustal layer and escape into the mantle. This means that less energy is available to be transmitted back through the mantle crust boundary of the reverse transition and reconverted to Lg wave energy. This trend is seen, although less clearly, in the forward and reverse time slices in chapter 2. The intermediate oceanic path length for that example is one hundred sixty nine kilometers. Disturbances that are seen to propagate out of the grid in that long path example can be traced, even in the example with the longer path length presented here, across the oceanic path length back into the crust through the reverse transition region. This implies that as the path length increases more and more converted energy is able to leave the system.

There is another contribution of the oceanic path length to the attenuation of Lg passing through an oceanic structure. The energy that is transmitted into the oceanic crustal layer is not all in the form of modes compatible with trapped modes in the oceanic crust. Therefore, as the wavefront propagates through the oceanic structure further energy leaks from the crustal layer and propagates downward to eventually escape from the system.

Calculation of Stress Components

To test the RT algorithm for coupling FE results to propagator calculations it is first necessary to determine expressions for the stress seismograms and the stress and displacement Green's functions used in the convolution integral. These expressions are developed and demonstrated in this section. The use of these expressions in the RT

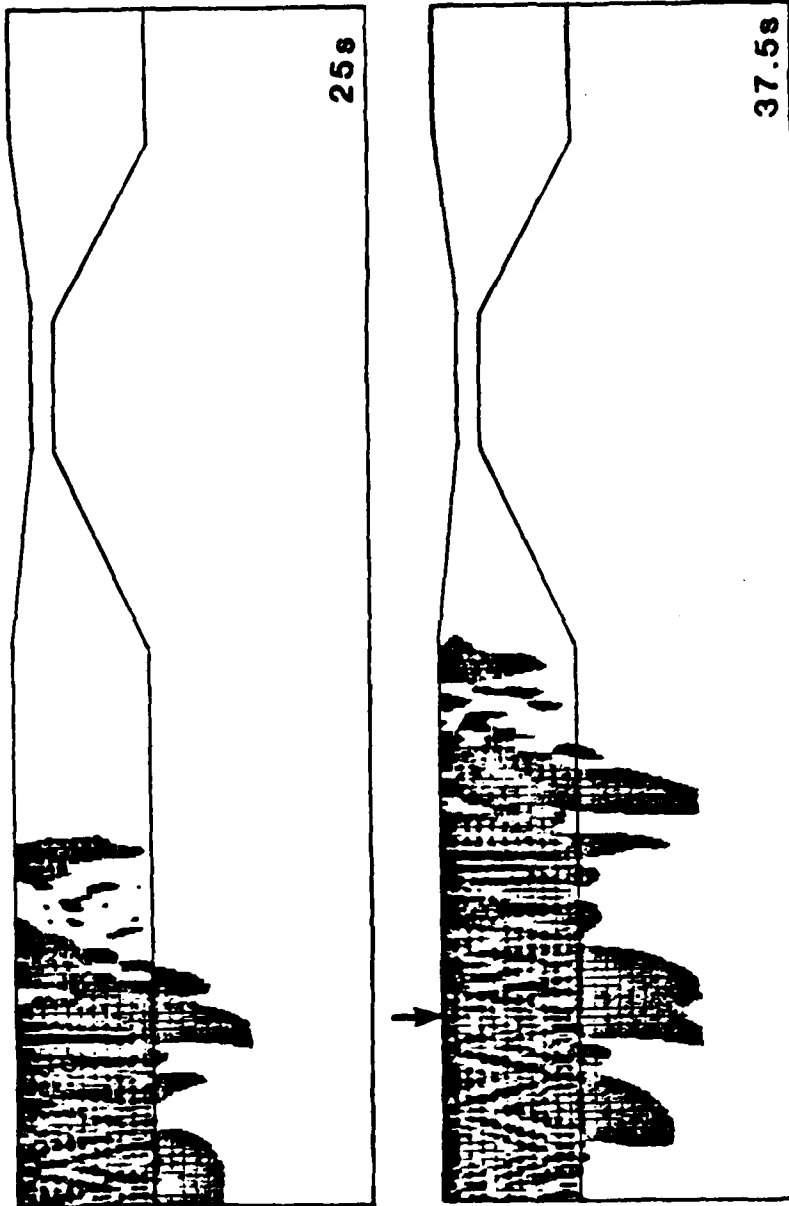


Figure 1: Time slices recorded during the calculation using an intermediate oceanic path length of 32 kilometers. The crustal layer and the ends and bottom of the FE grid which contain it and the underlying half-space are outlined. Within the outlines the displacements at each grid point at the indicated instant of time are plotted. A larger displacement produces a correspondingly larger point on the plot. Thus, high displacement areas appear darker. Each time slice is scaled so its maximum amplitude appears identical on the plot. The time since the initiation of the FE calculation is shown below the right end of each grid. The arrow above a time slice shows the location to which the disturbances, moving at 3.5 km/s, seen at the left end of the previous time slice, have moved in the intervening time.

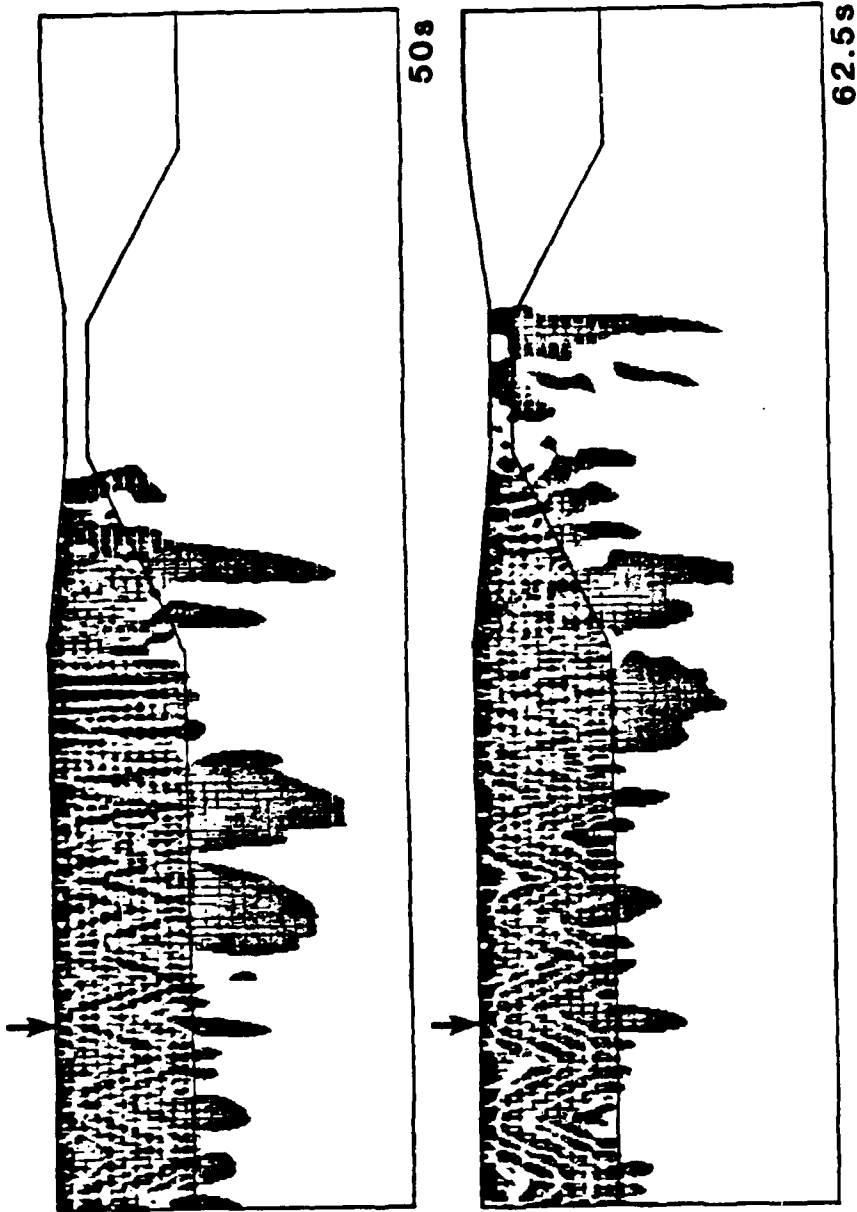


Figure 2: Time slices recorded during the calculation using an intermediate oceanic path length of 32 kilometers. Time slices for two later times illustrating the further propagation of the wavefield through the model. Details are the same as for Figure 1.

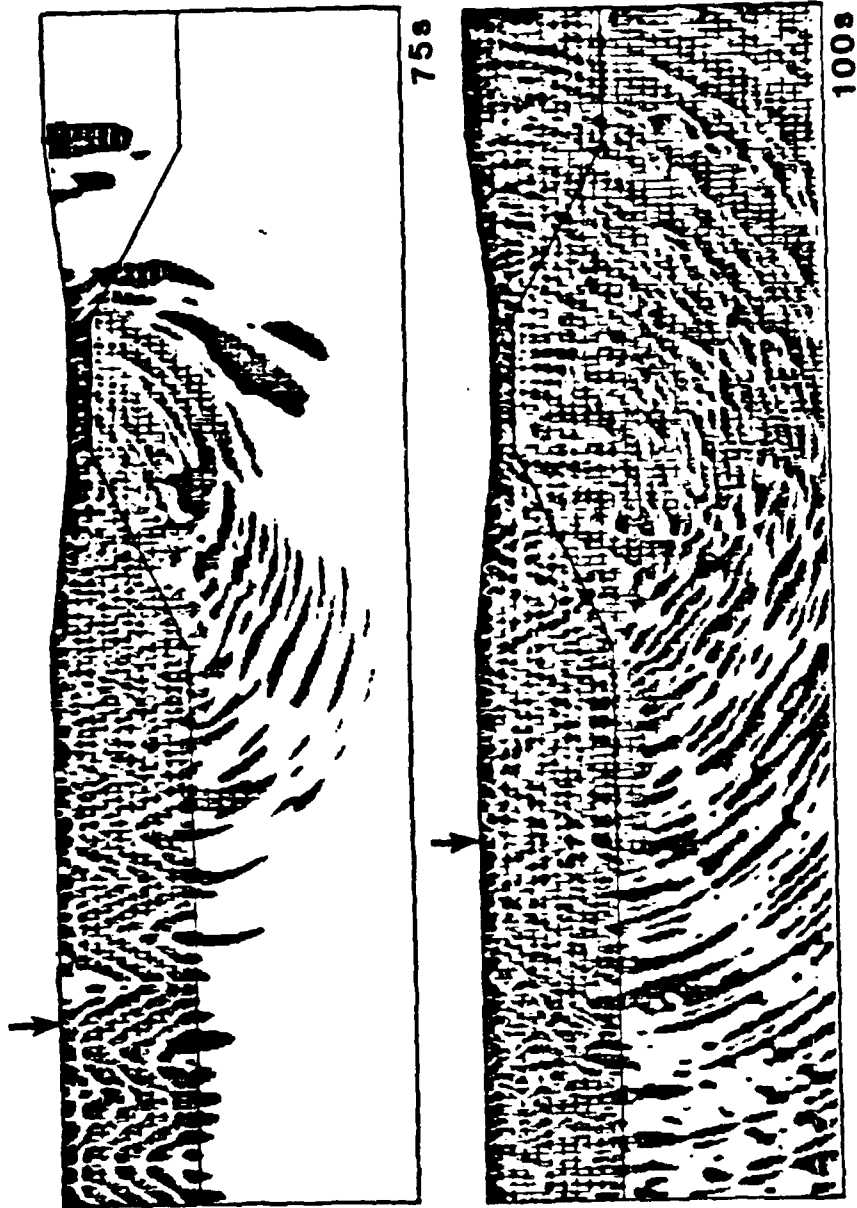


Figure 3: Time slices recorded during the calculation using an intermediate oceanic path length of 32 kilometers. Time slices for two later times illustrating the further propagation of the wavefield through the model. Details are the same as for Figure 1.

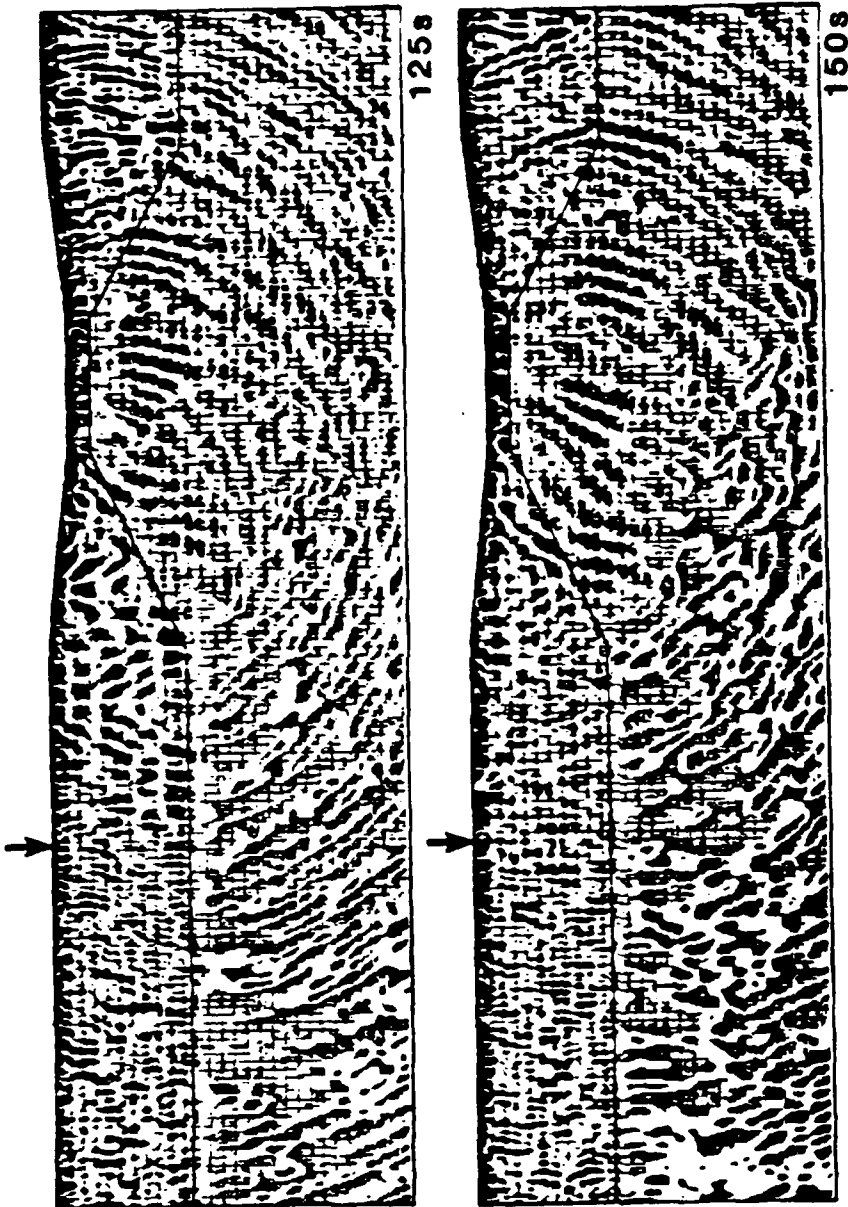


Figure 4: Time slices recorded during the calculation using an intermediate oceanic path length of 32 kilometers. Time slices for two later times illustrating the further propagation of the wavefield through the model. Details are the same as for Figure 1.

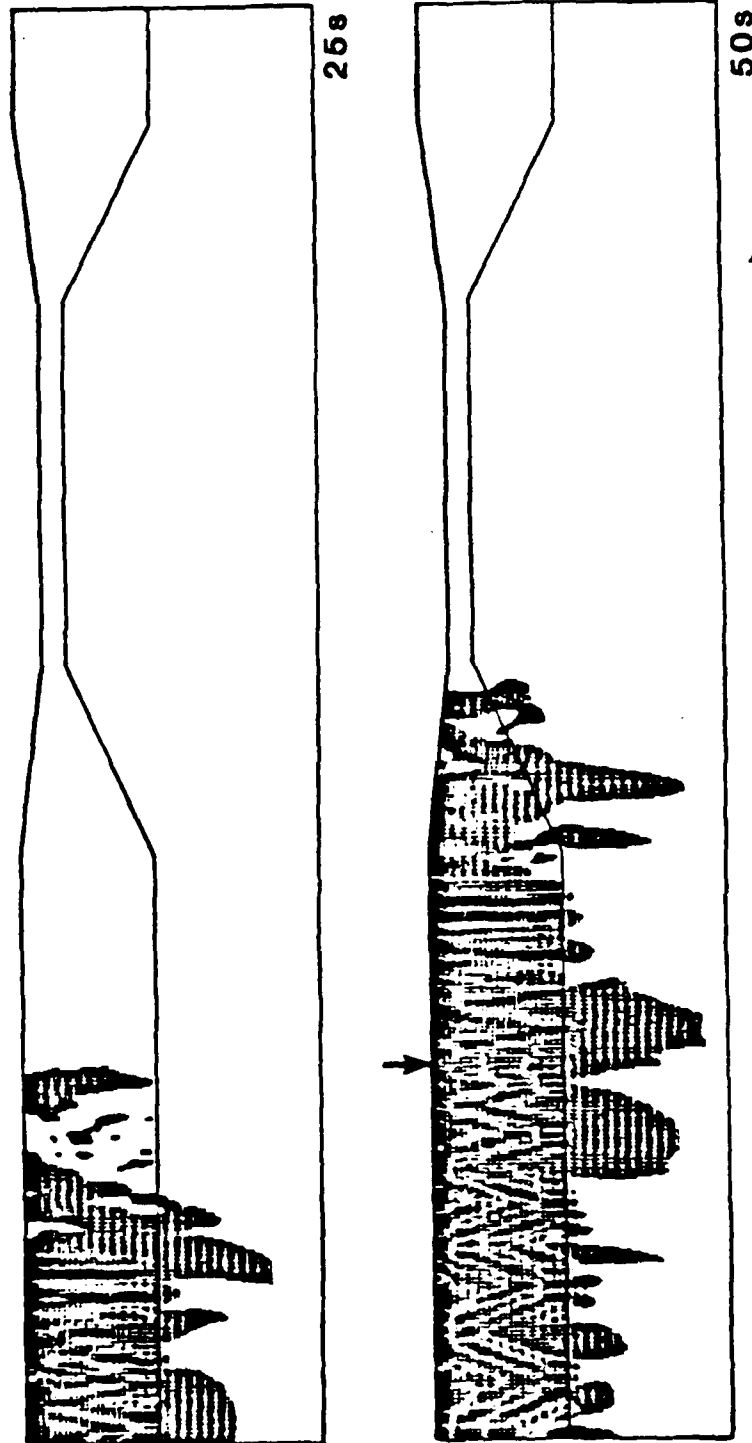


Figure 5: Time slices recorded during the calculation using an intermediate oceanic path length of 79 kilometers. Details are the same as for Figure 1.

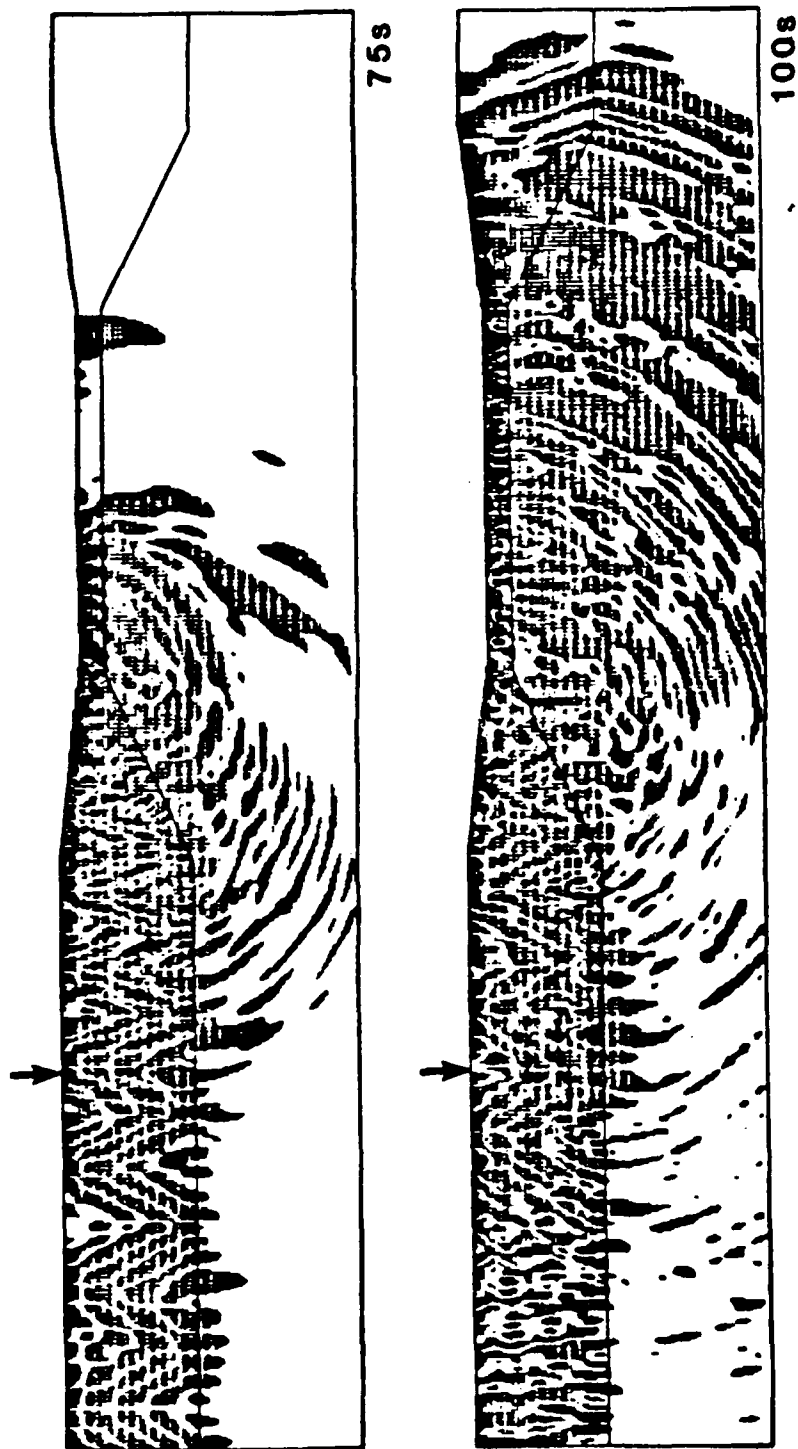


Figure 6: Time slices recorded during the calculation using an intermediate oceanic path length of 79 kilometers. Time slices for two later times illustrating the further propagation of the wavefield through the model. Details are the same as for Figure 1.

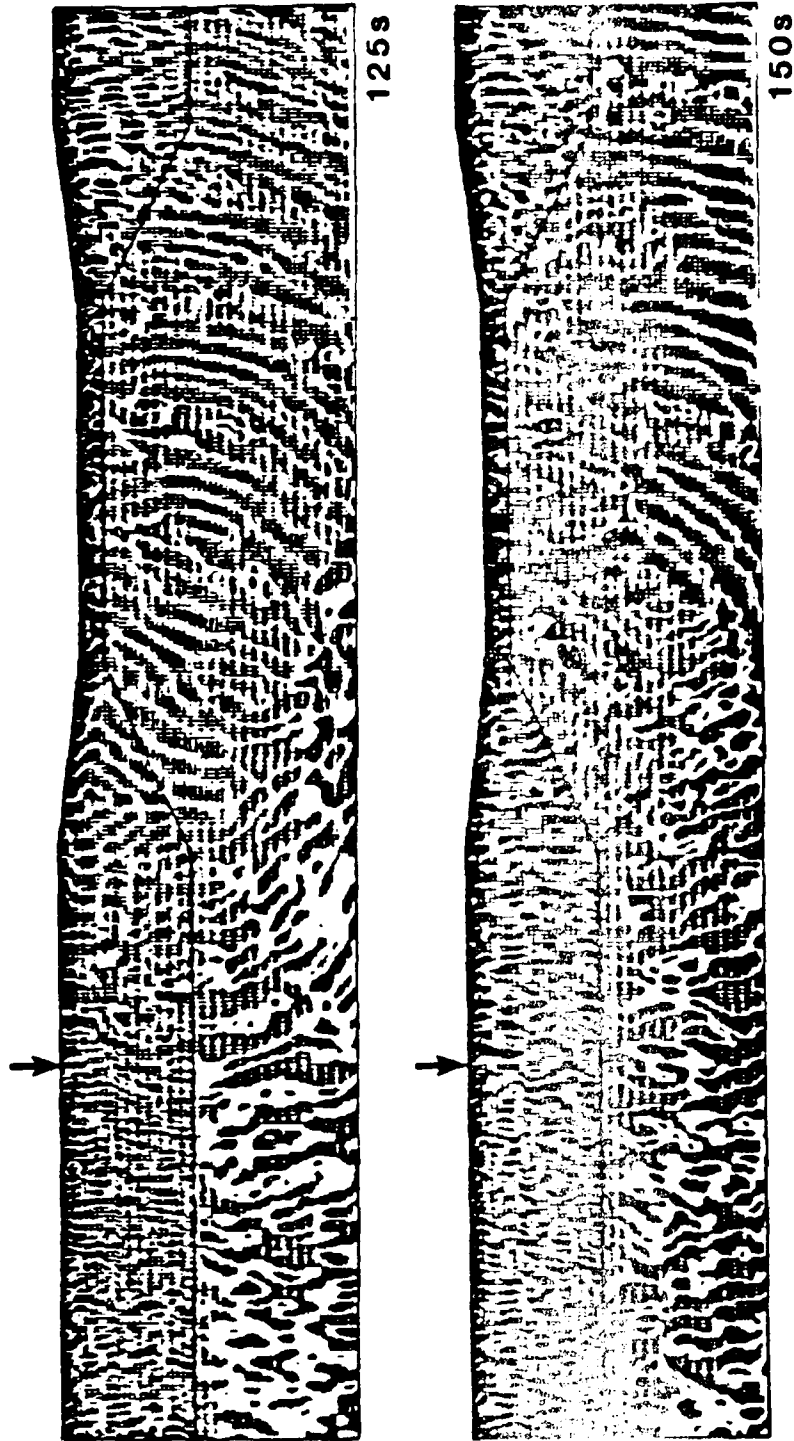


Figure 7: Time slices recorded during the calculation using an intermediate oceanic path length of 79 kilometers. Time slices for two later times illustrating the further propagation of the wavefield through the model. Details are the same as for Figure 1.

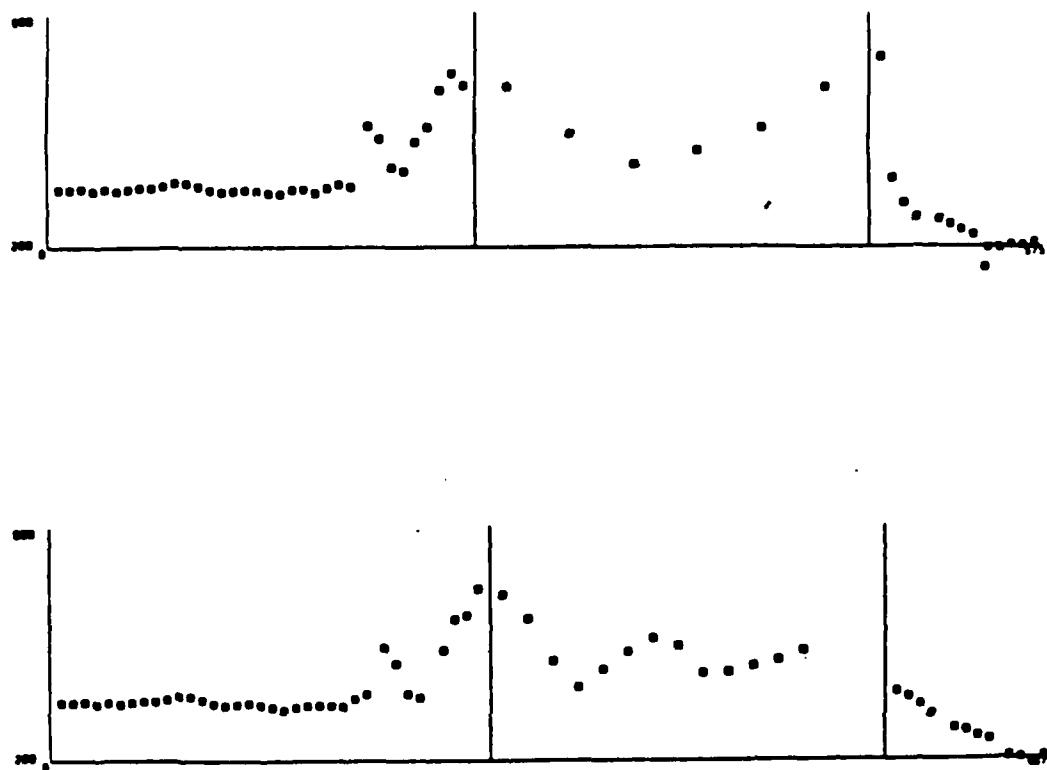


Figure 8: RMS surface amplitudes for the two FE models including both forward and reverse transitions. The upper plot shows the RMS surface amplitude for the model with an intermediate oceanic path of 31 km length. The lower plot shows the corresponding amplitude for the model with an intermediate oceanic path of 69 km length. The horizontal scale between the two vertical bars is different for each plot. This region represents the oceanic path. The scale between the vertical bars is chosen so that the shorter oceanic path plots with the same length as the longer one.

integral will be discussed in the next section. The determination of displacement and stress Green's functions is necessary in all applications of the RT integration method regardless of whether the forcing functions are FE results, analytic stress and displacement seismograms, or stresses and displacements from other sources. However, the stress seismograms are used in the following discussions only as an example of a well defined form of forcing functions. Using stress and displacement seismograms as forcing functions produces RT integration results which may be directly compared to purely analytic synthetics allowing one to verify the accuracy of the RT integration. For the SH problem in Cartesian coordinates the stresses that need to be considered are σ_{xy} and σ_{zy} . For the geometry used to couple surface waves from a FE grid into a layered medium through which the waves will be transmitted by convolution with propagator matrix generated Green's functions, only the stress σ_{xy} is used. However, σ_{zy} will also be derived for completeness. Should the geometry change so that it would be necessary to integrate over a horizontal surface such as the bottom of the grid then σ_{zy} would also be used.

The stresses, σ_{xy} and σ_{zy} , can be expressed in terms of spatial derivatives of displacements. One method of calculating values for these stresses is to express the derivative as a difference and evaluate the difference equation numerically. The expressions used to evaluate the stresses in the FE method are one such set of difference equations. They are

$$\sigma_{xy} = \mu \frac{\partial u_y}{\partial x} = \mu \frac{u_y(1) - u_y(2) - u_y(3) + u_y(4)}{4\Delta x} \quad (1a)$$

$$\sigma_{zy} = \mu \frac{\partial u_y}{\partial z} = \mu \frac{-u_y(1) - u_y(2) + u_y(3) + u_y(4)}{4\Delta z} \quad (1b)$$

In these expressions 1, 2, 3, 4, denote the positions of the nodes at the corners of the 2-D element (Figure 2, chapter 1) for which the element center stresses are σ_{xy} and

σ_{zy} . The displacement perpendicular to the FE grid is u_y , and the horizontal and vertical spacings of the nodes in the grid are Δx , and Δz respectively. Evaluating these relations gives a reasonable approximation to the desired stress values. A second, and more direct, method for determining the values of the stresses is to evaluate the analytic expression for each stress derived from the analytic displacement expressions. The derivations of analytic stress expressions are outlined below. Expressions for the stresses are determined for several different cases. First, dip slip and strike slip double couple sources are considered, then, a line source in a horizontally layered medium. Finally, the expressions for the line source Green's functions are derived.

The choice of evaluation of analytic expressions over the numerical calculation of derivatives is based on speed and accuracy. Evaluation of the analytic expressions for a stress component requires the same amount of calculation as the evaluation of a displacement. For a given depth section of n elements n element center stress components and n element center displacements need to be determined to evaluate the RT integral which propagates the wavefield from the RT surface through a layered structure to the receiver. Thus, if the calculation of each stress or displacement takes time t , the computation of the necessary displacement and stress components by evaluating the analytic expressions would take time $2nt$. When the stress component is determined using numerical differentiation, time $(2n+2)t$ is required to evaluate the displacements used in the difference equations, time nt is required to evaluate the element center displacements, and additional time is required to process the numerical difference equations. Clearly direct evaluation is faster. The calculation of numerical derivatives is known to be a potentially unstable numerical procedure since subtraction of almost equal numbers is possible. Thus, direct evaluation will be more reliable in cases where the numerical derivative becomes unstable. The analytic evaluation is also more accurate since it is equivalent to a numerical derivative with infinitesimal

spacing between the corners of the element. The accuracy of the numerical derivative increases as that spacing decreases. In practice, however, for the types of disturbances considered in this study, the increase in accuracy is small and both estimates are equally acceptable.

A numerical procedure is implemented to evaluate the analytic expressions for the stress components. The validity of the procedure is illustrated by comparing analytic stress time histories, determined by evaluation of equation (4) and (6) below, with corresponding results generated using the difference equations (1). The results of these comparisons are discussed after the analytic stress relations are developed.

The analytic expressions for the stress components for SH waves from a point double couple source are directly obtainable from the expressions used to determine the corresponding displacement seismograms. These expressions,

$$\left\{ \bar{v}(x,z) \right\} = -\frac{M_0}{2\omega} \Delta_L \frac{\partial H_2^{(2)}(k_L r)}{\partial r} \left[\frac{v_S(h)}{v_0} \right]_H \left[\frac{v_R(z)}{v_0} \right]_H \quad (2a)$$

$$\left\{ \bar{v}(x,z) \right\} = -\frac{M_0}{2\omega} \Delta_L \frac{1}{\mu_S} \frac{\partial H_1^{(2)}(k_L r)}{\partial r} \left[\frac{\dot{r}^*(h)}{\dot{v}_0 / c_L} \right]_H \left[\frac{v_R(z)}{v_0} \right]_H \quad (2b)$$

where the variables are as defined in chapter 1, lead to expressions for the stress σ_{zy} when their derivatives with respect to z are calculated. Only the final term in each equation depends directly on z . From Harkrider (1964)

$$\frac{\partial}{\partial z} \left[\frac{v_R(z)}{v_0} \right]_H = -\frac{k_L}{\mu_R} \left[\frac{\dot{r}^*(z)}{\dot{v}_0 / c_L} \right]_H \quad (3)$$

Substituting $\left\{ \bar{v}(z) \right\}$ from (2) for u_y in (1) and replacing the derivative of $\left[\frac{v_S(h)}{v_0} \right]_H$ by (3) gives

$$\left\{ \sigma_{zy}(x,z) \right\} = -k_L \frac{M_0}{2\omega} \Delta_L \frac{\partial H_2^{(2)}(k_L r)}{\partial r} \left[\frac{v_S(h)}{v_0} \right]_H \left[\frac{\dot{r}^*(z)}{\dot{v}_0 / c_L} \right]_H \quad (4a)$$

$$\{\sigma_{xy}(x,z)\} = -k_L \frac{M_0}{2\omega} \Delta_L \frac{1}{\mu_S} \frac{\partial H_1^{(2)}(k_L r)}{\partial r} \left[\frac{r^*(h)}{v_0 / c_L} \right]_H \left[\frac{r^*(z)}{v_0 / c_L} \right]_H \quad (4b)$$

Expressions (2) also yield the expressions for stress σ_{xy} when their derivatives with respect to x are calculated. All terms except the Hankel function are constant with respect to x . By expanding the Hankel function term in an asymptotic series for large r , and ignoring terms of order $\frac{1}{r}$, it can be shown that

$$\frac{\partial}{\partial x} \left(\frac{\partial H_2^{(2)}(k_L r)}{\partial r} \right) \approx -ik_L \frac{\partial H_2^{(2)}(k_L r)}{\partial r} \quad (5)$$

Then combining (1), (2), and (5) gives

$$\{\sigma_{xy}(x,z)\} = ik_L \mu_R \frac{M_0}{2\omega} \Delta_L \frac{\partial H_2^{(2)}(k_L r)}{\partial r} \left[\frac{v_S(h)}{v_0} \right]_H \left[\frac{v_R(z)}{v_0} \right]_H \quad (6a)$$

$$\{\sigma_{xy}(x,z)\} = ik_L \frac{\mu_R}{\mu_S} \frac{M_0}{2\omega} \Delta_L \frac{\partial H_1^{(2)}(k_L r)}{\partial r} \left[\frac{r^*(h)}{v_0 / c_L} \right]_H \left[\frac{v_R(z)}{v_0} \right]_H \quad (6b)$$

Equations (2) are the analytic expressions for displacement for the dip slip and strike slip faults, the corresponding expressions for the stresses are shown in (4) and (6).

The analytic expressions for a line source in a layered medium are derived by a procedure similar to that used in the previous section to obtain the stress expressions for the point double couple source. The same sequence of calculations is applied to the expression for the displacement produced by a 2-D line source as was applied to the expressions for the strike slip and dip slip displacements. These calculations yield the analytic 2-D line source stress equations. The displacement at depth z due to a line source at depth h is

$$\{\bar{u}_y(x,z)\} = 2\pi i \Delta_L \frac{\mu_S}{k_L} \left[\frac{v_S(h)}{v_0} \right]_H \left[\frac{v_R(z)}{v_0} \right]_H e^{-ik_L x} \quad (7)$$

In this case all terms in (7) except $\left[\frac{v_R(z)}{v_0} \right]_H$ are independent of z . Thus, the stress σ_{zy} has the same form as the displacement expression with $\left[\frac{v_R(z)}{v_0} \right]_H$ replaced by its derivative with respect to z , that is by the right hand expression of (3). Similarly, the stress σ_{xy} has the same form as the displacement with the exponential in x replaced by its derivative. Therefore, the stresses for the 2-D line source are

$$\left\{ \sigma_{zy}(x,z) \right\} = -2\pi i \mu_S \Delta_L \left[\frac{v_S(h)}{v_0} \right]_H \left[\frac{r'(z)}{v_0 / c_L} \right]_H e^{-ik_L x} \quad (8a)$$

$$\left\{ \sigma_{xy}(x,z) \right\} = 2\pi \mu_S \mu_R \Delta_L \left[\frac{v_S(h)}{v_0} \right]_H \left[\frac{v_R(z)}{v_0} \right]_H e^{-ik_L x} \quad (8b)$$

Next it is simple to extend the treatment used in the previous paragraph to the expression for the displacement Green's function for a line source in a layered half space. It has been previously shown that this Green's function is

$$\left\{ \Gamma_{22}(x,z;\xi_1,h) \right\} = -\frac{i}{k_L} \Delta_L \left[\frac{v_S(h)}{v_0} \right]_H \left[\frac{v_R(z)}{v_0} \right]_H e^{-ik_L(x-\xi_1)} \quad (9)$$

In this case a stress source term rather than a stress receiver term is needed. Thus, the z derivative is taken with respect to the source term. All terms in (9) except $\left[\frac{v_S(h)}{v_0} \right]_H$ are independent of z , so the σ_{zy} term has the same form as the displacement equation with $\left[\frac{v_S(h)}{v_0} \right]_H$ replaced by its derivative with respect to z . The form of this derivative is identical to that in (3) except that the R subscript is replaced by an S subscript denoting the properties at the source at the RT surface rather than at the receiver. Similarly the stress σ_{xy} has the same form as the displacement equation with the exponential term replaced by its derivative with respect to x . Therefore the derivatives of the Green's function are

$$\left\{ \Gamma_{22,3}(x,z;\xi_1,h) \right\} = \frac{i}{\mu_s} \Delta_L \left[\frac{r^*(h)}{v_0 / c_L} \right]_H \left[\frac{v_R(z)}{v_0} \right]_H e^{-ik_L(x-\xi_1)} \quad (10a)$$

$$\left\{ \Gamma_{22,1}(x,z;\xi_1,h) \right\} = -\Delta_L \left[\frac{v_s(h)}{v_0} \right]_H \left[\frac{v_R(z)}{v_0} \right]_H e^{-ik_L(x-\xi_1)} \quad (10b)$$

Now it is necessary to illustrate that expressions (4), (6), and (8), for the stress components give the correct results. The tests illustrated in Figures 9, 10, and 11 are analogous. In each case the upper trace in each pair is the displacement or stress as calculated using one of the sets of analytic expressions given above. The lower trace in each pair is the same displacement component, generated by averaging the surrounding four nodes, or the same stress component calculated using the difference equations (1) with $\Delta x = \Delta z = .5\text{km}$. The node spacings are chosen to correspond to those used in the FE calculations. The top pairs of traces are the $V=u_y$ displacements at the surface. The second pairs of traces are the stress σ_{xy} at 0.25 km depth, and the third pairs of traces are σ_{zy} at 0.25 km depth. The ratio of the analytic peak to peak amplitude to the numerical peak to peak amplitude is given for each pair of traces by the upper number beside that pair. The same type of ratio, analytic to numerical, is calculated using the RMS amplitudes of the seismograms and is shown as the lower number beside each pair. The quality of the waveform correspondence and the amplitude ratios remain essentially constant as one moves down the depth section. Figure 9 shows the results for the case of the 2-D line source, equation (8). The pairs of displacement and stress time histories show excellent correspondence when their waveforms are compared. Numerical derivatives for σ_{xy} agree with the corresponding analytic derivatives to within $\approx 4\%$ for peak to peak amplitude and to within $\approx 1\%$ for RMS amplitude. The peak to peak differences between the two methods are about 2% for the average displacement \bar{V} and the stress σ_{zy} . As expected, for all three cases, the correspondence improves as Δx and Δy are reduced. Figure 10 shows the results

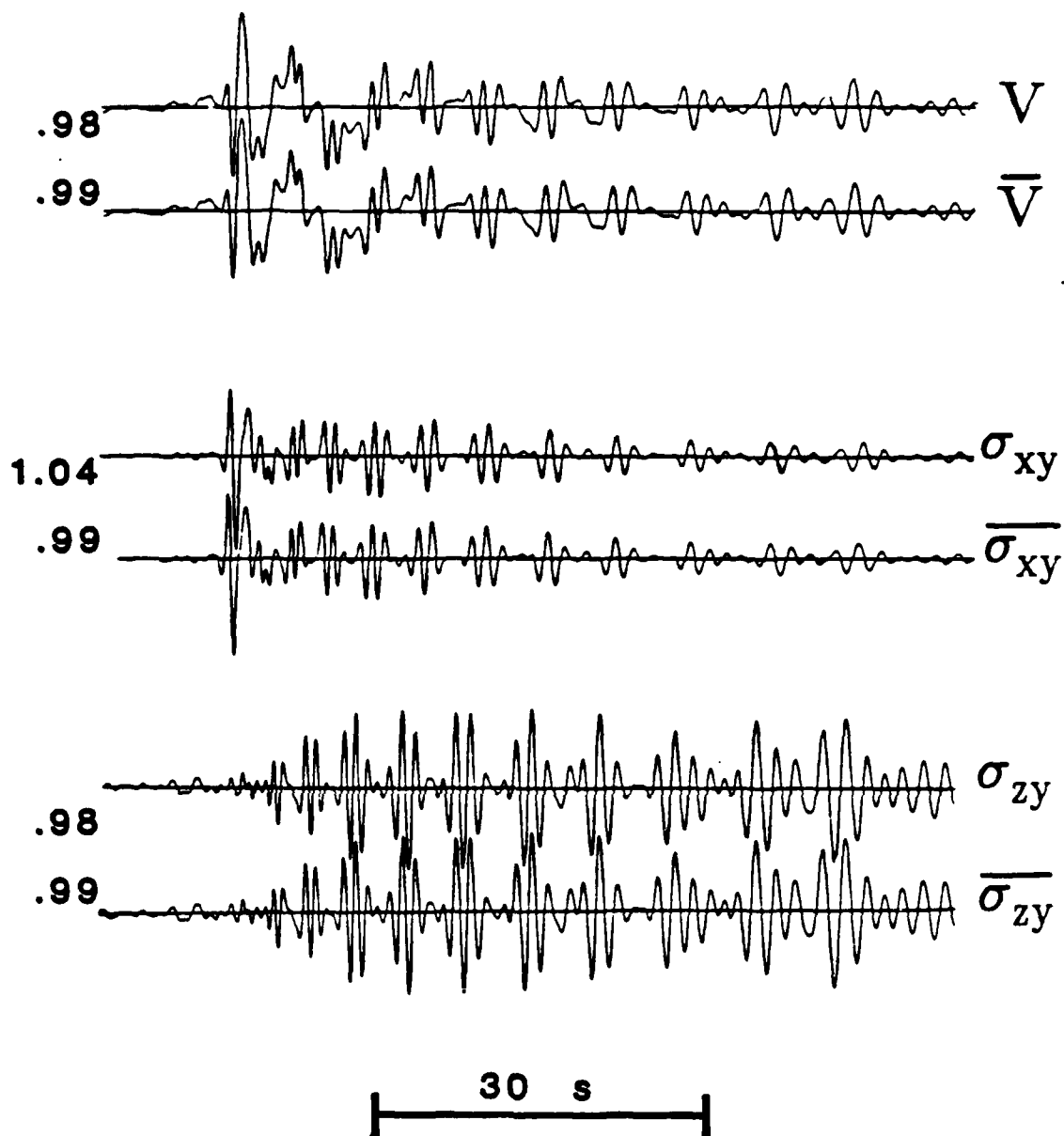


Figure 9: Comparison of element center displacement and stress time histories calculated for a 2-D line source using two methods. Upper traces in each pair are evaluations of the analytic expressions at the element centers. Lower traces are determined by using displacements calculated at the nodes surrounding the element center to evaluate the difference equations. For all traces $\Delta=1500$ km, and source depth is 8 km. The fundamental and first five higher modes are included in the synthetics. The upper number to the left of each trace is the peak to peak amplitude ratio of the numerical to analytic calculations, the lower number is the corresponding RMS amplitude ratio.

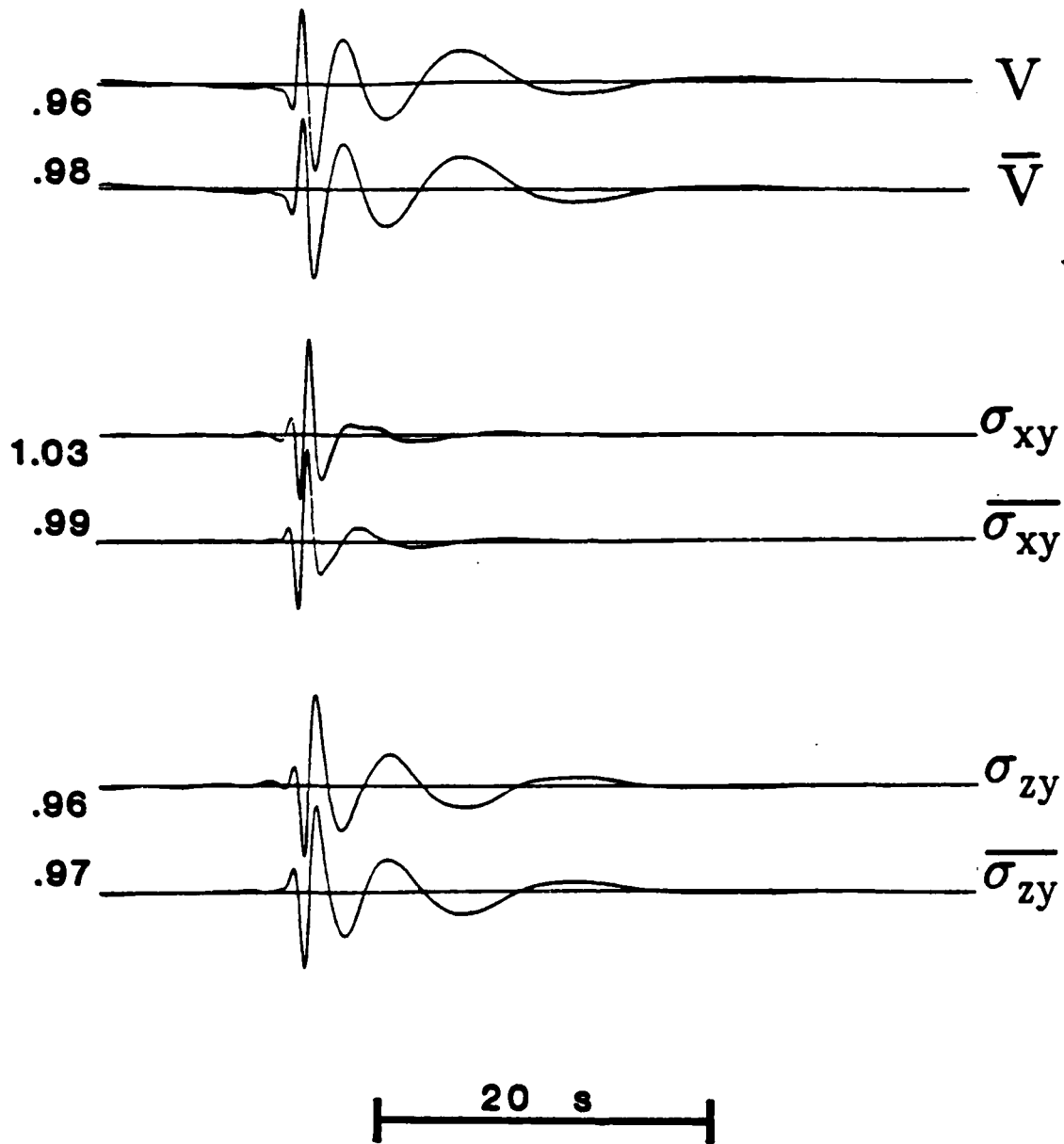


Figure 10: Comparison of element center displacement and stress time histories calculate for a strike slip type double couple source using two methods. Only the fundamental mode is illustrated. Other details are the same as for figure 9.

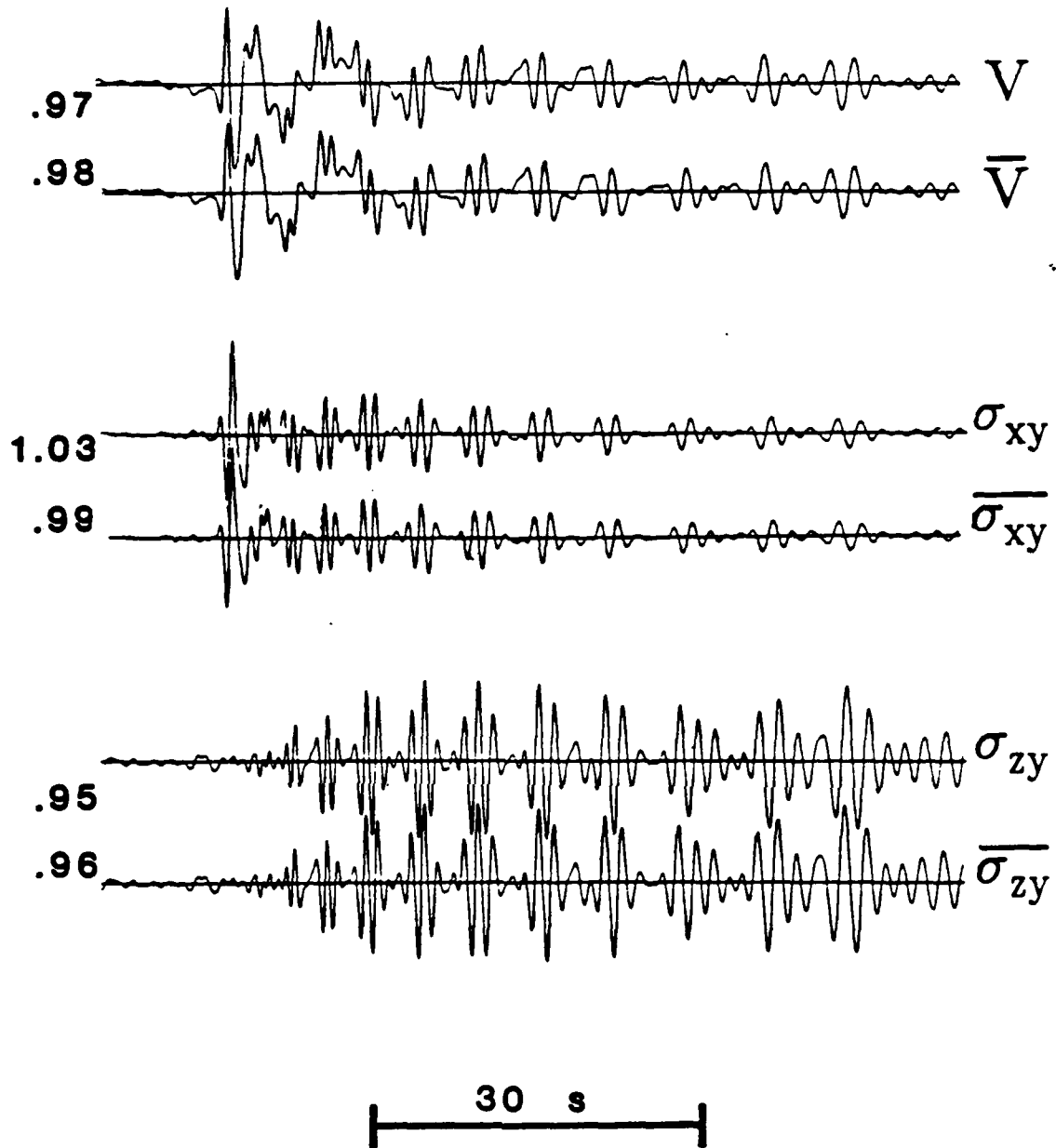


Figure 11: Comparison of element center displacement and stress time histories calculated for a strike slip type double couple source using two methods. Details are the same as for Figure 9.

for the case of a strike slip source, equations (4) and (6), using the fundamental mode only. Again, the waveform correspondence within each pair is excellent. The peak to peak amplitude ratios are close to one, showing less than 4% difference. Since the major variation between the two methods is the resolution of the magnitude of the high frequency peak near the onset of the trace the RMS amplitudes show a smaller variation of 2.5% or less. Figure 11 shows the results for the strike slip source, for a mode sum including the fundamental mode and the first five higher modes. The waveforms do not match as precisely as in the case of the fundamental mode alone, but the correspondence is still excellent. The amplitude ratios do not significantly change when the higher mode energy is added. Again, both for the fundamental mode alone and for the mode sum, correspondence between the analytic and numerical methods of evaluation improves rapidly as Δx and Δz are reduced. These tests not only indicate the validity of the analytic expressions above, they also give an estimate of the uncertainties present in the numerical differentiation used in the FE calculations.

RT Coupling of Analytic 2-D Seismograms and Green's Functions

In this section the validity and accuracy of the numerical implementation of the Representation Theorem coupling technique, used in the following section to pass FE results into a layered media, will be discussed in detail. The tests discussed below are designed to give RT integration results directly comparable with purely analytic results. First mode by mode results are presented to illustrate where the discrepancies between the RT results and the analytic results originate. Mode sum results are then presented. The form of the RT integral and its relation to the propagator matrix formulation is discussed and a method for mode by mode filtering of mode sum forcing function input is explained. The type of formulation used to explain the filtering method is also applied to derive more quantitative mode by mode analysis of the

origins of discrepancies between RT integration results and purely analytic solutions. These quantitative estimates of the sources of discrepancies explain the differences seen between the RT integration results and the purely analytic results quite well.

All the results discussed in this section are derived using a simple geometry. In all cases the model is a layer over a half-space. The layer has a thickness of thirty two kilometers, a SH wave velocity 3.5 km/s, and a density 2.7 g/cm³. The half-space has SH wave velocity 4.5 km/s and density 3.4 g/cm³. The same layer over a half space model is used for the entire path, making calculation of purely analytic synthetic for the entire path length of $\Delta = 1600$ km, or $\Delta = 1750$ km simple. Purely analytic synthetic seismograms were calculated at these distances for the mode sum and separately for each of the fundamental mode and the first five higher modes. The forcing functions used are the displacement and stress seismograms for a line source at at depth of ten kilometers and a distance of $\Delta = 1500$ km from the source. The forcing functions are evaluated at positions corresponding to the element centers of the rightmost column of elements in a FE grid with horizontal and vertical spacing of .5 km, whose right hand edge lies $\Delta = 1500.25$ km from the source. Thus, the seismograms are evaluated at points along a vertical surface, at depth intervals of 0.5 km, beginning at a depth of 0.25 km below the surface. All forcing functions are evaluated at a distance of $\Delta = 1500$ km. Separate sets of forcing functions were generated for each mode. A set of forcing functions which is a sum over the fundamental and the first five higher modes was also calculated. The displacement seismograms calculated using the RT integral are for distances of $\Delta = 1600$ km, or $\Delta = 1750$ km. Performing RT integrations to determine hybrid solutions at these distances requires Green's functions for propagation distances $\Delta = 100$, or $\Delta = 250$ km. At each of these distances a set of stress and displacement Green's functions was determined for each mode and an additional set was determined for a mode sum including the fundamental and the

AD-A193 562

BODY AND SURFACE WAVE MODELING OF OBSERVED SEISMIC
EVENTS PART 3(U) CALIFORNIA INST OF TECH PASADENA
SEISMOLOGICAL LAB R W CLAYTON ET AL. 13 MAY 87

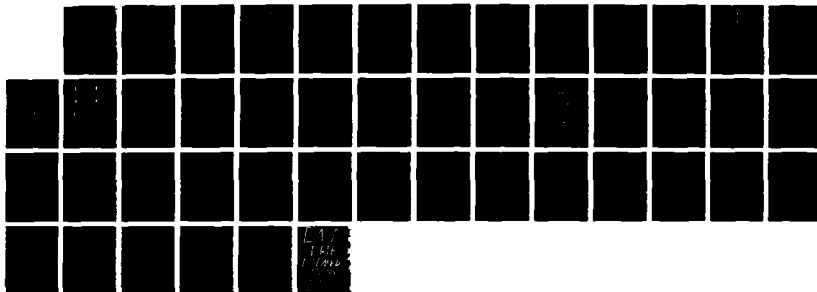
2/2

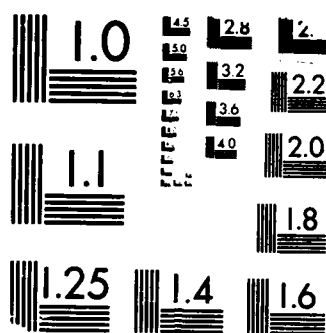
UNCLASSIFIED

AFGL-TR-87-0150 F19628-05-K-0017

F/G 17/10

NL





MICROCOPY RESOLUTION TEST CHART
 NATIONAL BUREAU OF STANDARDS-1963-A

first five higher modes. The Green's functions in each set were evaluated for a source at each of the locations where displacement and stress forcing functions were determined and a receiver at the surface. The RT integration surface for these examples extended to a depth of 37.5 km and included seventy five integration points. In the following discussions the seismogram resulting from a RT integration may be referred to as a hybrid seismogram, even though, for these tests of accuracy, the same method is being used to generate Green's functions and forcing functions.

The first group of tests using the sets of forcing functions and Green's functions discussed above produced mode by mode RT integration results to compare to the purely analytic synthetic single mode seismograms. The set of single mode forcing functions for each of the individual modes, was convolved with the single mode set of Green's functions for the same mode according to the RT integration relation. This produced a hybrid seismogram for that mode to compare to the corresponding purely analytic synthetic. Comparisons of the RT integration sums and the purely analytic synthetics for each individual mode are shown in Figures 11 and 12. In Figure 11 comparisons for the fundamental mode, the first higher mode, and the second higher mode are presented. Each of these pairs is illustrated at a distance of $\Delta = 1600$ km from the source. Figure 12 is a continuation of Figure 11 showing the results for the third through fifth higher modes. The upper two pairs of traces are also illustrated for a distance $\Delta = 1600$ km. The lowermost pair of traces, those for the fifth higher mode, are illustrated at a distance of $\Delta = 1750$ km from the source. The fifth higher mode results at 1500 km are equally well fit, but presenting an example for another distance helps verify the observation that the goodness of fit between the hybrid seismograms and the analytic synthetics does not depend significantly on distance propagated using the RT integration over stress and displacement seismograms and Green's functions. In each of these figures there are three pairs of seismograms. The

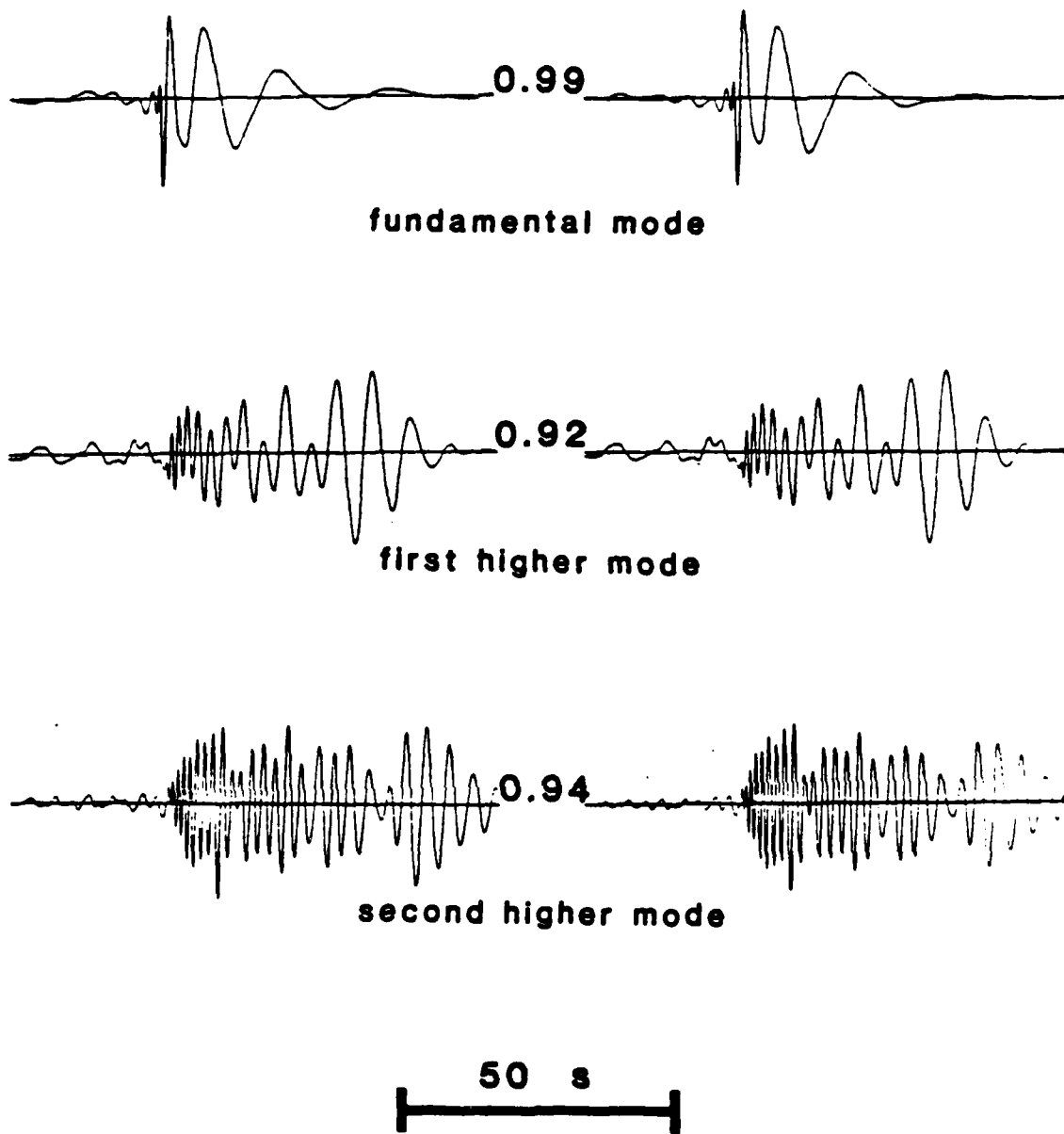
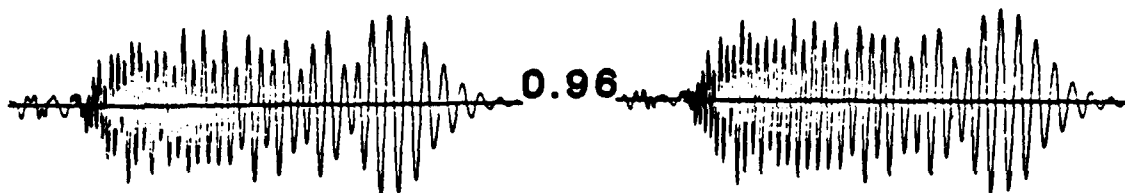


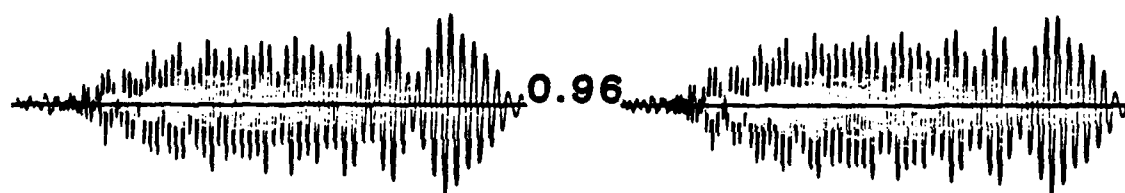
Figure 12: Comparison of analytic and hybrid synthetics at $\Delta=1600\text{km}$. The hybrid synthetics are transmitted the first 1500 km using the propagator method, and the remaining 100 km using RT integration with propagator generated Green's functions. The left column of seismograms shows the analytic synthetics and the right column the hybrid synthetics. The results are presented mode by mode, and the mode is identified below each pair of traces. The number between each pair of traces is the ratio of the RMS amplitude of the hybrid trace to the RMS amplitude of the analytic trace.



third higher mode



fourth higher mode



fifth higher mode

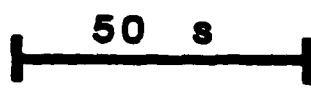


Figure 13: Comparison of analytic and hybrid synthetics at $\Delta=1600$ km. This figure is a continuation of Figure 12 showing the remaining modes. Other details are the same as for Figure 12.

leftmost seismogram in each pair shows the purely analytic synthetic, the rightmost seismogram shows the hybrid synthetic produced by RT integration. Between each pair of seismograms is a number indicating the ratio of the RMS amplitude of the hybrid synthetic to the RMS amplitude of the purely analytic synthetic. Below each pair of traces is a label indicating which mode is being illustrated. All the seismograms are bandpass filtered for periods between one and twenty-five seconds. The long period limit on the band pass filter was chosen to improve the correspondence between the waveform of the purely analytic synthetic and the RT integration result for the same mode. Longer periods seem to be poorly reconstructed by the RT integration, and are consequently filtered out of the displayed results. The filtering has the largest effect for the first two higher modes, and has a progressively smaller effect for each successive higher mode. Higher mode results depend less on the long periods and produce an increasingly good fit even before filtering. The increasing discrepancies between the purely analytic and the hybrid synthetics for successively lower higher modes is due to the larger proportion of long periods in those modes, and is a likely source of discrepancies in the mode sum calculations presented in the next paragraph and will be explained later in terms of the quantitative estimates of error yet to be derived.

The next test conducted was the RT integration using the mode sum forcing functions and Greens functions. The hybrid synthetic resulting from this integration is compared to the purely analytic mode sum synthetic in Figure 14. In this figure the hybrid synthetic is labeled mode sum and the purely analytic synthetic is labeled analytic. The seismogram labeled sum of single modes is calculated by summing the hybrid solutions for each individual mode to produce another estimate of the mode sum hybrid synthetic. Clearly the waveforms of all three seismograms are extremely similar. The numbers to the left of each of the lower two seismograms indicates the

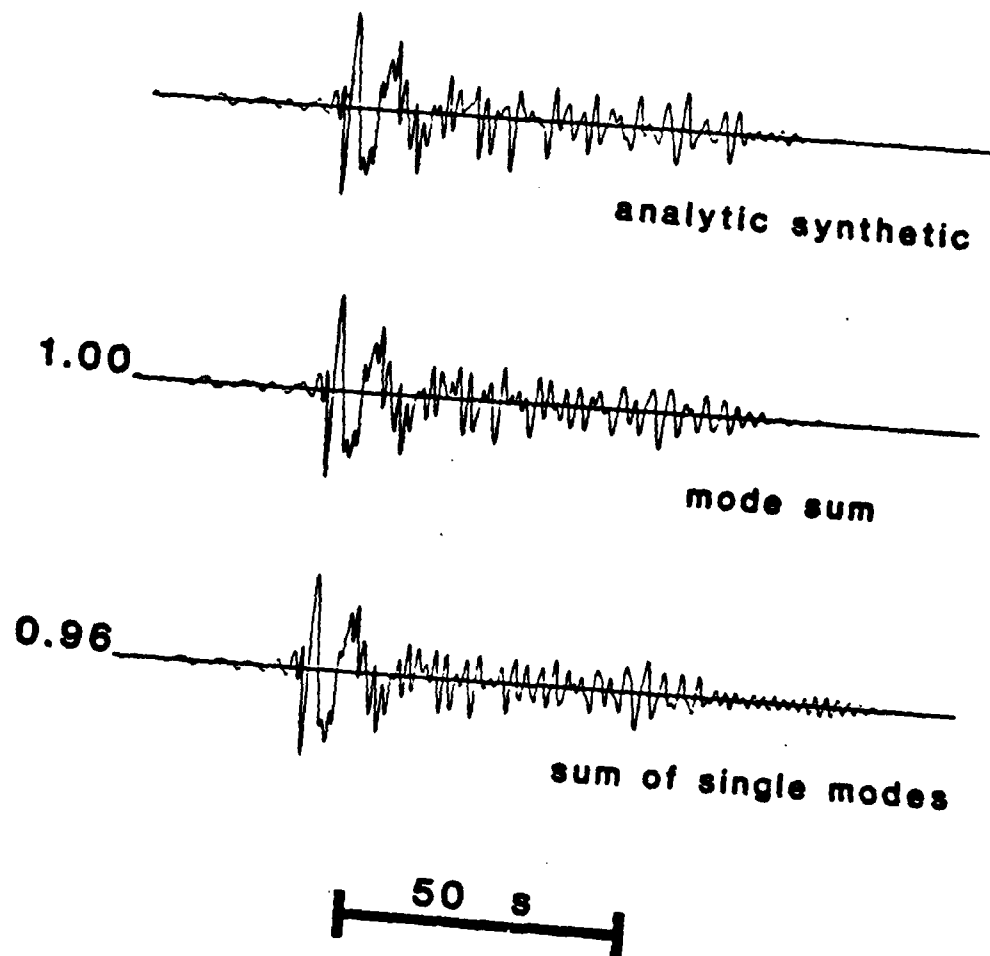


Figure 14: Comparison of analytic and hybrid mode sum seismograms. The upper seismogram, labeled analytic synthetic is calculated using the propagator technique for the whole path. The center seismogram, labeled mode sum, is calculated using a RT integration of mode sum Green's functions and forcing functions. The lower seismogram, labeled sum of single modes, is the sum of the RT integration results for each individual mode.

ratio of the RMS amplitude of that seismogram to the RMS amplitude of the purely analytic mode sum seismogram. The agreement in amplitude between the purely analytic and hybrid mode sum results is better than the agreement seen for any single mode. This improvement in agreement is probably fortuitous. The mode sum synthetic calculated as a sum over the single mode hybrid results shows a more realistic amplitude measure consistent with the single mode results previously presented.

The RT integration is accomplished by the evaluation of the following expression based on integrating equation 32 of chapter 1 along a vertical surface.

$$u_2(\vec{x}, t) = \int_0^{\infty} \left\{ \Gamma_{22}(x, z; \xi_1, \xi_3) u_{2,1}(\xi_1, \xi_3) + \Gamma_{22,1}(x, z; \xi_1, \xi_3) u_2(\xi_1, \xi_3) \right\} n_1 d\xi_3 \quad (11)$$

In this expression the displacement at time t at location \vec{x} is determined as a RT integral. The forcing functions, $u_2(\xi_1, \xi_3)$ and $\mu_S u_{2,1}(\xi_1, \xi_3)$ are evaluated on the vertical surface perpendicular to the propagation direction at a distance ξ_1 from the origin for points with a range of values of ξ_3 . Thus, the propagation distance for the forcing functions is ξ_1 . The Green's functions, Γ_{22} and $\Gamma_{22,1}$ are evaluated by placing a source point in each position where a forcing function is evaluated. By substituting alternate expressions, in terms of the variables used in the Propagator matrix method, for the Green's functions and forcing functions in equation (11) the Representation Theorem can be expressed in terms of terms constant with respect to ξ_3 times a simple integral with ξ_3 as an integration variable. To derive this form of the RT equation (9) is substituted for $\Gamma_{22}(x, z; \xi_1, \xi_3)$, and equation (8b) is substituted for $\Gamma_{22,1}(x, z; \xi_1, \xi_3)$. Also, equation (7) is substituted for $u_2(\xi_1, \xi_3)$, and equation (10b) for $u_{2,1}(\xi_1, \xi_3)$. Performing these substitutions gives

$$u_2(\vec{x}, t) = \int_0^{\infty} \mu(\xi_3) 4\pi \frac{\mu_S}{k_L} \left[\frac{v_S(h)}{v_0} \right]_H \left[\frac{v_R(z)}{v_0} \right]_H \Delta_L^2 e^{ik_L x} \left[\frac{v_R(\xi_3)}{v_0} \right]_H \left[\frac{v_R(\xi_3)}{v_0} \right]_H d\xi_3 \quad (12)$$

When the above mentioned substitutions into equation (11) are performed it becomes evident that both convolutions in the integrand of equation (11) produce identical expressions. Therefore, it should be possible to accelerate the numerical evaluation of (11) by evaluation only one of the convolutions and then doubling the resulting solution. This approach had the additional advantage that it makes it unnecessary to record both displacement and stress time histories in the FE calculations. Either one of these should be sufficient to calculate a 2-D SH RT integral. Even more useful is the fact that the equality of the two convolution terms allows determination of the value of the RT integral with the evaluation of half the number of Green's function. Tests have been conducted to investigate the validity of this approach. The waveforms of the solutions, for complete evaluation of the RT integral, and for evaluation of either term in the integral are indistinguishable when the resulting seismograms are examined. Thus, it was considered unnecessary to illustrate the results from these tests. The amplitudes of the sums of each term in the integral of (11), however, were not necessarily identical. Using the term containing the displacement and the Green's function stress general yielded amplitudes a percent or two higher than using the other term. These amplitudes were usually in better agreement with the synthetic than the amplitudes determined by summing the two terms. The differences in amplitude agreement are small enough to be ignored. Further calculations of the RT integral may be done by doubling the value of the first term in (11) without significantly affecting the solution.

Returning to equation (12) it is clear that many of the terms do not depend upon the integration variable ξ_3 . Taking these terms outside the integral and then comparing them to equation (7) allows equation (12) to be simplified to

$$u_2(\vec{x}, t) = u_2(\vec{x}, t) * 2\Delta_L \int_0^\infty \mu(\xi_3) \left[\frac{v_R(\xi_3)}{v_0} \right]_H \left[\frac{v_R(\xi_3)}{v_0} \right]_H d\xi_3 \quad (13)$$

Defining I_1 to be the relation

$$I_1 = \int_0^\infty \mu(\xi_3) \left[\frac{v_R(\xi_3)}{v_0} \right]_H \left[\frac{v_R(\xi_3)}{v_0} \right]_H d\xi_3 \quad (14)$$

immediately leads to the relation

$$\Delta_L = \frac{1}{2I_1} \quad (15)$$

Later the use of this last relation in the estimation of the minimum error for each mode will be discussed. First some consequences of equation (14) will be considered. It is well known that if i and j represent two different modes for a given period, that is $k_i \neq k_j$ for $\omega_i = \omega_j$, or for a given wave number $k_i = k_j$, $\omega_i \neq \omega_j$, then the orthogonality relation for Love waves states that

$$\int_0^\infty \rho(z) v_i(z) v_j(z) dz = 0 \quad i \neq j \quad (16)$$

In this equation v_i is the equivalent of the component of u_2 in equation (14) due to the single mode i . Comparing (14) and (16) shows that equation (14) is a form of the orthogonality relation. At this point it is useful to notice that the two $\left[\frac{v_R(\xi_3)}{v_0} \right]_H$ terms in the equation (14) each have separate origins. One originates with the forcing functions and the other with the Green's functions. Thus, any single modes not common to both the $\left[\frac{v_R(\xi_3)}{v_0} \right]_H$ term from the forcing function and the $\left[\frac{v_R(\xi_3)}{v_0} \right]_H$ term from the Green's function will produce zero contribution to the resulting hybrid result. This implies that the only modes present in both the Green's functions and the forcing functions will be present in the RT integration results. Thus, choosing Green's functions with a subset of the modes present in the forcing function will produce a filter that gives RT integration results that contain only that subset of modes. This is

demonstrated in the next set of numerical experiments.

A series of calculations investigating the accuracy and efficiency of the use of a Green's functions, containing only a subset of the modes present in the forcing functions, as a filter to extract only those modes from the forcing functions has been completed. In particular, the single mode sets of Green's functions were used in the RT integral along with the mode sum set of forcing functions. A RT integration was completed for each single mode set of Green's functions. Figure 15 presents results of the RT integration of the mode sum forcing functions and the fundamental mode Green's functions. Figure 16 is analogous to figure 15 but uses the third higher mode Green's function set. In each of these figures two columns of five seismograms are illustrated. The left column shows results of the single mode Green's functions integrated with the mode sum forcing functions. The right column shows the results of integrating single mode Green's functions with single mode forcing functions. The RT integration is numerically evaluated by summing the convolutions at discrete points along the RT surface. The sum begins with the point nearest the surface and then adds points at steadily increasing depth. In Figures 15 and 16 the first row of seismograms is a single convolution, the sum down to a depth of 0.25 km. The second row is the sum of 15 convolutions, and includes all integration points to a depth of 7.25 km. This pattern continues with the depth of the deepest point included in the integration indicated to the right of each pair of seismograms. The numbers between each pair of seismograms indicate the ratio of the RMS amplitude of the left trace to the RMS amplitude of the right trace. For the fundamental mode case this amplitude ratio varies only slightly with depth and shows a trend of increasing with depth only in the upper eight kilometers. However, as illustrated by the third higher mode, the higher mode ratios continue increasing with depth to much larger depths. This implies that the integration must proceed to a reasonable depth for the amplitude of the filtered mode sum

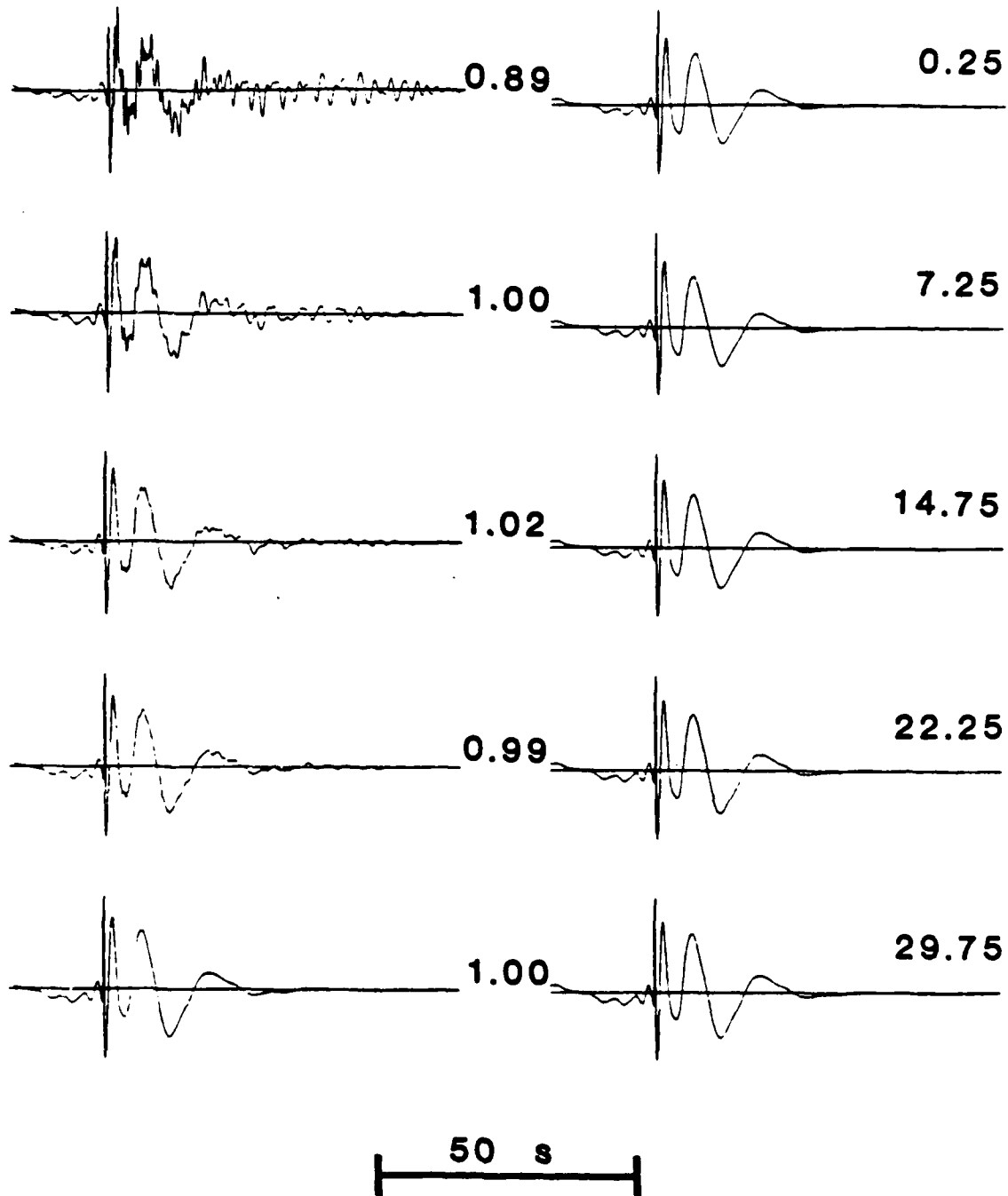


Figure 15: Comparison of hybrid synthetics at $\Delta=1600$ km. The traces in the left column are calculated by RT convolution of the mode sum forcing functions calculated at $\Delta=1500$ km with the fundamental mode Green's functions for 100 km further propagation. The traces in the right column are determined by RT convolution of fundamental mode forcing functions for $\Delta=1500$ km and the same Green's functions as the left column. The numbers to the right of each pair of seismograms show the depth to which integration along the RT integration surface has been completed. The central numbers show the RMS amplitude ratio of the right trace to the left trace.

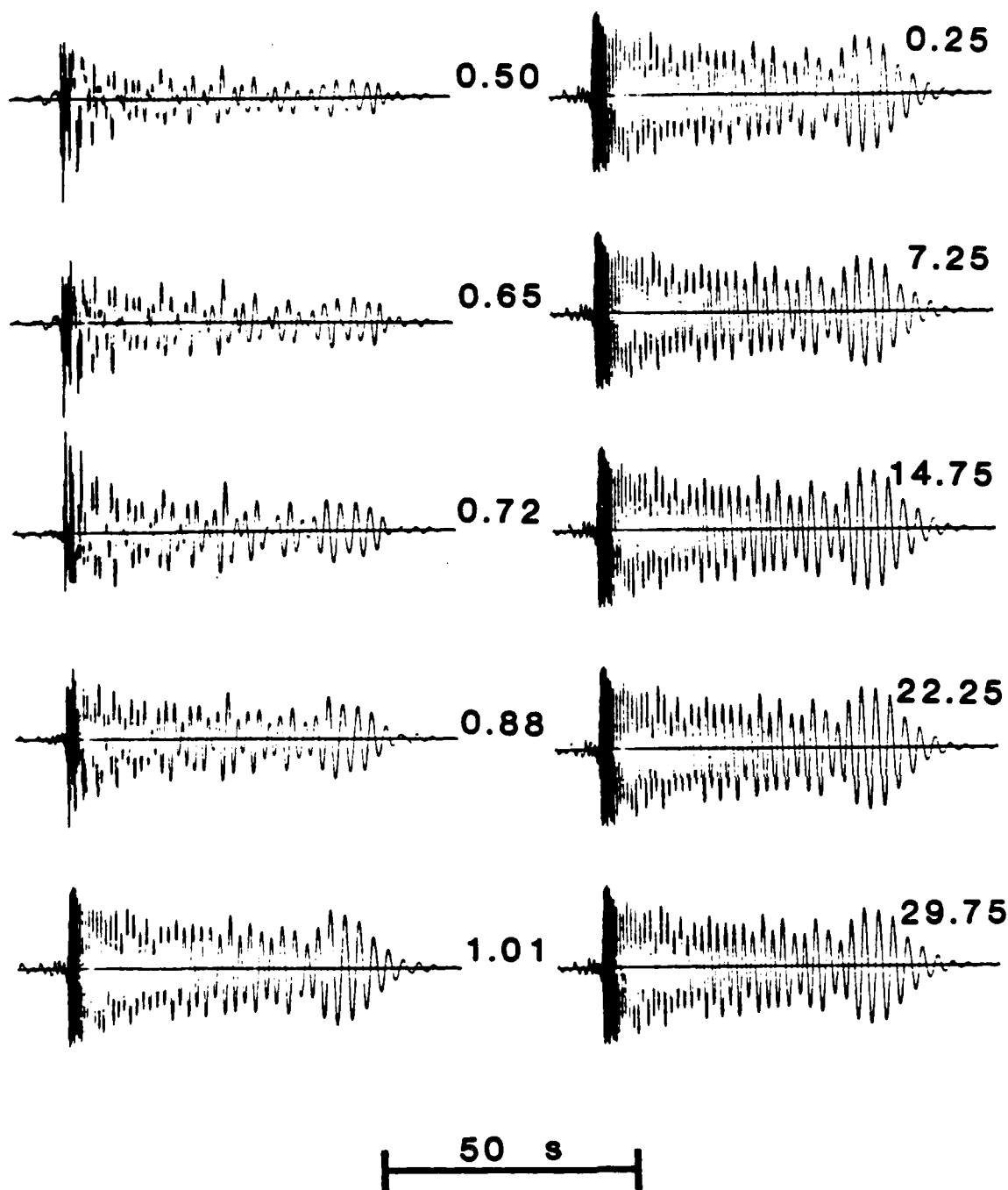


Figure 16: Comparison of hybrid synthetics at $\Delta=1600$ km. The traces in the left column are calculated by RT convolution of the mode sum forcing functions calculated at $\Delta=1500$ km with the third higher mode Green's functions for 100 km further propagation. The traces in the right column are determined by RT convolution of third higher mode forcing functions with the same Green's functions as the left column. The numbers to the right of each pair of seismograms and between each pair of seismograms have the same meanings as for Figure 14.

seismogram to reach that of the single mode hybrid results. For the modes investigated it was determined that the amplitude ratios stabilized near or above the base of the crustal layer, and that when the amplitudes had stabilized the waveforms of the two calculations showed little difference and remained relatively stable. Figures 17 and 18 illustrate the mode by mode results of the test discussed above. Rather than show the detailed progression to the stable result as in the previous two figures, a depth of thirty kilometers was chosen as the vertical extent of integration. This allows the illustration of the results of all six modes in two figures. In these figures two columns of seismograms are illustrated. The left column shows the results using the mode sum forcing functions and the single mode Green's functions. The right column shows the results using the single mode forcing functions and the single mode Green's functions. The numbers between each pair of seismograms indicate the ratio of the RMS amplitude of the left trace to the RMS amplitude of the right trace. Below each pair of seismograms the mode of the Green's functions is indicated. These seismograms appear different from those shown in Figures 12 and 13 since they have not been filtered before plotting. In summary, the effect of using a set of Green's functions containing a subset of the modes present in the set of forcing functions is to produce an efficient filter that allows only the modes common to both sets to appear in the hybrid result.

Now it is time to return to the analysis of the accuracy of the RT integration for a given single frequency mode. Rearranging equation (15) gives

$$2\Delta_L I_1 = 1 \quad (17)$$

Evaluation of this simple equation provides a direct estimate of the accuracy of the integration on a mode by mode basis. The estimate of the accuracy is obtained by evaluating the I_1 integrand at each integration point used in the RT integration, for each frequency on each branch of the dispersion curve used. For each single frequency

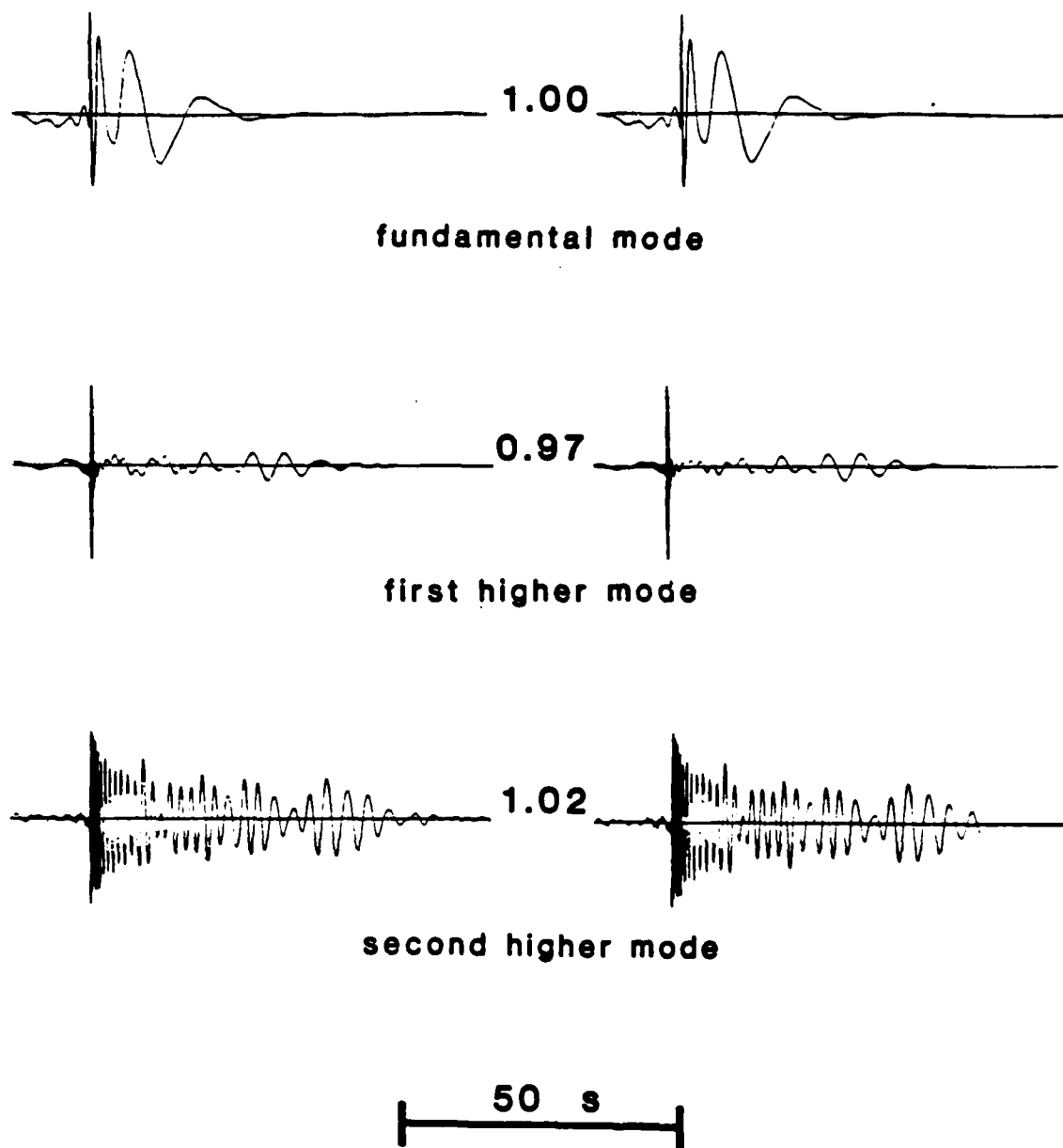
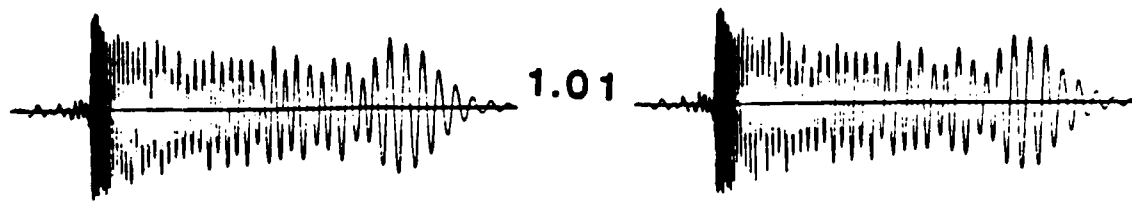
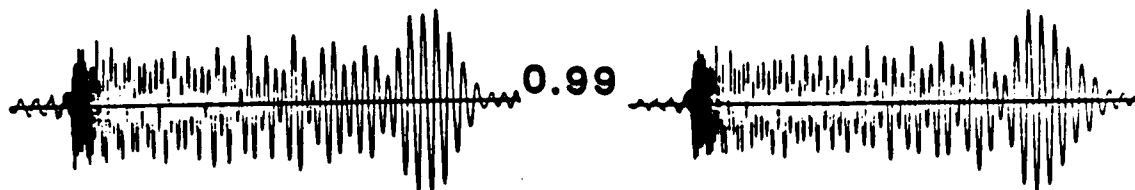


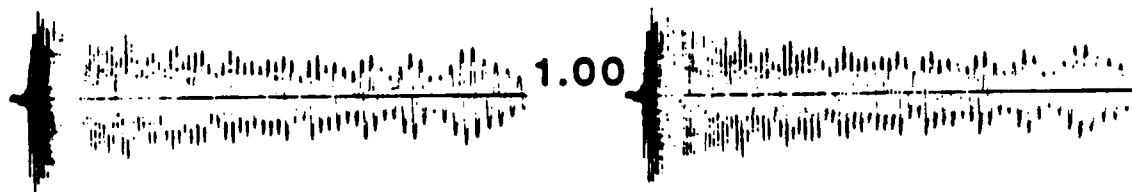
Figure 17; Comparison of synthetics at $\Delta=1600\text{km}$. The synthetics are transmitted the first 1500 km using the propagator method, and the remaining 100 km using RT integration with propagator generated Green's functions. The left column of seismograms shows the RT convolution of the mode sum forcing functions and the Green's functions of the indicated mode, the right column shows synthetics resulting from RT integration of forcing functions and Green's functions of the indicated mode only. The results are presented mode by mode, and the mode is identified below each pair of traces. The number between each pair of traces is the ratio of the RMS amplitude of the left trace to right trace.



third higher mode



fourth higher mode



fifth higher mode

50 s

Figure 18: Comparison of synthetics at $\Delta=1600$ km. This figure is a continuation of Figure 12 showing the remaining modes. Other details are the same as for Figure 12.

mode the quantity on the right hand side of equation 17 is determined at each integration point and summed over the integration surface. If the solution were perfect with no error present, then the sum would be exactly one. In practice the sum departs from one by some amount which gives an estimate of the size of the minimum error that could be expected in that mode in the RT integration results. The estimate is a minimum since it does not account for the phase of the arrivals nor for possible errors in that phase. The evaluation of the error using this relation is much faster than comparing results from multiple applications of RT theorem coupling. For example generating the tables on pages 219 and 220 which show the effects of varying grid spacing or of varying the vertical extent of the RT integration surface on the errors took less than 25% the time needed for a single RT integration example.

The tables on pages 219 and 220 show the effects of grid spacing and vertical extent of the integration surface. In the tables z indicates the depth in kilometers to which the integration surface extends, Δx indicated the spacing between successive integration points on that surface, and T indicates the period of the given mode. For each combination of these parameters illustrated the numbers in the table are the values of $2\Delta_L I_1$. It is clear from examining these tables that the grid spacing is fine enough to yield good results. Halving or doubling the grid spacing makes less than one percent difference in the error estimates which are at a level of about 98.5%. Reducing the time spacing by as much as a factor of four made no significant differences in the estimates of accuracy. So no table was included to illustrate how accuracy changed with time spacing. Seeing the errors on a frequency by frequency basis also helps to understand the causes of the inaccuracies noted in the actual RT integration results. The only variation that made noticeable changes in the accuracy of individual modes was variation in the depth to which the integration surface was extended. This change was, as expected, largest in the longest period modes. At

fundamental mode

T	z=40 km			dx=0.5 km		
	dx=.25	dx=0.5	dx=1.0	z=40	z=70	z=100
1000.	.00071	.00071	.00071	.00091	.00208	.00325
500.0	.00287	.00261	.00284	.00364	.00831	.01296
250.0	.01151	.01147	.01139	.01457	.03295	.05098
90.00	.09059	.09027	.08964	0.1123	0.2336	0.3384
70.00	0.1509	0.1503	0.1492	0.1843	0.3613	0.4998
60.00	0.2057	0.2049	0.2033	0.2480	0.4617	0.6145
55.00	0.2443	0.2433	0.2414	0.2920	0.5248	0.6808
50.00	0.2937	0.2926	0.2902	0.3473	0.5974	0.7513
45.00	0.3574	0.3559	0.3529	0.4169	0.6787	0.8223
40.00	0.4389	0.4370	0.4332	0.5034	0.7654	0.8881
35.00	0.5404	0.5379	0.5329	0.6070	0.8500	0.9408
30.00	0.6584	0.6551	0.6486	0.7216	0.9203	0.9738
25.00	0.7793	0.7752	0.7669	0.8314	0.9653	0.9873
20.00	0.8817	0.8766	0.8664	0.9160	0.9841	0.9893
18.00	0.9134	0.9079	0.8969	0.9397	0.9865	0.9889
16.00	0.9390	0.9331	0.9215	0.9576	0.9874	0.9883
14.00	0.9586	0.9525	0.9402	0.9701	0.9874	0.9877
12.00	0.9729	0.9664	0.9535	0.9782	0.9870	0.9871
10.00	0.9825	0.9757	0.9623	0.9827	0.9865	0.9865
8.000	0.9883	0.9813	0.9674	0.9848	0.9861	0.9861
6.000	0.9913	0.9841	0.9697	0.9854	0.9856	0.9856
4.000	0.9924	0.9850	0.9702	0.9852	0.9852	0.9852
2.000	0.9924	0.9848	0.9696	0.9848	0.9848	0.9848
1.800	0.9924	0.9848	0.9695	0.9848	0.9848	0.9848
1.600	0.9923	0.9847	0.9694	0.9847	0.9847	0.9847
1.400	0.9923	0.9847	0.9693	0.9847	0.9847	0.9847
1.200	0.9923	0.9846	0.9693	0.9846	0.9846	0.9846
1.000	0.9924	0.9847	0.9693	0.9847	0.9847	0.9847
0.8000	0.9924	0.9847	0.9692	0.9847	0.9847	0.9847
0.7000	0.9924	0.9847	0.9692	0.9847	0.9847	0.9847
0.6000	0.9917	0.9839	0.9684	0.9839	0.9839	0.9839
0.5000	0.9924	0.9847	0.9691	0.9847	0.9847	0.9847
0.4000	0.9925	0.9847	0.9692	0.9847	0.9847	0.9847
0.3000	0.9925	0.9848	0.9692	0.9848	0.9848	0.9848
0.2500	0.9966	0.9889	0.9733	0.9889	0.9889	0.9889
0.2000	0.9927	0.9849	0.9693	0.9849	0.9849	0.9849
0.1500	0.9928	0.9849	0.9692	0.9849	0.9849	0.9849
0.1000	0.9930	0.9851	0.9694	0.9851	0.9851	0.9851

fifth higher mode

T	z=40 km			dx=0.5 km		z=100
	dx=.25	dx=0.5	dx=1.0	z=40	z=70	
2.2960	.08099	.08054	.07972	0.1171	0.3077	0.4571
2.2900	0.2266	0.2253	0.2230	0.3185	0.6836	0.8523
2.2860	0.2996	0.2980	0.2949	0.4144	0.8015	0.9312
2.2000	0.8010	0.7963	0.7877	0.9187	0.9901	0.9902
2.1000	0.9213	0.9155	0.9050	0.9748	0.9880	0.9880
2.0000	0.9619	0.9555	0.9440	0.9839	0.9870	0.9870
1.9000	0.9784	0.9717	0.9596	0.9855	0.9863	0.9863
1.8000	0.9858	0.9788	0.9663	0.9857	0.9859	0.9859
1.7000	0.9892	0.9822	0.9694	0.9856	0.9856	0.9856
1.6000	0.9909	0.9837	0.9708	0.9854	0.9854	0.9854
1.5000	0.9917	0.9845	0.9714	0.9853	0.9853	0.9853
1.4000	0.9921	0.9848	0.9716	0.9852	0.9852	0.9852
1.3000	0.9923	0.9849	0.9717	0.9851	0.9851	0.9851
1.2000	0.9923	0.9850	0.9716	0.9850	0.9850	0.9850
1.1000	0.9923	0.9849	0.9716	0.9850	0.9850	0.9850
1.0000	0.9923	0.9849	0.9715	0.9849	0.9849	0.9849
0.9501	0.9923	0.9849	0.9715	0.9849	0.9849	0.9849
0.9001	0.9923	0.9849	0.9714	0.9849	0.9849	0.9849
0.8501	0.9923	0.9849	0.9714	0.9849	0.9849	0.9849
0.8001	0.9923	0.9849	0.9714	0.9849	0.9849	0.9849
0.7501	0.9923	0.9848	0.9714	0.9848	0.9848	0.9848
0.7001	0.9923	0.9848	0.9713	0.9848	0.9848	0.9848
0.6501	0.9923	0.9848	0.9713	0.9848	0.9848	0.9848
0.6000	0.9923	0.9848	0.9713	0.9848	0.9848	0.9848
0.5500	0.9923	0.9848	0.9713	0.9848	0.9848	0.9848
0.5000	0.9923	0.9848	0.9713	0.9848	0.9848	0.9848
0.4500	0.9923	0.9848	0.9713	0.9848	0.9848	0.9848
0.4000	0.9922	0.9847	0.9712	0.9847	0.9847	0.9847
0.3501	0.9922	0.9847	0.9712	0.9847	0.9847	0.9847
0.3000	0.9922	0.9847	0.9712	0.9847	0.9847	0.9847
0.2500	0.9927	0.9851	0.9715	0.9851	0.9851	0.9851
0.2000	0.9928	0.9852	0.9716	0.9852	0.9852	0.9852
0.1500	0.9921	0.9846	0.9710	0.9846	0.9846	0.9846
0.0000	0.9924	0.9849	0.9721	0.9849	0.9849	0.9849

longer periods the wavelength increases and the integration surface needs to be extended downward to maintain accurate results. When the depth to which the integration surface extends is less than n wavelengths then significant error occurs. This relation is clearly visible in the tables on pages 222 and 223. These tables show the mode by mode values of $2A_L I_1$ for each separate overtone, and for the fundamental. It is easily seen that the error is very small until $n+1$ wavelengths, for the n th higher mode, become longer than the depth extent of the RT integration surface. This explains why the RT integration results and the analytic synthetics needed to have the long periods removed to yield a good fit. Those long period components had large errors due to incomplete representation caused by the truncation of the integration surface at depth and thus contaminated otherwise accurate results.

Using the RT Integration Method for Long Oceanic Paths

Now that the reliability of the RT coupling of FE results to a receiver distant from the FE grid has been demonstrated it can be applied to the problem of investigating the propagation of L_g when the intermediate oceanic path is too long to be handled using FE alone. The amount of calculation needed to determine each seismogram using the coupling technique is large enough that the calculation of an entire depth section for reentry into another FE calculation would be worthwhile only if a specific example were to be considered, and detailed structure were known. Thus, the approach taken here is to calculate seismograms at the surface at receivers distant from the end of the FE grid, and to examine what the remaining modal energy looks like after propagation for a large distance through the oceanic crust. Then by knowing the proportion of surface amplitude that is removed by transmission through a reverse transition an estimate of the RMS amplitude of the L_g energy that travels through the transition can be made.

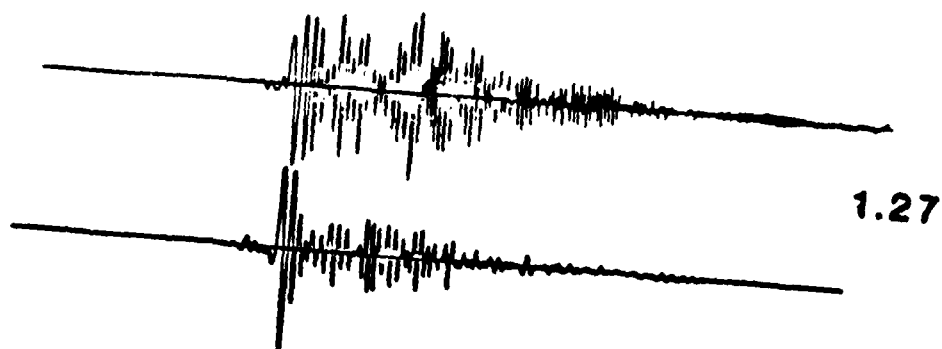
fundamental		1st		2nd	
T		T			
1000.	.00090	11.49	0.0000	5.750	0.0000
500.0	.00036	11.40	.00370	5.700	0.1350
250.0	.01457	11.20	0.1135	5.600	0.3522
90.00	0.1123	11.00	0.1868	5.500	0.5069
70.00	0.1843	10.80	0.2572	5.400	0.6219
60.00	0.2480	10.60	0.3249	5.300	0.7091
55.00	0.2920	10.40	0.3899	5.200	0.7758
50.00	0.3473	10.20	0.4521	5.100	0.8269
45.00	0.4169	10.00	0.5113	5.000	0.8660
40.00	0.5034	9.800	0.5672	4.900	0.8958
35.00	0.6070	9.600	0.6196	4.800	0.9184
30.00	0.7216	9.400	0.6681	4.700	0.9355
25.00	0.8314	9.200	0.7126	4.600	0.9485
20.00	0.9160	9.000	0.7530	4.500	0.9582
18.00	0.9397	8.800	0.7890	4.400	0.9654
16.00	0.9576	8.600	0.8210	4.300	0.9706
14.00	0.9701	8.400	0.8488	4.200	0.9748
12.00	0.9782	8.200	0.8729	4.100	0.9778
10.00	0.9827	8.000	0.8935	4.000	0.9800
8.000	0.9848	7.800	0.9108	3.800	0.9827
6.000	0.9854	7.600	0.9254	3.600	0.9842
4.000	0.9852	7.400	0.9374	3.400	0.9849
2.000	0.9848	7.200	0.9474	3.200	0.9852
1.800	0.9848	7.000	0.9555	3.000	0.9852
1.600	0.9847	6.500	0.9695	2.500	0.9851
1.400	0.9847	6.000	0.9775	2.000	0.9849
1.200	0.9846	5.500	0.9818	1.900	0.9849
1.000	0.9847	5.000	0.9839	1.800	0.9849
0.8000	0.9847	4.500	0.9848	1.700	0.9848
0.7000	0.9847	4.000	0.9851	1.600	0.9848
0.6000	0.9839	3.500	0.9852	1.500	0.9848
0.5000	0.9847	3.000	0.9851	1.400	0.9848
0.4000	0.9847	2.500	0.9850	1.300	0.9847
0.3000	0.9848	2.000	0.9848	1.200	0.9847
0.2500	0.9889	1.800	0.9848	1.100	0.9847
0.2000	0.9849	1.600	0.9847	1.000	0.9847
0.1500	0.9849	1.400	0.9847	0.9001	0.9846
0.1000	0.9851	1.200	0.9846	0.8001	0.9846
0.0000	0.0000	1.000	0.9846	0.7001	0.9846
0.0000	0.0000	0.9001	0.9846	0.6001	0.9844
0.0000	0.0000	0.8001	0.9845	0.5001	0.9843
0.0000	0.0000	0.7001	0.9849	0.4501	0.9844
0.0000	0.0000	0.6001	0.9843	0.4000	0.9845
0.0000	0.0000	0.5001	0.9844	0.3500	0.9845
0.0000	0.0000	0.4001	0.9841	0.3000	0.9845
0.0000	0.0000	0.3001	0.9841	0.2500	0.9849
0.0000	0.0000	0.2501	0.9844	0.2000	0.9850
0.0000	0.0000	0.2000	0.9849	0.1500	0.9851
0.0000	0.0000	0.1500	0.9851	0.100E	0.9865
0.0000	0.0000	0.1001	4.234	0.0000	0.0000

3rd		4th		5th	
T		T		T	
3.831	0.0000	2.873	0.0000	2.299	0.0000
3.824	.07248	2.869	.09512	2.296	0.1171
3.808	0.2093	2.860	0.2664	2.290	0.3185
3.800	0.2651	2.854	0.3519	2.286	0.4144
3.700	0.6640	2.800	0.7295	2.200	0.9187
3.600	0.8238	2.700	0.9145	2.100	0.9748
3.500	0.9005	2.600	0.9624	2.000	0.9839
3.400	0.9400	2.500	0.9777	1.900	0.9855
3.300	0.9609	2.400	0.9830	1.800	0.9857
3.200	0.9722	2.300	0.9848	1.700	0.9856
3.100	0.9784	2.200	0.9854	1.600	0.9854
3.000	0.9818	2.100	0.9855	1.500	0.9853
2.900	0.9836	2.000	0.9855	1.400	0.9852
2.800	0.9846	1.900	0.9854	1.300	0.9851
2.700	0.9851	1.800	0.9853	1.200	0.9850
2.600	0.9853	1.700	0.9852	1.100	0.9850
2.500	0.9854	1.600	0.9851	1.000	0.9849
2.400	0.9854	1.500	0.9850	0.9501	0.9849
2.300	0.9853	1.400	0.9850	0.9001	0.9849
2.200	0.9853	1.300	0.9849	0.8501	0.9849
2.000	0.9851	1.200	0.9849	0.8001	0.9849
1.800	0.9850	1.100	0.9848	0.7501	0.9848
1.600	0.9849	1.000	0.9848	0.7001	0.9848
1.500	0.9849	0.9501	0.9848	0.6501	0.9848
1.400	0.9848	0.9001	0.9848	0.6000	0.9848
1.300	0.9848	0.8501	0.9848	0.5500	0.9848
1.200	0.9848	0.8001	0.9848	0.5000	0.9848
1.100	0.9848	0.7501	0.9847	0.4500	0.9848
1.000	0.9847	0.7001	0.9847	0.4000	0.9847
0.9001	0.9847	0.6501	0.9847	0.3501	0.9847
0.8001	0.9847	0.6000	0.9847	0.3000	0.9847
0.7501	0.9846	0.5500	0.9847	0.2500	0.9851
0.7001	0.9847	0.5000	0.9847	0.2000	0.9852
0.6501	0.9846	0.4500	0.9847	0.1500	0.9846
0.6001	0.9846	0.4000	0.9847	0.1000	0.9849
0.5500	0.9846	0.3500	0.9846	0.0000	0.0000
0.5000	0.9846	0.3000	0.9846	0.0000	0.0000
0.4500	0.9846	0.2500	0.9851	0.0000	0.0000
0.4000	0.9849	0.2000	0.9846	0.0000	0.0000
0.3500	0.9846	0.1500	0.9847	0.0000	0.0000
0.3000	0.9845	0.1000	0.9849	0.0000	0.0000
0.2500	0.9844	0.0000	0.0000	0.0000	0.0000
0.2000	0.9837	0.0000	0.0000	0.0000	0.0000
0.1500	0.9853	0.0000	0.0000	0.0000	0.0000
0.1000	0.9856	0.0000	0.0000	0.0000	0.0000

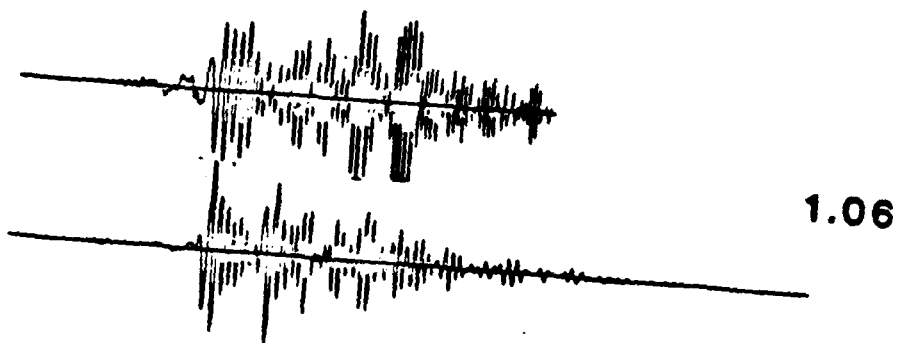
In order to perform the RT integration that propagates the FE results across the oceanic portion of the path sets of Green's functions must first be calculated for each distance at which the seismogram is to be examined. It should be noted that these Green's Functions are not identical to those used in the tests above. Since the propagation path has an oceanic crustal structure a different set of modes appropriate for an oceanic structure rather than a continental one must be used to determine the Green's functions. Since the oceanic crust is thinner than the continental crust the modes tend to concentrate at higher frequencies. Thus, more (eight) higher modes were used in the oceanic mode set than in the continental mode set. This does not give complete coverage in the period range considered, but should give an adequate Green's function.

To illustrate the effect that the oceanic propagation has on the FE results sampling a wavefield that has already propagated through a transition region three sample distances, from FE node to receiver, of one hundred, two hundred and fifty, and one thousand kilometers were chosen. Mode sum Green's functions for receivers at the crustal surface and sources where the FE displacements and stresses were recorded were calculated to be used in the RT integral. The seismograms resulting from the RT integrations are illustrated in Figure 19. In this figure the RT integration results for the two shortest paths are compared to FE results at the same locations with respect to the source. The result for the longer path is also shown below the upper two pairs of seismograms. In each of the pairs of illustrated seismograms the upper trace shows the FE result. This result includes propagation through an oceanic path length of 125 km, for the upper pair, or 275 km, for the lower pair. These seismograms are taken from the reverse reference model FE calculation which uses a column of nodes recorded in the fifty kilometer forward transition calculation as forcing functions. Displacements and stresses recorded at the same horizontal distance from the source as these forcing functions are used as the u_2 , and $\mu u_{2,1}$, terms in the RT

125 km



275 km



1025 km

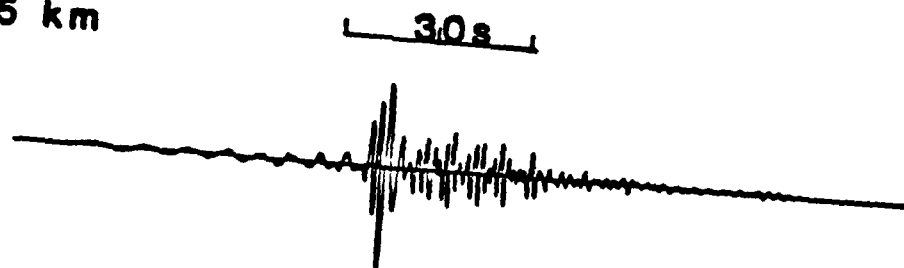


Figure 19: Seismograms for different oceanic path lengths. Each of the upper two pairs of traces compare FE and RT integration results at the indicated distances. The single seismogram at 1025 km shows RT integration results for a distance too long to treat using FE. The number to the right of each pair of seismograms gives the RMS amplitude ratio of the upper trace to the lower trace.

integration. The seismograms resulting from the RT integration of these terms with Green's functions for propagation through a path length of oceanic structure are shown as the lower seismograms. The upper pair of seismograms is for Green's functions for a one hundred kilometer path length, the lower pair for a Green's function path length of two hundred fifty kilometers. The numbers to the right of each pair indicate the RMS amplitude ratio of the upper seismogram to the lower one. The upper pair of seismograms shows reasonable agreement. At least half the difference between the two traces could easily be due to truncation errors caused by terminating the integration surface at 35 km depth. The remaining differences in amplitude and waveform can be explained as being due to a small component of non-modal energy which is filtered out of the result when using the RT integration but not when using the FE method. Thus, this pair of seismograms shows that after propagation through 125 km of oceanic path most of the non-modal energy is no longer visible at the surface. From the FE calculations whose time slices are shown in chapter two it is clear that at this distance some of the non-modal energy is still present at depth. This energy is probably a source of the amplitude discrepancy between the two uppermost seismograms. The lower pair of seismograms shows excellent agreement in amplitude but discrepancies in waveform for all but the initial arrivals. This is expected since the FE result is contaminated with small reflections from the nearby grid edge that can change the waveform significantly but have been shown to change the RMS amplitudes by at most a couple of percent. Thus the amplitude agreement at this distance implies that the non-modal energy remaining at depths included in the integration is not significant. However, the remaining amplitude of the Lg phase is still fifty five to seventy percent of the incident amplitude. Using longer transitions this can be reduced another five to ten percent, and adding the effects of intrinsic or scattering attenuation, which are not considered

in the calculations presented here, might produce a further small reduction in the the Lg wave amplitude. Thus, it is apparent that the attenuation due to passage through a transition region is not sufficient to explain the entire observed attenuation of Lg waves.

In conclusion, the FE results show several effects which are significant mechanisms for the attenuation of Lg as it passes through ocean continent or continent ocean transition regions. The most important of these effects, associated with the path length of oceanic structure, is the transmission of energy across the crust half-space boundary in the forward transition region and the conversion of that energy into downgoing non-modal phases. As the length of the oceanic path increases the amplitude of these downgoing phases increase and they are able to propagate far enough towards the base of the grid that they are not transmitted back into the crustal layer through the half-space crust boundary in the reverse transition region. The FE results illustrated in this chapter show that significant portions of the energy originally trapped in the continental crust can be carried out of the system in this manner. The RT integration results show that, for a 125 km path length, much of the downgoing energy has passed out of the depth region above the base of the continental crust, and that after propagation through an oceanic path of length 275 km the non-modal energy has become negligible. The attenuation of Lg passing through the reverse transition should be maximal for path lengths in excess of that length at which the non-modal energy has reached depths below the base of the continental crust. The oceanic path length necessary for complete escape of the non-modal component of the wavefield is on the order of 200 to 250 km but significant portions of the energy is able to escape for path lengths as short as eighty kilometers. The results presented here are for a fifty kilometer long transition. Since a longer transition region produces more rapid downward propagation these lengths should be expected to be an

overestimate of the observed Lg data which is on average associated with longer transitions. However, the amount of attenuation seen in the Lg phase is not large enough to explain the observed attenuation of Lg. These simple models show that geometry of the transition region alone produces at most a reduction of a factor of five or six in amplitude. Thus, the observed attenuation, which has frequently been attributed to the propagation effects caused by passage through a transition, cannot be entirely due to these propagation effects.

REFERENCES

- Abramowitz, M., Stegun, I., *Handbook of Mathematical Functions*, Dover, New York, 1972.
- Aki, K., Richards, P. G., *Quantitative Seismology*, W. H. Freeman & Co., San Francisco, 1980.
- Alsop, L. E., Transmission and Reflection of Love Waves at a Vertical Discontinuity, *J. Geophys. Res.*, vol. 71, pp. 3969-3984, 1966.
- Alsop, L. E., An Orthonormality Relation for Elastic Body Waves, *Bull. Seismol. Soc. Am.*, vol. 58, pp. 1949-1954, 1968.
- Baker, R. G., Determination of Magnitude from L_g , *Bull. Seismol. Soc. Am.*, vol. 60, pp. 1907-1919, 1970.
- Barker, B. W., Der, Z. A., Mrazek, C. P., The Effect of Crustal Structure on the Regional Phases P_g and L_g at the Nevada Test Site, *J. Geophys. Res.*, vol. 86, pp. 1686-1700, 1981.
- Barton, P., Matthews, D., Hall, J., Warner, M., Moho beneath the North Sea Compared on Normal Incidence and Wide-Angle Seismic Records, *Nature*, vol. 308, 1984.
- Basham, P. W., A New Magnitude Formula for Short Period Continental Rayleigh Waves, *Geophys. J. R. Astr. Soc.*, vol. 29, pp. 255-260, 1971.
- Bath, M., The Elastic Waves L_g and R_g along Euroasiatic Paths, *Arkiv for Geofysik*, vol. 2, pp. 295-342, 1954.
- Bath, M., Channel Waves, *J. Geophys. Res.*, vol. 63, pp. 583-587, 1958.
- Blandford, R., Seismic Event Discrimination, *Bull. Seismol. Soc. Am.*, vol. 72, pp. s69-s87, 1982.
- Bolt, B. A., Velocity of the Seismic Waves L_g and R_g across Australia, *Nature*, vol. 180, pp. 495, 1957.

- Bollinger, G. A., Attenuation of the L_g Phases and Determination of m_b in the Southeastern United States, *Bull. Seismol. Soc. Am.*, vol. 69, pp. 45-63, 1979.
- Boore, D., Love Waves in Nonuniform Wave Guides: Finite Difference Calculations, *J. Geophys. Res.*, vol. 75, pp. 1512-1527, 1970.
- Boore, D., A Note on the Effect of Simple Topography on Seismic SH Waves, *Bull. Seismol. Soc. Am.*, vol. 62, pp. 275-284, 1972a.
- Boore, D., Finite Difference Methods for Seismic-Wave Propagation in Heterogeneous Materials, Ch. 5 in *Methods in Computational Physics, Vol. II*, Academic Press, 1972b.
- Boore, D., Lerner, K. L., Aki, K., Comparison of Two Independent Methods for the Solution of Wave-Scattering Problems: Response of a Sedimentary Basin to Vertically Incident SH Waves, *J. Geophys. Res.*, vol. 76, pp. 558-569, 1971.
- Bose, S. K., Transmission of SH Waves across a Rectangular Step, *Bull. Seismol. Soc. Am.*, vol. 65, pp. 1779-1786, 1975.
- Bouchon, M., A Simple Method to Calculate Green's Functions for Elastic Layered Media, *Bull. Seismol. Soc. Am.*, vol. 71, pp. 959-971, 1981.
- Bouchon, M., The Complete Synthesis of Seismic Crustal Phases at Regional Distances, *J. Geophys. Res.*, vol. 87, pp. 1735-1741, 1982.
- Campillo, M., Bouchon, M., Massinon, B., Theoretical Study of the Excitation, Spectral Characteristics, and Geometrical Attenuation of Regional Seismic Phases, *Bull. Seismol. Soc. Am.*, vol. 74, pp. 79-90, 1984.
- Cara, M., Minster, J. B., Multi-Mode Analysis of Rayleigh-Type L_g . Part 1. Theory and Applicabilty of the Method., *Bull. Seismol. Soc. Am.*, vol. 71, pp. 973-984, 1981.
- Cara, M., Minster, J. B., LeBras, R., Multi-Mode Analysis of Rayleigh-Type L_g . Part 2. Application to Southern California and the Northwestern Sierra Nevada., *Bull. Seismol. Soc. Am.*, vol. 71, pp. 985-1002, 1981.

- Chinn, D. S., Isacks, B. L., Barazangi, M., High Frequency Seismic Wave Propagation in Western South America Along the Continental Margin, in the Nazca Plate, and across the Altiplano, *Geophys. J. R. Astr. Soc.*, vol. 60, pp. 209-244, 1980.
- Chung, D. H, Bernreuter, D. L., Regional Relationships among Earthquake Magnitude Scales, *Reviews of Geophys. Space Phys.*, vol. 19, pp. 649-663, 1981.
- Der, Z. A., Marshall, M. E., O'Donnell, A., McElfresh, T. W., Spatial Coherence Structure and Attenuation of the L_g Phase, Site Effects, and the Interpretation of the L_g Coda, *Bull. Seismol. Soc. Am.*, vol. 74, pp. 1125-1147, 1984.
- de Hoop, A., T., Representation Theorems for the Displacement in an Elastic Solid and Their Application to Elastodynamic Diffraction Theory, Sc. D. Thesis, Technische Hogeschool, Delft, 1958.
- Drake, L. A., Love and Rayleigh Waves in Nonhorizontally Layered Media, *Bull. Seismol. Soc. Am.*, vol. 62, pp. 1241-1258, 1972.
- Drake, L. A., Bolt, B. A., Love Waves Normally Incident at a Continental Boundary, *Bull. Seismol. Soc. Am.*, vol. 70, pp. 1103-1123, 1980.
- Dwyer, J. J., Herrmann, R. B., Nuttli, O. W., Spatial Attenuation of the L_g Wave in the Central United States, *Bull. Seismol. Soc. Am.*, vol. 73, pp. 781-796, 1983.
- Ebel, J. E., M_L Measurements for Northeastern United States Earthquakes, *Bull. Seismol. Soc. Am.*, vol. 72, pp. 1367-1378, 1982.
- Eittreim, S., Grantz, A., CDP Seismic Sections of the Western Beaufort Continental Margin, *Tectonophysics*, vol. 59, pp. 251-262, 1979.
- Frazier, G. A., Alexander, J. H., Petersen, C. M., 3-D Seismic code for the ILLIAC IV. *Systems, Science and Software Report SSS-R-73-1506*, 1973.
- Frazier, G. A., Petersen, C. M., 3-D Stress Wave Code for the ILLIAC IV. *Systems, Science and Software Report SSS-R-74-2109*, 1974.

- Gilbert, F., Knopoff, L., Seismic Scattering from Topographic Irregularities, *J. Geophys. Res.*, vol. 65, pp. 3437-3444, 1960.
- Grantz, A., Eittreim, S., Dinter, D. A., Geology and Tectonic Development of the Continental Margin North of Alaska, *Tectonophysics*, vol. 59, pp. 263-269, 1979.
- Gregersen, S., Possible Mode Conversion between Love and Rayleigh Waves at a Continental Margin, *Geophys. J. R. Astr. Soc.*, vol. 54, pp. 121-127, 1978.
- Gregersen, S., L_g Wave Propagation and Crustal Structure Differences near Denmark and the North Sea, *Geophys. J. R. Astr. Soc.*, vol. 79, pp. 217-234, 1984.
- Gregersen, S., Alsop, L. E., Amplitudes of Horizontally Refracted Love Waves, *Bull. Seismol. Soc. Am.*, vol. 64, pp. 535-553, 1974.
- Gregersen, S., Alsop, L. E., Mode Conversion of Love Waves at a Continental Margin, *Bull. Seismol. Soc. Am.*, vol. 66, pp. 1855-1872, 1976.
- Grow, J. A., Bowin, C. O., Hutchinson, D. R., The Gravity Field of the U. S. Atlantic Continental Margin, *Tectonophysics*, vol. 59, pp. 27-52, 1979.
- Gumper, F., Pomeroy, P. W., Seismic Wave Velocities and Earth Structure on the African Continent, *Bull. Seismol. Soc. Am.*, vol. 60, pp. 651-668, 1970.
- Gupta, I. N., Barker, B. W., Burnetti, J. A., Der, Z. A., A Study of the Regional Phases from Earthquakes and Explosions in Western Russia, *Bull. Seismol. Soc. Am.*, vol. 70, pp. 851-872, 1980.
- Gupta, I. N., von Seggern, D. H., Wagner, R. A., A Study of Variations in the Horizontal to Vertical L_g Amplitude Ratio in the Eastern United States, *Bull. Seismol. Soc. Am.*, vol. 72, pp. 2081-2088, 1982.
- Gutenberg, B., Channel Waves in the Earth's Crust, *Geophysics*, vol. 20 pp. 283-294, 1955.

- Harkrider, D. G., Surface Waves in Multilayered Media I, Rayleigh and Love Waves from Buried Sources in a Multilayered Elastic Half-Space, *Bull. Seismol. Soc. Am.*, vol. 54, pp. 627-679, 1964.
- Harkrider, D. G., Surface Waves in Multilayered Elastic Media, Part II. Higher Mode Spectra and Spectral Ratios from Point Sources in Plane Layered Earth Models, *Bull. Seismol. Soc. Am.*, vol. 60, pp. 1937-1987, 1970.
- Harkrider, D. G., Coupling Near Source Phenomena into Surface Wave Generation, pp. 277-326 in *Identification of Seismic Sources- Earthquake or Underground Explosion*, ed. Husebye, E. S., Mykkeltveit, S., eds, Reidel, 1981.
- Herrin, E., On \bar{P} and L_g , *J. Geophys. Res.*, vol. 66, pp. 334-335, 1961.
- Herrin, E., Minton, P. D., The Velocity of L_g in the Southwestern United States and Mexico, *Bull. Seismol. Soc. Am.*, vol. 50, pp. 35-44, 1960.
- Herrin, E., Richmond, J., On the Propagation of the L_g Phase, *Bull. Seismol. Soc. Am.*, vol. 50, pp. 197-210, 1960.
- Herrmann, R. B., Kijko, A., Modeling Some Empirical Vertical Component L_g Relations, *Bull. Seismol. Soc. Am.*, vol. 73, pp. 157-171, 1983a.
- Herrmann, R. B., Kijko, A., Short Period L_g Magnitudes: Instrument, Attenuation, and Source Effects, *Bull. Seismol. Soc. Am.*, vol. 73, pp. 1835-1850, 1983b.
- Herrmann, R. B., Nuttli, O. W., Ground Motion Modelling at Regional Distances for Earthquakes in a Continental Interior, I. Theory and Observations, *Int. J. Earthq. Engng. Struct. Dyn.*, vol. 4, pp. 49-58, 1975a.
- Herrmann, R. B., Nuttli, O. W., Ground Motion Modelling at Regional Distances for Earthquakes in a Continental Interior, II. Effect of Focal Depth, Azimuth, and Attenuation, *Int. J. Earthq. Engng. Struct. Dyn.*, vol. 4, pp. 59-77, 1975b.
- Herrmann, R. B., Nuttli, O. W., Magnitude: the Relation of M_L to m_{BL} , *Bull. Seismol. Soc. Am.*, vol. 72, pp. 389-397, 1982.

- Herrera, I., On a Method to Obtain a Green's Functions for a Multi-Layered Half Space, *Bull. Seismol. Soc. Am.*, vol. 54, pp. 1087-1096, 1964a.
- Herrera, I., A Perturbation Method for Elastic Wave Propagation: I. Nonparallel Boundaries, *J. Geophys. Res.*, vol. 69, pp. 3845-3851, 1964b.
- Hinz, K., Schluter, H.-U., Grant, A. C., Srivastava, S. P., Unpleby, D., Woodside, J., Geophysical Transects of the Labrador Sea: Labrador to Southwest Greenland, *Tectonophysics*, vol. 59, pp. 151-183, 1979.
- Hudson, J. A., The Passage of Elastic Waves through an Anomalous Region-IV. Transmission of Love Waves through a Laterally Varying Structure, *Geophys. J.*, vol. 49, pp. 645-654, 1977.
- Hudson, J. A., Scattered Surface Waves from a Surface Obstacle, *Geophys. J.*, vol. 13, pp. 441-458, 1967.
- Hudson, J. A., Knopoff, L., Transmission and Reflection of Surface Waves at a Corner: I. Love Waves, *J. Geophys. Res.*, vol. 69, pp. 275-280, 1964.
- Isacks, B. L., Stephens, C., Conversion of S_g to L_g at a Continental Margin, *Bull. Seismol. Soc. Am.*, vol. 65, pp. 235-244, 1975.
- Jones, F. B., Long, L. T., McKee, J. H., Study of the Attenuation and Azimuthal Dependence of Seismic Wave Propagation in the Southeastern United States. *Bull. Seismol. Soc. Am.*, vol. 67, pp. 1503-1513, 1977.
- Kadinsky-Cade, K., Barazangi, M., Oliver, J., Isacks, B., Lateral Variation of High Frequency Seismic Wave Propagation at Regional Distances across the Turkish and Iranian Plateaus, *J. Geophys. Res.*, vol. 86, pp. 9377-9396, 1981.
- Kazi, M. H., The Love Wave Scattering Matrix for a Continental Margin (Theoretical), *Geophys. J. R. Astr. Soc.*, vol. 52, pp. 25-44, 1978a.
- Kazi, M. H., The Love Wave Scattering Matrix for a Continental Margin (Numerical), *Geophys. J. R. Astr. Soc.*, vol. 53, pp. 227-243, 1978b.

- Keen, C. E., Hyndman, R. D., Geophysical Review of the Continental Margins of Eastern and Western Canada, *Can. J. Earth Sci.*, vol. 16, pp. 712-747, 1979.
- Kennett, B. L. N., The Interaction of Seismic Waves with Horizontal Velocity Contrasts, *Geophys. J. R. Astr. Soc.*, vol. 39, pp. 431-450, 1973.
- Kennett, B. L. N., Guided Wave Propagation in Laterally Varying Media-I. Theoretical Development, *Geophys. J. R. Astr. Soc.*, vol. 79, pp. 235-256, 1984.
- Kennett, B. L. N., Mykkeltveit, S., Guided Wave Propagation in Laterally Varying Media-II. L_g -Waves in North-Western Europe, *Geophys. J. R. Astr. Soc.*, vol. 79, pp. 257-267, 1984.
- Kennett, B. L. N., L_g Waves and Structural Boundaries, *Bull. Seismol. Soc. Am.*, vol. 76, pp. 1133-1142, 1986.
- Knopoff, L., Hudson, J. A., Transmission of Love Waves Past a Continental Margin, *J. Geophys. Res.*, vol. 69, pp. 1649-1653, 1964.
- Knopoff, L., Mal, A. K., Phase Velocities of Surface Waves in the Transition Zone of Continental Margins-I. Love Waves, *J. Geophys. Res.*, vol. 72, pp. 1769-1776, 1967.
- Knopoff, L., Mal, A. K., Alsop, L. E., Phinney, R. A., A Property of Long-Period Love Waves, *J. Geophys. Res.*, vol. 75, pp. 4084-4086, 1970.
- Knopoff, L., Schwab, F., Nakanishi, K., Chang, F., Evaluation of L_g as a Discriminant among Different Continental Crustal Structures, *Geophys. J. R. Astr. Soc.*, vol. 39, pp. 41-70, 1975.
- Knopoff, L., Schwab, F., Kausel, E., Interpretation of L_g , *Geophys. J. R. Astr. Soc.*, vol. 39, pp. 389-404, 1973.
- Kosloff, D., Frazier, G. A., Treatment of Hourglass Patterns in Lower Order Finite Element Codes, *International Journal for Numerical and Analytical Methods*.

vol. 2, pp. 57-72, 1978.

Kovach, R. L., Anderson, D. L., Higher Mode Surface Waves and Their Bearing on the Structure of the Earth's Mantle, *Bull. Seismol. Soc. Am.*, vol. 54, pp. 161-182, 1964.

Lapwood, E. R., Hudson, J. A., The Passage of Elastic Waves through an Anomalous Region-III. Transmission of Obliquely Incident Body Waves, *Geophys. J. R. Astr. Soc.*, vol. 40, pp. 255-268, 1975.

Lapwood, E. R., Hudson, J. A., Kembhavi, K., The Passage of Elastic Waves through an Anomalous Region-II. Transmission through a Layer between Two Different Media, *Geophys. J. R. Astr. Soc.*, vol. 40, pp. 241-254, 1975.

Lapwood, E. R., Hudson, J. A., Kembhavi, K., The Passage of Elastic Waves through an Anomalous Region-I. Transmission of Body Waves through a Soft Layer, *Geophys. J. R. Astr. Soc.*, vol. 31, pp. 457-467, 1973.

Le Douaran, S., Burrus, J., Avedik, F., Deep Structure of the North-Western Mediterranean Basin: Results of a Two-Ship Survey, *Marine Geology*, vol. 55, pp. 325-345, 1984.

Lehmann, I., On Short Period Surface Wave L_g and Crustal Structures, *Bull. D'information L'UGGI 2^e Aneé*, pp. 248-251, 1952.

Lehmann, I., On L_g as read in North American Records, *Annali di Geofisica*, vol. 10, pp. 1-28, 1957

Love, A. E. H., *A Treatise on the Mathematical Theory of Elasticity*, 4th edn. Cambridge University Press, Cambridge, 643 pp.

Lysmer, J., Drake, L. A., The Propagation of Love Waves across Nonhorizontally Layered Structures, *Bull. Seismol. Soc. Am.*, vol. 61, pp. 1233-1251, 1971.

Lysmer, J., Drake, L. A., A Finite Element Method for Seismology, Ch. 6 in *Methods in Computational Physics 11, Seismology*, Alder, B., Fernbach, S., Bolt, B. A., editors, Academic Press, 1972.

- Makris, J., Ben Abraham, Z., Behle, A., Ginzburg, A., Giese, P., Steinmetz, L., Whitmarsh, R. B., Eleftheriou, S., Seismic Refraction Profiles Between Cyprus and Israel and Their Interpretation, *Geophys. J. R. Astr. Soc.*, vol. 75, pp. 575-591, 1983.
- Makris, J., Stobbe, C., Physical Properties and State of the Crust and Upper Mantle of the Eastern Mediterranean Sea Deduced from Geophysical Data, *Marine Geology*, vol. 55, pp. 347-363, 1984.
- Mal, A. K., Herrera, I., Scattering of Love Waves by a Constriction in the Crust, *J. Geophys. Res.*, vol. 70, pp. 5125-5133, 1965.
- Martel, L., Love Wave Propagation Across a Step by Finite Elements and Spatial Filtering, *Geophys. J. R. Astr. Soc.*, vol. 61, pp. 639-677, 1980.
- Mantovani, E., Generation of Complete Theoretical Seismograms for SH-III, *Geophys. J. R. Astr. Soc.*, vol. 53, pp. 55-60, 1978.
- Mantovani, E., Schwab, F., Liao, H., Knopoff, L., Generation of Complete Theoretical Seismograms for SH-II, *Geophys. J. R. Astr. Soc.*, vol. 48, pp. 531-535, 1977.
- Nakanishi, K., Schwab, F., Knopoff, L., Generation of Complete Theoretical Seismograms for SH-I, *Geophys. J. R. Astr. Soc.*, vol. 48, pp. 525-530, 1977.
- Ni, J., Barazangi, M., High-Frequency Seismic Wave Propagation beneath the Indian Shield, Himalayan Arc, Tibetan Plateau, and Surrounding Regions: High Uppermost Mantle velocities and Efficient S_n Propagation Beneath Tibet, *Geophys. J. R. Astr. Soc.*, vol. 72, pp. 663-689, 1983.
- Nicolas, M., Massinon, B., Mechler, P., Bouchon, M., Attenuation of Regional Phases in Western Europe, *Bull. Seismol. Soc. Am.*, vol. 72, pp. 2089-2106, 1982.
- Nuttli, O. W., Seismic Wave Attenuation and Magnitude Relations for Eastern North America, *J. Geophys. Res.*, vol. 78, pp. 876-885, 1973.

- Nuttli, O. W., A Time Domain Study of the Attenuation of 10-Hz Waves in the New Madrid Seismic Zone, *Bull. Seismol. Soc. Am.*, vol. 68, pp. 343-355, 1978.
- Nuttli, O. W., The Excitation and Attenuation of Seismic Crustal Phases in Iran. *Bull. Seismol. Soc. Am.*, vol. 70, pp. 469-485, 1980.
- Nuttli, O. W., On the Attenuation of L_g Waves in Western and Central Asia and Their Use as a Discriminant between Earthquakes and Explosions, *Bull. Seismol. Soc. Am.*, vol. 71, pp. 249-261, 1981.
- Oliver, J., Dorman, J., Sutton, G., The Second Shear Mode of Continental Rayleigh Waves, *Bull. Seismol. Soc. Am.*, vol. 49, pp. 379-389, 1959.
- Oliver, J., Ewing, M., Press, F., Crustal Structure of the Arctic Regions from the L_g Phase, *Bull. Seismol. Soc. Am.*, vol. 66, pp. 1063-1074, 1955.
- Oliver, J., Ewing, M., Higher Modes of Continental Rayleigh Waves, *Bull. Seismol. Soc. Am.*, vol. 47, pp. 187-204, 1957.
- Oliver, J., Ewing, M., Normal Modes of Continental Surface Waves, *Bull. Seismol. Soc. Am.*, vol. 48, pp. 33-49, 1958a.
- Oliver, J., Ewing, M., The Effect of Surficial Sedimentary Layers on Continental Surface Waves, *Bull. Seismol. Soc. Am.*, vol. 48, pp. 339-354, 1958b.
- Panza, G. F., Calcagnile, G., Comparison of Multimode Surface Wave Response in Structures With and Without a Low Velocity Channel (Part I: Dip Slip Sources on a vertical Fault Plane), *Pure Appl. Geophys.*, vol. 112, pp. 583-596, 1974.
- Panza, G. F., Calcagnile, G., L_g , L_i and R_g from Rayleigh Modes, *Geophys. J. R. Astr. Soc.*, vol. 40, pp. 475-487, 1975.
- Panza, G. F., Schwab, F. A., Knopoff, L., Channel and Crustal Rayleigh Waves, *Geophys. J. R. Astr. Soc.*, vol. 30, pp. 273-280, 1972.

- Péč, K., Theoretical Dispersion Tables for Love Waves Propagating in a Wedge and in a Single Nonhomogeneous Layer with a Linear Velocity Gradient, *Pub. of Dominion Obs. Ottawa*, vol. 35, 1967.
- Pomeroy, P. W., Best, W. J., McKeivilly, T. V., Test Ban Treaty verification with Regional Data: A Review, *Bull. Seismol. Soc. Am.*, vol. 72, pp. s89-s129, 1982.
- Press, F., Velocity of L_g Waves in California, *Trans. A. G. U.*, vol. 37, pp. 615-618, 1956.
- Press, F., Ewing, M., Two Slow Surface Waves across North America, *Bull. Seismol. Soc. Am.*, vol. 42, pp. 219-228, 1952.
- Press, F., Ewing, M., Oliver, J., Crustal Structure and Surface-Wave Dispersion in Africa, *Bull. Seismol. Soc. Am.*, vol. 46, pp. 97-103, 1956.
- Press, F., Gutenberg, B., Channel P Waves Π_g in the Earth's Crust, *Trans. A. G. U.*, vol. 37, pp. 754-756, 1956.
- Ruzaikin, A. I., Nersesov, I. L., Khalturin, vol. I., Molnar, P., Propagation of L_g and Lateral Variations in Crustal Structure in Asia, *J. Geophys. Res.*, vol. 82, pp. 307-316, 1977.
- Sato, R., Love Waves Propagated across Transitional Zone, *Japan J. Geophys.*, vol. 2, pp. 117-134, 1961a.
- Sato, R., Love Waves in Case the Surface Layer is Variable in Thickness, *J. Phys. Earth.*, vol. 9, pp. 19-36, 1961b.
- Schlue, J. W., Love Wave Propagation in Three-Dimensional Structures Using Finite Element Techniques, *Bull. Seismol. Soc. Am.*, vol. 69, pp. 319-328, 1979.
- Savarensky, E., Valdner, N., Observations of L_g and R_g Waves from the Black Sea Basin Earthquakes, *Annali di Geofisica*, vol. 13, pp. 129-134, 1960.
- Schwab, F., Kausel, E., Knopoff, L., Interpretation of S_g for a Shield Structure, *Geophys. J. R. Astr. Soc.*, vol. 36, pp. 737-742, 1974.

- Sheridan, R. E., Grow, J. A., Behrent, J. C., Bayer K. C., Seismic Refraction Study of the Continental Edges of the Eastern United States, *Tectonophysics*, vol. 59, pp. 1-26, 1979.
- Shurbet, D. H., The High Frequency P and S Phases from the West Indies, *Bull. Seismol. Soc. Am.*, vol. 52, pp. 957-962, 1962.
- Shurbet, D. H., The High Frequency S Phase and Structure of the Upper Mantle, *J. Geophys. Res.*, vol. 69, pp. 2065-2070, 1964.
- Shurbet, D. H., Conversion of S_g at a Continental Margin, *Bull. Seismol. Soc. Am.*, vol. 66, 327-329, pp. 1976.
- Singh, S., Herrmann, R. B., Regionalization of Crustal Coda Q in the Continental United States, *J. Geophys. Res.*, vol. 88, pp. 527-538, 1983.
- Smith, W. D., A Nonreflecting Plane Boundary for Wave Propagation Problems, *J. Comp. Phys.*, vol. 15, pp. 492-503, 1974.
- Stephens, J. L., Day, S. M., The Physical Basis of m_b : M_s and Variable Frequency Magnitude Methods for Earthquake/Explosion Discrimination, *J. Geophys. Res.*, vol. 90, pp. 3009-3020, 1985.
- Stephens, C., Isacks, B. L., Toward an Understanding of S_g : Normal Modes of Love Waves in an Oceanic Structure, *Bull. Seismol. Soc. Am.*, vol. 67, pp. 69-78, 1977.
- Street, R., Scaling Northeastern United States/Southeastern Canadian Earthquakes by Their L_g Waves, *Bull. Seismol. Soc. Am.*, vol. 66, pp. 1525-1537, 1976.
- Street, R., Some Recent L_g Phase Displacement Spectral Densities and Their Implications with Respect to the Prediction of Ground Motions in Eastern North America, *Bull. Seismol. Soc. Am.*, vol. 74, pp. 757-762, 1984.
- Street, R., Herrmann, R. B., Nuttli, O. W., Spectral Characteristics of the L_g Wave Generated by Central United States Earthquakes *Geophys. J. R. Astr. Soc.*,

vol. 41, pp. 51-63, 1975.

Street, R., Turcotte, F. T., A Study of Northeastern North American Spectral Moments, Magnitudes, and Intensities, *Bull. Seismol. Soc. Am.*, vol. 67, pp. 599-614, 1977.

Sutton, G. H., Mitronovas, W., Pomeroy, P. W., Short-Period Seismic Energy Radiation Patterns from Underground Nuclear Explosions and Small Magnitude Earthquakes, *Bull. Seismol. Soc. Am.*, vol. 57, pp. 249-267, 1967.

Uchupi, Austin, J. A., The Geologic History of the Passive Margin off New England and the Canadian Maritime Provinces, *Tectonophysics*, vol. 59, pp. 53-69, 1979.

Utsu, T., Observations of the L_g Waves and Crustal Structure in the Vicinity of Japan,, vol. ..., pp. 499-508,

Wetmiller, R. J., Crustal Structure of Baffin Bay from Earthquake Generated L_g Phases, *Can. J. Earth Sci.*, vol. 11, pp. 123-130, 1974.

Zienkiewicz, O. C., *The Finite Element Method in Engineering Science*, McGraw-Hill, 1971.

Zienkiewicz, O. C., Cheung, ., *The Finite Element Method in Structural and Continuum Mechanics*, McGraw-Hill, 1967.

DARPA SUPPLEMENTAL LIST FOR TECHNICAL REPORTS (Unclassified)
DISTRIBUTION LIST

Dr. Monem Abdel-Gawad
Rockwell International Science Center
1049 Camino Dos Rios
Thousand Oaks, CA 91360

Professor Keiliti Aki
Center for Earth Sciences
University of Southern California
University Park
Los Angeles, CA 90089-0741

Professor Shelton S. Alexander
Geosciences Department
403 Deike Building
The Pennsylvania State University
University Park, PA 16802

Professor Charles B. Archambeau
Cooperative Institute for Research in
Environmental Sciences
University of Colorado
Boulder, CO 80309

Dr. Thomas C. Bache Jr.
Science Applications Int'l Corp.
10210 Campus Point Drive
San Diego, CA 92121

Dr. James Bulau
Rockwell International Science Center
1049 Camino Dos Rios
P.O. Box 1085
Thousand Oaks, CA 91360

Dr. Douglas R. Baumgardt
Signal Analysis and Systems Division
ENSCO, Inc.
5400 Port Royal Road
Springfield, VA 22151-2388

Dr. S. Bract
Science Applications Int'l Corp.
10210 Campus Point Drive
San Diego, CA 92121

Professor John Ebel
Department of Geology & Geophysics
Boston College
Chestnut Hill, MA 02167

Woodward-Clyde Consultants
Attn: Dr. Lawrence J. Burdick
Dr. Jeff Barker
P.O. Box 93245
Pasadena, CA 91109-3245 (2 copies)

Dr. Roy Burger
1221 Serry Rd.
Schenectady, NY 12309

Professor Robert W. Clayton
Seismological Laboratory
Division of Geological and Planetary
Sciences
California Institute of Technology
Pasadena, CA 91125

Dr. Vernon F. Cormier
Earth Resources Laboratory
Department of Earth, Atmospheric and
Planetary Sciences
Massachusetts Institute of Technology
42 Carleton Street
Cambridge, MA 02142

Professor Anton M. Dainty
AFGL/LWH
Solid Earth Geophysics Branch
Earth Sciences Division
Hanscom AFB, MA 01731

Dr. Zoltain A. Der
Teledyne Geotech
314 Monthery Street
Alexandria, VA 22314

Prof. Adam Dzierwonski
Hoffman Laboratory
Harvard University
20 Oxford St.
Cambridge, MA 02138

Professor John Ferguson
Center for Lithospheric Studies
The University of Texas at Dallas
P.O. Box 830688
Richardson, TX 75083-0688

Dr. Jeffrey W. Given
Sierra Geophysics
11255 Kirkland Way
Kirkland, WA 98033

Prof. Roy Greenfield
Geosciences Department
403 Deike Building
The Pennsylvania State University
University Park, PA 16802

Professor David G. Harkrider
Seismological Laboratory
Division of Geological and Planetary
Sciences
California Institute of Technology
Pasadena, CA 91125

Professor Donald V. Helmberger
Seismological Laboratory
Division of Geological and Planetary
Sciences
California Institute of Technology
Pasadena, CA 91125

Professor Eugene Herrin
Institute for the Study of Earth & Man
Geophysical Laboratory
Southern Methodist University
Dallas, TX 75275

Professor Robert B. Herrmann
Department of Earth and Atmospheric
Sciences
Saint Louis University
Saint Louis, MO 63156

Professor Lane R. Johnson
Seismographic Station
University of California
Berkeley, CA 94720

Professor Thomas H. Jordan
Department of Earth, Atmospheric and
Planetary Sciences
Massachusetts Institute of Technology
Cambridge, MA 02139

Dr. Alan Kafka
Department of Geology & Geophysics
Boston College
Chestnut Hill, MA 02167

Professor Charles A. Langston
Geosciences Department
403 Deike Building
The Pennsylvania State University
University Park, PA 16802

Professor Thorne Lay
Department of Geological Sciences
1006 C.C. Little Building
University of Michigan
Ann Arbor, MI 48109-1063

Dr. George R. Mellman
Sierra Geophysics
11255 Kirkland Way
Kirkland, WA 98033

Professor Brian J. Mitchell
Department of Earth and Atmospheric
Sciences
Saint Louis University
Saint Louis, MO 63156

Professor Thomas V. McEvilly
Seismographic Station
University of California
Berkeley, CA 94720

Dr. Keith L. McLaughlin
Teledyne Geotech
314 Montgomery Street
Alexandria, VA 22314

Professor Otto W. Nuttli
Department of Earth and Atmospheric
Sciences
Saint Louis University
Saint Louis, MO 63156

Professor Paul G. Richards
Lamont-Doherty Geological Observatory
of Columbia University
Palisades, NY 10964

Dr. Norton Rimer
S-Cubed
A Division of Maxwell Laboratory
P.O. 1620
La Jolla, CA 92038-1620

Professor Larry J. Ruff
Department of Geological Sciences
1006 C.C. Little Building
University of Michigan
Ann Arbor, MI 48109-1063

Professor Charles G. Sammis
Center for Earth Sciences
University of Southern California
University Park
Los Angeles, CA 90089-0741

Dr. David G. Simpson
Lamont-Doherty Geological Observatory
of Columbia University
Palisades, NY 10964

Dr. Jeffrey L. Stevens
S-CUBED,
A Division of Maxwell Laboratory
P.O. Box 1620
La Jolla, CA 92038-1620

Professor Brian Stump
Institute for the Study of Earth
and Man
Geophysical Laboratory
Southern Methodist University
Dallas, TX 75275

Professor Ta-liang Teng
Center for Earth Sciences
University of Southern California
University Park
Los Angeles, CA 90089-0741

Dr. R. B. Tittmann
Rockwell International Science Center
1049 Camino Dos Rios
P.O. Box 1085
Thousand Oaks, CA 91360

Professor M. Nafi Toksoz
Earth Resources Laboratory
Department of Earth, Atmospheric and
Planetary Sciences
Massachusetts Institute of Technology
42 Carleton Street
Cambridge, MA 02142

Professor Terry C. Wallace
Department of Geosciences
Building #11
University of Arizona
Tucson, AZ 85721

Prof. John H. Woodhouse
Hoffman Laboratory
Harvard University
20 Oxford St.
Cambridge, MA 02138

Dr. G. Blake
US Dept of Energy/DP 331
Forrestal Building
1000 Independence Ave.
Washington, D.C. 20585

Dr. Michel Bouchon
Universite Scientifique et
Medicale de Grenoble
Laboratoire de Geophysique
Interne et Tectonophysique
I.R.I.G.M.-B.P. 68
38402 St. Martin D'Herès
Cedex FRANCE

Dr. Hilmar Bungum
NTNF/NORSAR
P.O. Box 51
Norwegian Council of Science,
Industry and Research, NORSAR
N-2007 Kjeller, NORWAY

Dr. Alan Douglas
Ministry of Defense
Blacknest, Brimpton, Reading RG7-4RS
UNITED KINGDOM

Professor Peter Harjes
Institute for Geophysics
Rhur University
Bochum
P.O. Box 102148
4630 Bochum 1
FEDERAL REPUBLIC OF GERMANY

Dr. James Hannon
Lawrence Livermore National Laboratory
P.O. Box 808
Livermore, CA 94550

Dr. E. Husebye
NTNF/NORSAR
P.O. Box 51
N-2007 Kjeller, NORWAY

Dr. Arthur Lerner-Lam
Lamont-Doherty Geological Observatory
of Columbia University
Palisades, NY 10964

Mr. Peter Marshall
Procurement Executive
Ministry of Defense
Blacknest, Brimpton, Reading RG7-4RS
UNITED KINGDOM

Dr. B. Massinon
Societe Radiomana
27, Rue Claude Bernard
75005, Paris, FRANCE

Dr. Pierre Mechler
Societe Radiomana
27, Rue Claude Bernard
75005, Paris, FRANCE

Mr. Jack Murphy
S-CUBED
Reston Geophysics Office
11800 Sunrise Valley Drive
Suite 1212
Reston, VA 22091

Dr. Svein Mykkeltveit
NTNF/NORSAR
P.O. Box 51
N-2007 Kjeller, NORWAY

Dr. Carl Newton
Los Alamos National Laboratory
P.O. Box 1663
Mail Stop C 335, Group ESS3
Los Alamos, NM 87545

Dr. Peter Basham
Earth Physics Branch
Department of Energy and Mines
1 Observatory Crescent
Ottawa, Ontario
CANADA K1A 0Y3

Professor J. A. Orcutt
Geological Sciences Division
Univ. of California at San Diego
La Jolla, CA 92093

Dr. Frank F. Pilotte
Director of Geophysics
Headquarters Air Force Technical
Applications Center
Patrick AFB, Florida 32925-6001

Professor Keith Priestley
University of Nevada
Mackay School of Mines
Reno, Nevada 89557

Mr. Jack Raclin
USGS - Geology, Rm 3C136
Mail Stop 928 National Center
Reston, VA 22092

Dr. Frode Ringdal
NTNF/NORSAR
P.O. Box 51
N-2007 Kjeller, NORWAY

Dr. George H. Rothe
Chief, Research Division
Geophysics Directorate
Headquarters Air Force Technical
Applications Center
Patrick AFB, Florida 32925-6001

Dr. Alan S. Ryall, Jr.
Center for Seismic Studies
1300 North 17th Street
Suite 1450
Arlington, VA 22209-2308

Dr. Lawrence Turnbull
OSWR/NED
Central Intelligence Agency
CIA, Room 5G48
Washington, DC 20505

Professor Steven Grand
Department of Geology
245 Natural History Bldg
1301 West Green Street
Urbana, IL 61801

Dr. Gary McCartor
Mission Research Corp.
735 State Street
P.O. Box Drawer 719
Santa Barbara, CA 93102

DARPA/PM
1400 Wilson Boulevard
Arlington, VA 22209

Defense Technical Information Center
Cameron Station
Alexandria, VA 22314 (12 copies)

Defense Intelligence Agency
Directorate for Scientific and
Technical Intelligence
Washington, D.C. 20301

Defense Nuclear Agency
Shock Physics Directorate/SS
Washington, D.C. 20305

Defense Nuclear Agency/SPSS
ATTN: Dr. Michael Shore
6801 Telegraph Road
Alexandria, VA 22310

AFOSR/NPG
ATTN: Director
Bldg 410, Room C222
Bolling AFB, Washington, D.C. 20332

AFTAC/CA (STINFO)
Patrick AFB, FL 32925-6001

AFWL/NTESC
Kirtland AFB, NM 87171

U.S. Arms Control & Disarmament Agency
ATTN: Mrs. M. Hoinkes
Div. of Multilateral Affairs, Rm 5499
Washington, D.C. 20451

U.S. Geological Survey
ATTN: Dr. T. Hanks
National Earthquake Research Center
345 Middlefield Road
Menlo Park, CA 94025

SRI International
333 Ravensworth Avenue
Menlo Park, CA 94025

Center for Seismic Studies
ATTN: Dr. C. Romney
1300 North 17th Street
Suite 1450
Arlington, VA 22209 (3 copies)

Dr. Robert Blandford
DARPA/GSD
1400 Wilson Boulevard
Arlington, VA 22209-2308

Ms. Ann Kerr
DARPA/GSD
1400 Wilson Boulevard
Arlington, VA 22209-2308

Dr. Ralph Alewine III
DARPA/GSD
1400 Wilson Boulevard
Arlington, VA 22209-2308

Mr. Edward Giller
Pacific Sierra Research Corp.
1401 Wilson Boulevard
Arlington, VA 22209

Science Horizons, Inc.
Attn: Dr. Bernard Minster
Dr. Theodore Cherry
710 Encinitas Blvd., Suite 101
Encinitas, CA 92024 (2 copies)

Dr. Jack Evernden
USGS - Earthquake Studies
345 Middlefield Road
Menlo Park, CA 94025

Dr. Lawrence Braile
Department of Geosciences
Purdue University
West Lafayette, IN 47907

Dr. G.A. Bollinger
Department of Geological Sciences
Virginia Polytechnical Institute
21044 Derring Hall
Blacksburg, VA 24061

Dr. L. Sykes
Lamont Doherty Geological Observatory
Columbia University
Palisades, NY 10964

Dr. S.W. Smith
Geophysics Program
University of Washington
Seattle, WA 98195

Dr. L. Timothy Long
School of Geophysical Sciences
Georgia Institute of Technology
Atlanta, GA 30332

Dr. N. Biswas
Geophysical Institute
University of Alaska
Fairbanks, AK 99701

Dr. Freeman Gilbert
Institute of Geophysics &
Planetary Physics
Univ. of California at San Diego
P.O. Box 109
La Jolla, CA 92037

Dr. Pradeep Talwani
Department of Geological Sciences
University of South Carolina
Columbia, SC 29208

University of Hawaii
Institute of Geophysics
Attn: Dr. Daniel Walker
Honolulu, HI 96822

Dr. Donald Forsyth
Department of Geological Sciences
Brown University
Providence, RI 02912

Dr. Jack Oliver
Department of Geology
Cornell University
Ithaca, NY 14850

Dr. Muawia Barazangi
Geological Sciences
Cornell University
Ithaca, NY 14853

Rondout Associates
Attn: Dr. George Sutton
Dr. Jerry Carter
Dr. Paul Pomeroy
P.O. Box 224
Stone Ridge, NY 12484 (3 copies)

Dr. Bob Smith
Department of Geophysics
University of Utah
1400 East 2nd South
Salt Lake City, UT 84112

Dr. Anthony Gangi
Texas A&M University
Department of Geophysics
College Station, TX 77843

Dr. Gregory B. Young
ENSCO, Inc.
5400 Port Royal Road
Springfield, CA 22151

Dr. Ben Menaheim
Weizman Institute of Science
Rehovot, ISRAEL 951729

Weidlinger Associates
Attn: Dr. Gregory Wojcik
620 Hansen Way, Suite 100
Palo Alto, CA 94304

Dr. Leon Knopoff
University of California
Institute of Geophysics & Planetary
Physics
Los Angeles, CA 90024

Dr. Kenneth H. Olsen
Los Alamos Scientific Laboratory
Post Office Box 1663
Los Alamos, NM 87545

Prof. Jon F. Claerbout
Prof. Amos Nur
Dept. of Geophysics
Stanford University
Stanford, CA 94305 (2 copies)

Dr. Robert Burridge
Schlumberger-Doll Research Ctr.
Old Quarry Road
Ridgefield, CT 06877

Dr. Eduard Berg
Institute of Geophysics
University of Hawaii
Honolulu, HI 96822

Dr. Robert Phinney
Dr. F.A. Dahlen
Dept. of Geological & Geophysical Sci.
Princeton University
Princeton, NJ 08540 (2 copies)

Dr. Kin-Yip Chun
Geophysics Division
Physics Department
University of Toronto
Ontario, CANADA M5S 1A7

New England Research, Inc.
Attn: Dr. Randolph Martin III
P.O. Box 857
Norwich, VT 05055

Sandia National Laboratory
Attn: Dr. H.B. Durham
Albuquerque, NM 87185

Dr. Gary McCartor
Mission Research Corp.
735 State Street
P. O. Drawer 719
Santa Barbara, CA 93102

Dr. W. H. K. Lee
USGS
Office of Earthquakes, Volcanoes,
& Engineering
Branch of Seismology
345 Middlefield Rd
Menlo Park, CA 94025

AFGL/XO
Hanscom AFB, MA 01731-5000

AFGL/LW
Hanscom AFB, MA 01731-5000

AFGL/SULL
Research Library
Hanscom AFB, MA 01731-5000 (2 copies)

Secretary of the Air Force (SAFRD)
Washington, DC 20330

Office of the Secretary Defense
DDR & E
Washington, DC 20330

HQ DNA
Attn: Technical Library
Washington, DC 20305

Director, Technical Information
DARPA
1400 Wilson Blvd.
Arlington, VA 22209

Los Alamos Scientific Laboratory
Attn: Report Library
Post Office Box 1663
Los Alamos, NM 87544

Dr. Thomas Weaver
Los Alamos Scientific Laboratory
Los Alamos, NM 87544

Dr. Al Florence
SRI International
333 Ravenswood Avenue
Menlo Park, CA 94025-3493

END

DATE

FILMED

7-88

Dtic